Characterisation of a Novel Radiation Detector and Demonstration of a Novel Error Detection Algorithm for Application in Radiotherapy

Hanan Mohammed Saeed Alzahrani

A dissertation submitted in partial fulfillment

of the requirements for the degree of

Doctor of Philosophy

of

University College London.

Division of Surgery and Interventional Science

University College London

March 1, 2022

I, Hanan Mohammed Saeed Alzahrani, confirm that the work presented in this thesis is my own. Where information has been derived from other sources, I confirm that this has been indicated in the work.

Abstract

Radiation detectors play an important role in radiology departments, particularly in relation to imaging and dosimetry. The significant advances achieved in material properties and high-quality electronic systems during previous decades has led to a continual expansion of their role and usage. In turn, this has had a concomitant impact upon the rapid progress of radiation detector technologies, specifically those utilised in medical imaging and dosimetry. This thesis aims to evaluate a radiation detector for a particular function, and to assess its suitability for said function within radiology and radiotherapy departments.

Two novel radiation detectors, one for low energy imaging (kV) and another for radiotherapy (MV), are named Lassena (kV) and Lassena (MV) respectively. These detectors underwent an evaluation for the first time in order to assess their performance. Lassena (kV) was assessed in terms of image resolution and noise level to obtain the detective quantum efficiency (DQE) values representing image quality. DQE (0.5) values were 0.46-0.59 for three beam energies. Lassena (MV) was evaluated regarding its dosimetric properties, including linearity based on dose rate, reproducibility, and uniformity. Lassena (MV) has a high degree of short-term reproducibility, an acceptable pixel uniformity-response at high dose rates, and acceptable linearity with a coefficient of determination (R^2) of 0.8624. Lassena (kV) displayed promising results whilst Lassena (MV) exhibited high sensitivity to radiation.

A Monte Carlo system consisting of a linear accelerator and radiation detector

was built and calibrated in order to assess dose verification applications within radiotherapy using a radiation detector. Anatomical changes during radiation therapy (such as parotid shrinkage and sinusitis for a nasopharyngeal case) were replicated. Analysis of computational EPID images started to warn of a risk of deviation from the planned dose at -26.3% volume loss of the parotid gland. This is most likely to happen in the third week of the treatment, however, the user must be aware of the limitations present due to anatomical overlapping and gamma analysis.

Impact Statement

In X-ray detectors, radiation energy is converted into forms which can be identified either visually or electronically. There are two main usages for these detectors: imaging and dosimetry. This thesis aims to evaluate a radiation detector for a particular function, and to assess its suitability for said function within radiology and radiotherapy departments.

In this work, two novel radiation detectors have been examined and tested in terms of their suitability for imaging via X-rays in kilovolt (kV) and megavolt (MV) ranges. The detectors are named Lassena (kV) and Lassena (MV) based on the used X-ray range. Lassena (kV) presented promising results for cone-beam computed tomography (CBCT) applications. This is especially exciting since the market thereof is in need of a new detector for CBCT and which uses a low radiation dose whilst nonetheless maintaining good image quality. The development of new scintillators to take advantage of low noise sensors, such as Lassena (kV), could drastically improve the performance of imaging systems based on this type of sensor. The Lassena (MV) design was also evaluated, and the results have been sent to the designers in order to improve the design since it was discovered that the detector saturates very quickly. Lassena (MV) detector can be used (after modifications) in radiotherapy departments for dosimetry and imaging purposes.

Electronic portal imaging devices (EPID) are the currently available dosimeters for taking X-rays in the MV range: they are commonly utilised for patient setup and positioning. In terms of computational work, a virtual EPID built by EGSnrc software, is used to assess its detection abilities for the anatomical changes

of parotid glands due to radiation exposure in a head and neck cancer case. The results of the computational study demonstrated the utility of EPID for monitoring anatomical changes of the parotid gland during radiation treatment. This can improve patients' life quality, especially in departments where there is limited access to modern technology.

The anatomical superimposition and gamma analysis influence the EPID ability to detect the changes: this leads to a limit on the EPID usage of dose verification. The work here presented the impact of these factors and provided some recommendations and suggestions to take into account whilst using EPID for dose verification.

Acknowledgements

Who does not thank people, is not thankful to God. In this vein, I begin as usual by thanking my first and second supervisors Kate Ricketts and Gary Royle for their guidance.

I also wish to express my sincere thanks to the first paper co-authors: Sion Richards, Iain Sedgwick, and Anastasios Konstantinidis for giving me the necessary guidance in how to write a scientific paper.

Thanks to colleagues and the department staff who were nice to me at work, and for their constant help and encouragement, specifically Dr. Paul Burke, Dr. Jamie McClelland and Mr. Adam Szmul.

Special Thanks to the French students I worked with. They displayed high work performance and ethics. Thanks to Alexandre Piccoli and Emeric Moulene who started using EGSnrc and collecting the Linac parameter from an online source. Thanks to Apolline Assaud for collecting data about the parotid shrinkage for nasopharyngeal carcinoma cases during radiotherapy. Final thanks to Magali Gidenne for helping me run the simulations.

Thanks to Royal Free Hospital and University College London Hospital (UCLH) for providing the necessary data for this work.

Thanks to the people in the EGSnrc workshop whose company I enjoyed during the workshop in addition to their support, help and encouragement, particularly Dr. Reid Townson.

I would like to thank the Kingdom of Saudi Arabia and the United Kingdom governments; I am very grateful for both. I hope they remain safe and flourishing. Thanks to Taibah University, my scholarship sponsor, and my workplace.

Last but not least, thank you to all my family members for their beautiful and honest wishes and prayers.

Contents

List of Figures

List of Tables

Dedicated to Hanan and her family

Acronyms

K_a Air-Kerma. 67

Al aluminium. 40

APS active pixel sensors. 31

ART adaptive radiotherapy. 54

CBCT cone beam computed tomography. 54

CCD charge-coupled device. 38

CMOS complementary metal-oxide semiconductor. 31

CsI(Tl) Cesium Iodide activated with Thallium. 38, 82

CTV clinical target volume. 121

d' sensitivity index. 128

DD dose difference. 49

DICOM Digital Imaging and COmmunications in Medicine. 44

DQE detective quantum efficiency. 33

DTA distance to agreement. 49

ECUT global electron cutoff energy. 46

EGS Electron gamma shower. 43

EPID electronic portal imaging device. 30

FPN fixed pattern noise. 36

Gadox gadolinium oxysulfide. 114

GPRs gamma passing rates. 129

HVL half value layer. 66

IAEA International Atomic Energy Agency. 94

IEC International Electrotechnical Commission. 29

kV kilovolt. 55

linac Linear accelerator. 39

lp/mm line pairs per millimetre. 30

MC Monte Carlo. 9, 39–48

MLCs multi-leaf collimators. 40

MPV mean pixel value. 68

MU monitor units. 40

MV megavolts. 30

NNPS Normalised noise power spectrum. 9, 35

OARs organs at risk. 131

PCUT global photon cutoff energy. 46

PDD percentage depth dose. 41

pMTF Pre-sampling modulation transfer function. 9, 34

PPS passive pixel sensor. 31

PSF phase space file. 44

PTV planning target volume. 121

SNR signal to noise ratio. 70, 81

STP Signal transfer property. 68

TPS treatment planning system. 56

VMAT volumetric arc therapy. 58

VRTs variance reduction techniques. 46

W tungsten. 40

Outputs

Journal publications

- **Alzahrani, H.**, Richards, S., Sedgwick, I., Seller, P., Konstantinidis, A., Royle, G., Ricketts, K. (2020). Image quality determination of a novel digital detector for X-ray imaging and cone-beam computed tomography applications. Nuclear Instruments and Methods in Physics Research Section A: Accelerators, Spectrometers, Detectors and Associated Equipment, 968, 163914.

Conference publications

- **Alzahrani, H.**, Richards, S., Sedgwick, I., Seller, P., Konstantinidis, A., Royle, G., Ricketts, K. (2018, November). Image Quality Determination of a Novel Low Energy X-ray Detector. In 2018 IEEE Nuclear Science Symposium and Medical Imaging Conference Proceedings (NSS/MIC) (pp. 1-2). IEEE. Poster presented.

- **Alzahrani, H.**, Royle, G., Ricketts, K. (2019). Monte Carlo Modelling and Calibration of Radiotherapy X-ray Beams. In 2019 UCL Computational Sciences symposium. Poster presented.

- **Alzahrani, H.**, Gidenne, M., Collins-Fekete, C. A., Royle, G., Ricketts, K. (2020). In Silico Study of Investigating the Sensitivity of Three EPID Models to Anatomical Changes. International Journal of Radiation Oncology,

Biology, Physics, 108(3), e263-e264. Poster abstract publication.

Chapter 1

Introduction

1.1 The clinical importance of the work

Clinical problems and unmet needs in the current situation:

1.1.1 Medical imaging and CBCT application

Radiation imaging devices are subject to continuous adaptation given that they are those most frequently used for patient examination [1]. Trends such as the rise of new diseases, the prevalence of some diseases, and the need for efficient and outcome-oriented systems have led to emerging new designs for imaging systems as well as their components in order to meet ongoing clinical needs. However, new designs must undergo rigorous evaluation and testing to determine their performance and outcome image quality before clinical use [2]. Image resolution and noise level play an important role in determining overall image quality. These elements are measured using modulation transfer function (MTF) and noise power spectrum (NPS) metrics, respectively. Each should reach a certain level in order to obtain a meaningful image in accordance with International Electrotechnical Commission (IEC) standards [3]. In general, radiography detectors can produce good quality images [4–6]. However, for cone-beam computed tomography systems, the market is in need of better options in order to provide superior image quality [7–11].

1.1.2 Imaging and dosimetry in radiotherapy departments

Currently, the electronic portal imaging device (EPID) is the most exceptional system for imaging and dosimetry in radiotherapy departments [12]. However, it renders low image quality due to high noise generated via Compton scattering. This is dominant tissue interaction in radiotherapy whereby a high energy (i.e., megavolts (MV) range) is used [13]. Moreover, clinical EPID images have around 0.7 line pairs per millimetre (lp/mm) at modulation transfer function (MTF) 10%, whereas a good imaging system should score 3 and 5 lp/mm at MTF 10% [4, 14, 15]. This implies that EPID has poor resolution resulting from large pixel pitches which are usually from 0.3 to 0.4 mm [16]. To that end, the new design may provide superior image quality due to the fine pixel size (50 μm (0.05 mm)) which is responsible for improving the image resolution, and the thick scintillator which will allow a better signal to noise ratio (i.e., generate more useful information).

1.1.3 EPID application for error detection raised from anatomical changes due to radiation exposure for head and neck cancer patients

EPID has a key function enabling it to achieve a successful radiotherapy treatment. It does this by determining the delivered dose and radiation field placement accuracy. EPID is attached to almost all commercially available radiotherapy machines by supporting arms [14, 17]. Furthermore, it has the ability to monitor anatomical changes. Imaging feedback will be utilised for adaptive radiotherapy in order to deliver radiation dosages accurately according to the description dose, despite the presence of ongoing, dynamic changes. As such, it is able to continually modify and correct the treatment plan accordingly [18]. EPID monitors the changes in the patient by comparing the image acquired on the first day (i.e., its reference image) with the images acquired on other days (i.e., evaluation images) by utilising gamma analysis [19, 20]. Nevertheless, EPID is not routinely used in many clinics during treatment [21]. Rather, it is mostly utilised for pre-treatment and patient positioning

verifications [22–24].

1.2 Complementary metal-oxide semiconductor

Radiation detection systems play an important role in radiology. As with the discovery of ionising radiation, the need for an adequate radiation detector was born: this encouraged scientists to seek methods to observe and measure radiation. The main categories of detectors involved in this project are: imaging devices (such as the detectors used in radiography departments) or, dose measurement devices (such as the detectors in radiotherapy) which are used for dosimetry [2].

In recent years, with the rapid development of technology, digital sensors have become the dominant system in medical imaging worldwide. There have many noticeable advantages: low costs; lightweight equipment; good image quality; easy accessibility; and, the possibility of digital storage in computers with vast memory capacities. The digital sensors also guarantee quick image processing and acquisition: hence, they quickly replaced the traditional film-based methods given their rapid and highly efficient nature [25].

These unique features of digital detectors are due complementary metal-oxide semiconductor (CMOS). CMOS is a technology used to construct integrated circuits using p- and n-type metal-oxide semiconductors. The transistors are separated from each other by a well that has reverse doping to the original material [26, 27]. In general, CMOS technology can be found in many commercial products such as mobile phones, laptops, webcams, digital cameras, and radiation detectors [28–30]. This technology comes in two different architectures: namely, passive pixel sensor (PPS), the first design used in CMOS radiation detectors; and, active pixel sensors (APS), which came later [31, 32].

- **Passive pixel sensor (PPS)**

  Passive pixel sensors are the first generation of CMOS-based sensors. Each pixel in PPS consists of a photodiode sensitive to optical light in order to col-

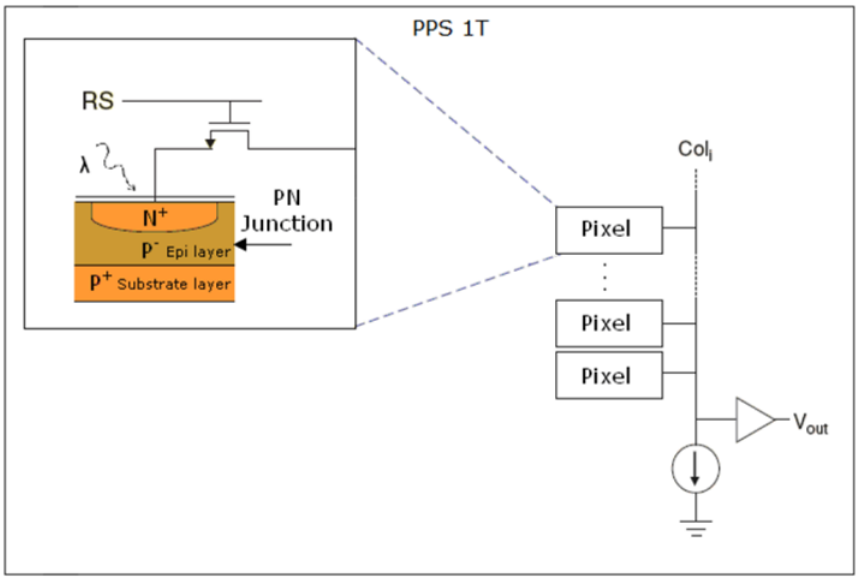

Figure 1.1: A schematic showing the PPS one transistor (1T) pixel and readout architecture [34].

lect and convert this to equivalent charges in a given time period, referred to as the 'integration time'. This is in addition to one simple amplifier transistor (1T) (the row select transistor (RS)) for signal input, and which is connected to a readout structure. Afterwards, the pixel is reset via the reference voltage (V_{REF}) (see Figure 1.1). Despite the high fill factor and small pixel size, PPS has limited performance due to relatively slow readout speeds and high noise [25, 32, 33].

- **Active pixel sensor (APS)**

  As mentioned before, the APS came after the PPS in order to overcome the limitations of PPS. It promised to improve the readout speed and reduce noise since each pixel works individually [32]. APS delivers high performance thanks to its structure: each pixel has a photodiode and three transistors (3T) which are the reset transistor (R), the source follower (SF), and the row select transistor (RS) (see Figure 1.2) [26]. The reset transistor removes the integrated charge from the pixel, and the source follower amplifies and reads the charge. Subsequently, the pixel is activated by the row select transistor for readout and then its voltage is presented to the column bus (Col_i). This is the

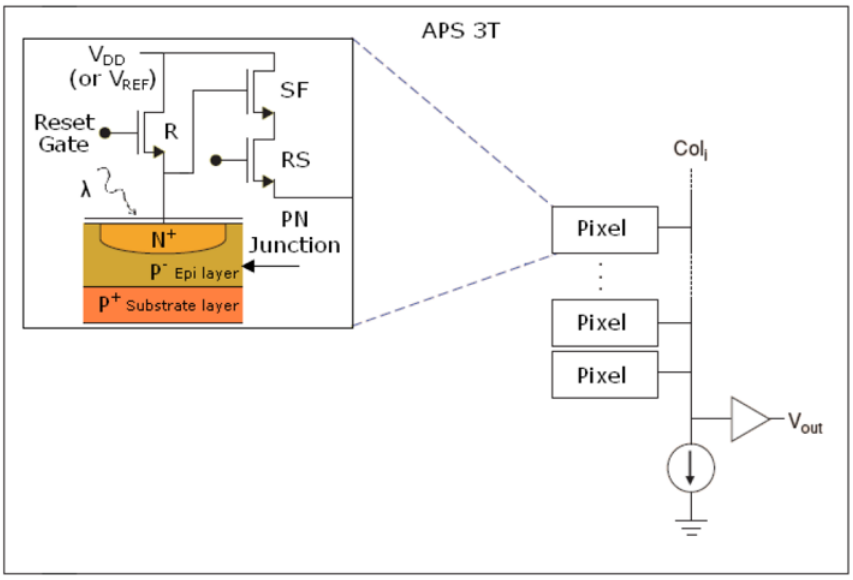

Figure 1.2: A schematic showing the APS 3T pixel and readout architecture [34].

origin of the name 'active pixel sensor' [26].

1.3 Measurement of radiation detector performance

In radiology, the balance between the system performance and patient dose determines the image quality. Accordingly, the finest imaging system is the system which guarantees adequate image quality whilst keeping the patient's radiation dose as low as reasonably achievable [35]. The detective quantum efficiency (DQE) is a widely recommended concept used in order to indicate the image quality in many studies [35–38].

Generally speaking, the DQE describes the transmission of the signal to noise ratio in a digital X-ray imaging detector [38]. Until 2002, there was no international standard measurement for this parameter, and in 2003, the International Electrotechnical Commission (IEC) issued a standard method for DQE measurement. This included two specific metrics: (i) noise power spectrum (NPS); and (ii) modulation transfer function (MTF) [38]. Based on the literature, the physical performance of the imaging detector represented by DQE deteriorates due to increasing noise more than the resolution reduction as a function of the spatial frequency [3, 38–47].

1.3.1 Pre-sampling modulation transfer function (pMTF)

The sharpness or resolution is a key factor in terms of image quality for medical images. It refers to the ability of a medical imaging system for distinction in relation to the neighbouring detailed features of an object [21, 48]. In other words, it describes how much the medical image is blurred, and this blurring can be measured by modulation transfer function, or pre-sampling modulation transfer function (pMTF) [21]. As stated in [49], the pMTF is the MTF of the digital detector before the sampling process: this results in minimising the issues introduced by aliasing. The pMTF is the signal resolution of a detector as a function of spatial frequency; the DQE is proportional to the square of pMTF [37, 50].

The pMTF can be measured by three main methods: a translucent edge test device [48]; a slit test device [51]; and, the opaque edge test device. The last method is the one recommended by the international standard IEC 62220-1 [3]. Each of these methods have been discussed and evaluated by [39]. It has been found that the opaque edge test device method recommended by the IEC estimates lower values of the pMTF than the slit test device method used by [51] by $4.0\% \pm 0.2\%$. It also produces a higher pMTF than the translucent edge test device method used by [52] by $0.7\% \pm 0.4\%$. It has thus been concluded that the measurement method has a noticeable impact upon the pMTF measurement. To that end, it has been suggested that the opaque edge test device should be used in order to obtain a pMTF value reflecting the best overall performance of the imaging system [3, 39].

The pMTF curve translates the amplitude of the sine waves, and the system resolution always degrades as the details increase (see Figure 1.3) [53]. It is known that the frequency corresponding to 10% MTF describes the limiting resolution of a system considering that the human eye cannot observe minute details below 5% to 10% [34].

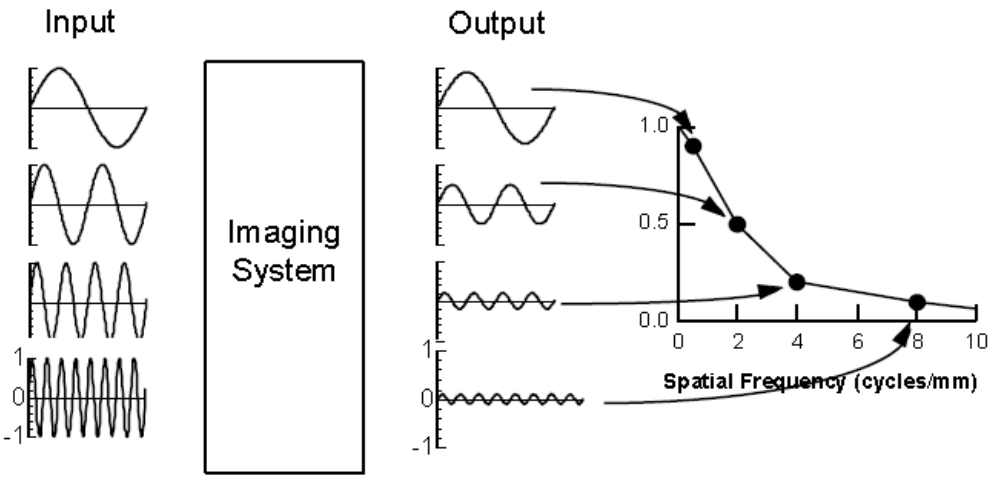

Figure 1.3: The pMTF measures change in the amplitude of sine waves [53].

1.3.2 Normalised noise power spectrum (NNPS)

Noise is a prevalent issue in radiographic images. It is defined as unwanted image details, or random fluctuations [54]. These obscure the region of interest (ROI) in the medical images: hence, noise is considered as a significant obstacle in small object detection. The noise is classified into anatomical (e.g., ribs in chest images) and radiographic noises [48, 55, 56]. The radiographic noises are the two main categories classified as quantum noise, this can also be referred to as random noise, and fixed pattern noise. The former type varies from image to image given that it occurs due to statistical fluctuations of the X-ray source; the latter type is constant for all images due to the non-uniformity photo response of pixels within the detector. Also, image noise can be due to random generation of electrons in the depletion region in the detector, as will be discussed in detail in section 1.3.2.1 [48].

Noise can be determined by the normalised noise power spectrum (NPS). Many scientific sources define the NPS as the Fourier transform modulus of the overall noise. It describes the noise variations in an image as a function of spatial frequency (see Figure 1.4). NPS is the second important metric for calculating the DQE, and is inversely proportional to the DQE [4, 37, 57].

It is recommended by [57] to calculate the DQE using the averaged normalised

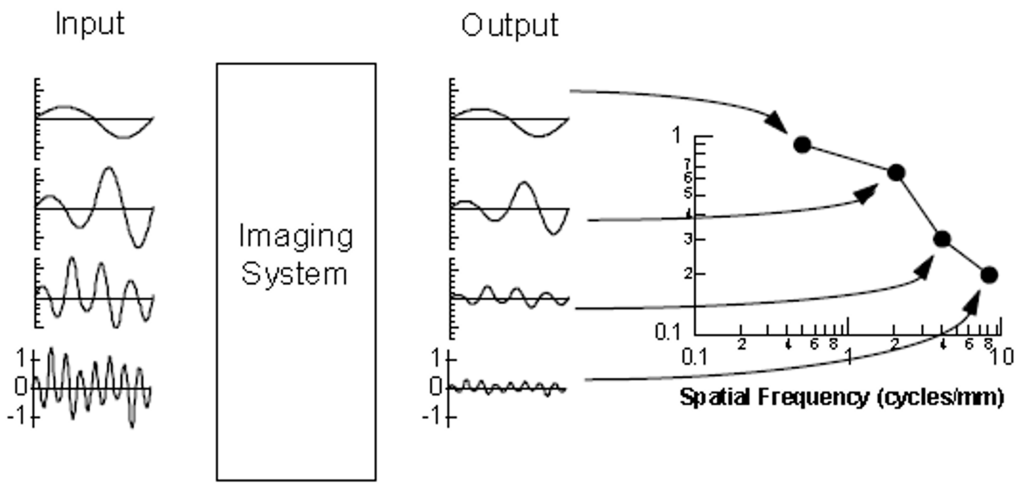

Figure 1.4: The NNPS measures change in the amplitude variation of sine waves [53].

NPS (NNPS) rather than averaged NPS values. It is claimed that NNPS provides more accurate DQE figures because the NPS measures the absolute noise that determines the magnitude of the absolute fluctuations of an image (i.e., pixel standard deviation) whereas NNPS provides information of fluctuations in magnitude relative to the image mean signal (i.e., the pixel standard deviation divided by mean signal).

1.3.2.1 Noise sources in radiation detector

The radiographic noise arises from quantum noise, structure noise, and also electronic noise including read noise and dark current (see Figure 1.5) [29].

Quantum noise:

This is also known as shot noise and random noise. It can be divided into primary and secondary quantum noises, and both are related to the Poisson distribution of the number of X-rays absorbed by the radiation detector. However, each one occurs at a different stage. It is proportional to the square root of the number of photons [29, 34].

Structure noise:

Structure noise, also known as fixed pattern noise (FPN), describes the fixed variations gain within the detector: in other words, the variations in the output signal for

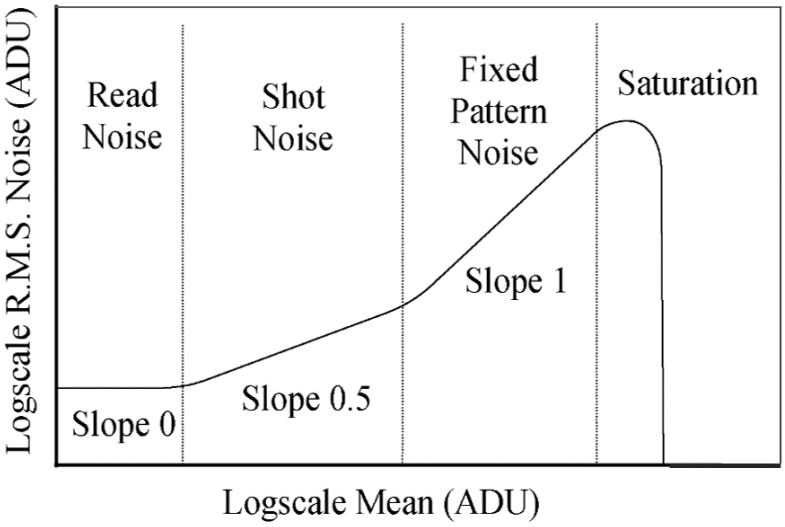

Figure 1.5: Photon-transfer curve displaying all noise sources, limited by read noise at low illumination, shot noise at mid illumination, and fixed pattern noise at high illumination prior to saturation [29]. ADU: analog-to-digital units, RMS: root mean square.

a given input quantity [29, 34].

Electronic noise:

Electronic noise arises from electronic components within the detector. This includes the readout noise and the dark current. The former may be due to transistors and amplifier noises; the latter is due to thermal charges generated in the photodiodes. This type of noise appears both in the absence and presence of the illumination [29, 34].

1.3.3 Detective quantum efficiency (DQE)

Detective quantum efficiency (DQE) demonstrates the effectiveness of input X-ray fraction quanta that is used for image signal to noise ratios as a function of spatial frequency. This, therefore, means the DQE expresses the imaging system capacity to use the obtainable input X-ray quanta [4]. The DQE is expressed by the following equation (1.1):

$$DQE(f) = \frac{pMTF^2(f)}{\frac{\phi}{K_a} K_a NNPS(f)} \tag{1.1}$$

Where NNPS is normalised noise power spectrum and pMTF is pre-sampling modulation transfer function. The photon fluence (ϕ) was provided by IEC 62220-1, whilst the K_a is air-kerma measured at detector surface.

1.3.4 Other parameters affecting the image quality

- The scintillator: Cesium Iodide activated with Thallium (CsI(Tl))

  The performance of any detector system should be considered both in terms of the scintillator CsI(Tl) and the sensor given that there are additional factors which might degrade the image quality. The modern form of imaging systems contain CsI(Tl) with a needle-like (columnar) structure in their construction: this part of the imaging system called the X-ray scintillator. The columnar structure of the CsI provides organised channels for light photons resulting from X-ray interactions within the scintillator which leads to great image resolution [58, 59]. In terms of the cost, the columnar CsI is more expensive than the powdered phosphor gadolinium oxysulfide which is commonly found in MV detectors, and where the image resolution is poor at any rate due to the dominant factor of Compton scattering [60, 61].

- CMOS sensor inherent non linearity

  Despite the numerous advantages of CMOS technology, this kind of sensors suffers from inherent non-linearity, unlike the charge-coupled device (CCD technology. This is a result of either:

  - Sensitivity non linearity; or,
  - Gain non linearity

  The last source can be well controlled in CMOS sensors, whilst the former has a significant impact upon CMOS sensors' non-linearity. CMOS non linearity may indirectly affect the sensor performance. Both have been discussed in

detail by [34].

1.4 Monte Carlo (MC) system building

Linear accelerator (linac) is a machine used in radiotherapy departments to produce high energy photons in the megavolt (MV) range. Henry Kaplan and Edward Ginzton began building a first medical linear accelerator in 1952. Later in 1956, the first patient suffering from an eye tumour was successfully treated using the high energy radiation and he lived the remainder of his life with his vision intact. Today, in the marketplace there is a list of linac suppliers: Varian (USA); Elekta (Sweden); Philips (Netherlands); GE Healthcare (UK); Toshiba and Mitsubishi (Japan); and, Huiheng Medical and HAMMING (China) [62].

- **Linac head structure**

  The linac structure is complicated, but the essential linac components are: an electron gun; an accelerating wave guide; electron beam transport; and, the treatment head (see Figure 1.6). The treatment head is the most significant part for the simulation: therefore, it will be discussed here in detail.

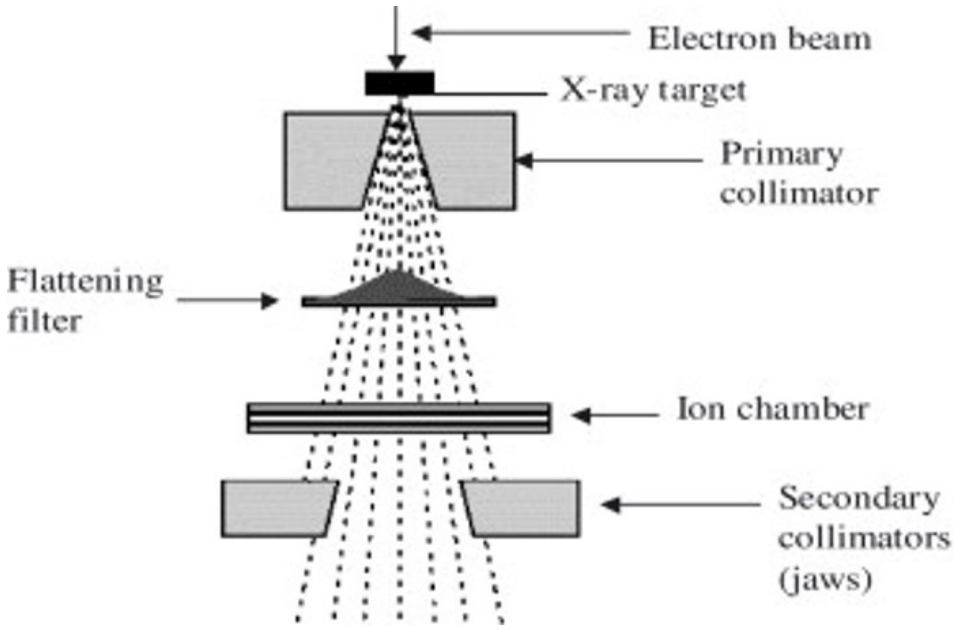

Figure 1.6: Typical Varian treatment head [63].

After the electron beam is accelerated and bent into a specific direction through the accelerating waveguide, the beam will hit a thick target which is made of a high atomic number (Z) material. This is to ensure the interaction between the electron and the target and produce high energetic photons. The primary collimator comes next to absorb the unwanted photons and reshape the beam. Usually, it is made of tungsten (W) since it has a high Z number and thus a high attenuation coefficient. This is followed by the flattening filter which uniformly distributes the forward peaked photon beam to achieve a flat beam. It can be made of lead (Pb), tungsten (W), uranium (U), steel, aluminium (Al) or a combination of these materials [64, 65].

Subsequently, the flattened beam is incident on the monitoring system which consists of four ion chambers measuring the beam dose in monitor units (MU) and ensuring the beam transverse and radial symmetry. The transverse and radial orientations are at 90° to each other, and both are perpendicular to the radiation beam itself. The ion chamber is also used to provide feedback on the linac disability in delivering the planned dose. Next, the mirror comes to project and replicate the radiation beam by optical lights in order to show the position of the radiation beam. The mirror is carefully aligned to a specific angle with the beam, and it is then removed out of beam path when linac is in use [64, 65].

Following this, the movable secondary collimators (which are also called jaws) are brought into use. They are two blocks forming the upper jaws in the y-direction, and the other two blocks in x-direction form the lower jaws. The main job of these jaws is to create a rectangular or square field. They are usually made of Pb or W. Finally, the multi-leaf collimators (MLCs) are added later to linac. These are made of similar material to the jaws and are composed of a number of leaves (e.g., 82, 120, and 160) so as to conform the radiation field matching the tumour shape. Each leaf can be controlled individually. Every linac manufacturer has different MLC design and configurations [64, 65]. Each of these components have been accurately studied in

terms of material, thickness, positions, angles, length and orientation in order to reach the optimum outcomes.

- **The percentage depth dose (PDD) and lateral profiles**

  The PDD is the absorbed dose in a medium as deposited by a radiation beam parallel to the central axis operating as a function of depth. It consists of several areas. The first area is referred to as the 'build-up region' which is the area between surface to D_{max}. Following the D_{max} parameter (which is the highest dose at a certain depth, and which becomes deeper as the energy increases), the curve decays to the last part of the PDD curve and is referred to as the 'exit dose' as shown in Figure 1.7 [66].

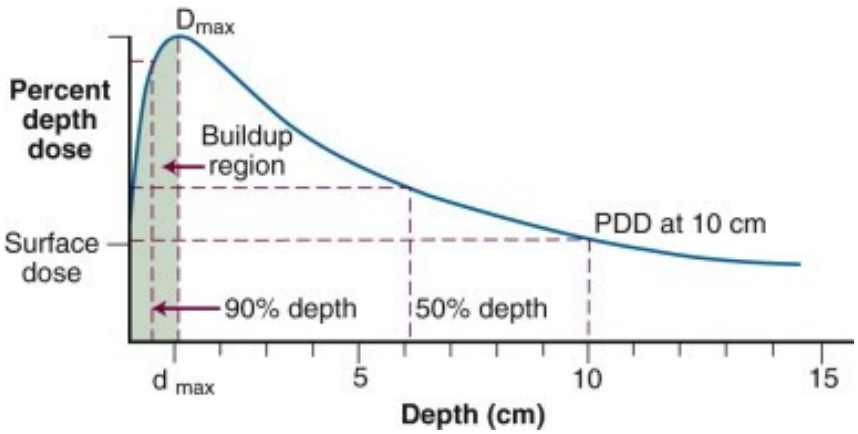

Figure 1.7: The PDD of a radiation beam [66].

The beam profiles provide information regarding dose as a function of a given depth within a medium contrasted to the distance from the beam central axis in x or y orientations, and perpendicular to the radiation beam. It consists of three main regions which are the central region, the penumbra region, and the umbra (toe) region (see Figure 1.8). The central region represents the central portion of the radiation profile to beam field edges by 1 to 1.5 cm. The penumbra is the region near the edges of the geometric field where the dose drops quickly and is affected by the collimators. The Umbra or toe is the area outside the beam, and the dose in this region comes via radiation transmitted through the MLCs and treatment head-shielding. It is considerably low [67].

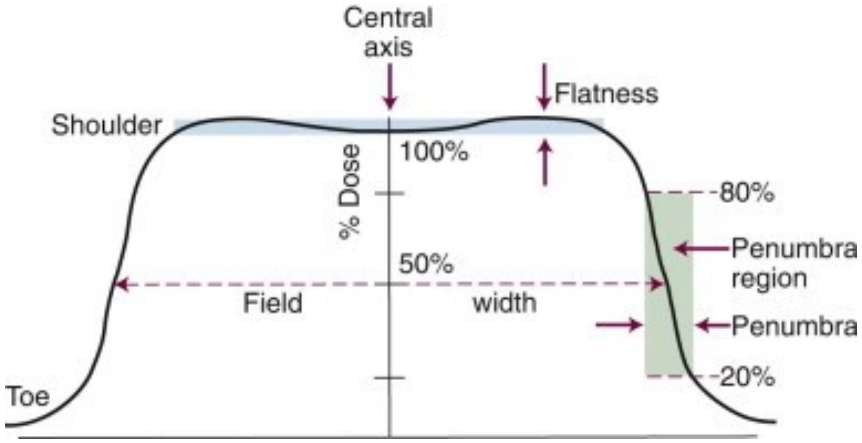

Figure 1.8: The lateral profile of a radiation beam [66].

1.4.1 Computer simulation: the Monte Carlo simulation

Computer simulations are a method to study the clinical setting by mimicking and modelling clinical experiments, or a real-world phenomenon in a computational environment via a vast number of random events [68, 69]. The main advantages of such method are providing access to experiments at any time and thereby testing the merits of alternative methods without having to physically build the system. In radiation therapy units, computerised simulations are much cheaper than the clinical experiments where the radiation source (such as linac) can cost around £1.5 million and where the priority goes to treating patients rather than experiments for research. Nevertheless, an adequate computer, in terms of memory space and speed, is required since some simulations necessitate intensive computational processing [70].

The computer simulation is classified into two categories based upon the randomness degree associated with simulator behaviour. The first depends on random behaviour: hence, it is referred to as a stochastic system. In contrast, deterministic system behaviour incorporates absolutely no randomness: such systems are beyond the scope of this thesis [70].

The most popular algorithm is the Monte Carlo (MC) simulation which uses random numbers in a determinative manner in order to perform statistical analy-

ses (i.e., it is based on a stochastic system). It is considered to be an appropriate model for dose distribution and particle tracking thanks to its ability to govern the individual photon and electron interactions with the patient, and track their transport within the patient. Additionally, the MC algorithm can be utilised to model a radiation beam [66].

The simulation begins with modelling the desired system and the user defines the number of repeats which usually ranges from 5×10^{10} to 50×10^{10} replications (which are also called 'histories'). The simulation is then executed in order to acquire the statistical estimations (the simulation outputs) with low uncertainty. Monte Carlo integration generally has an error variance of σ^2/n, where σ^2 is the variance (standard deviation (σ) to the power two) and n is the number of replications. This means that sampling larger n leads to superior statistical analysis. The replication number determines the simulation speed along with the demands the simulation places on the central processing unit (CPU), however, applying variance reduction techniques can help to reduce the simulation time dramatically [71]. This aspect will be discussed later in variance reduction techniques in section 1.4.2.2.

1.4.2 EGSnrc introduction

Electron gamma shower (EGS) is a software toolkit and platform which is used to run the MC simulation of radiation interaction and transport. It was developed by the National Research Council (NRC) in Canada by several programmers [72], and is available online for free (including extensive user manuals).

The EGSnrc package contains diverse applications for radiation transport modelling and data analysis. The common two codes are BEAMnrc and DOSXYZnrc, whilst other analytical codes, like beamdp and statdose, are also utilised.

- **BEAMnrc**

  BEAMnrc is known for its uses within linac modelling. It has the capability of adding linac geometries such as target, ion chamber, mirror, jaws, and

MLC for a specific linac brand in addition to its ability to perform dynamic MLC (leaves are moving while the radiation is delivered) and jaws (time-synchronised). The main output of the BEAMnrc simulation is phase space file (PSF), accompanied with an output listing (.egslst) and also a log and graphics file (.egslog). The PSF is a binary file that stores information about particles regarding their energies, positions, and momentum. Such a file can be used to improve the simulation efficiency by scoring it behind patient independent components. These components have the same positions and dimensions for all patients, namely: target; ion chamber; mirror; whilst; jaws; and, MLCs are considered patient dependent components since they alter depending on the patient being examined. The PSFs can be used in the DOSXYZnrc or BEAMnrc simulations as a radiation source if they are scored underneath patient independent components [64, 73, 74].

- **Beamdp**

  Beamdp is another beneficial EGSnrc user code: it stands for 'beam data processor'. This code gives the BEAMnrc users the capability to analyse the resultant phase space file and derive the desired data, such as energy fluence, spectral distribution, and angular distribution. It can also combine two PSFs into one. There are eleven options given by the user code [73].

- **DOSXYZnrc and statdose**

  DOSXYZnrc is ideal for dose calculation in a voxelised phantom. It allows users to select and synchronise the source model. The DOSXYZnrc simulation generates a data file called '3D dose file' (with extension .3ddose), an output listing, and a log and graphics file. This program permits the user to define the phantom using either CT images in Digital Imaging and COmmunications in Medicine (DICOM) format or as non-CT data input (thus creating the phantom manually by inserting the material densities). The software can read the DICOM only when the Hounsfield units (HU) are converted to density, and with a file extension of .egsphant, in 3D geometry [75]. It is worth noting that EGSnrc has a fixed unit system: namely, the length and distance

are in cm and the dose is always normalised in Gy/ particle.

Given that the lateral profiles and depth dose curves have received widespread attention, EGSnrc has distributed a tool giving the opportunity to gain such data using a specific command line in EGSnrc environment. The tool is called 'statdose', which is an analytical code helping to extract data from the 3D dose file obtained from the DOSXYZnrc simulation [74].

The user interacts with the software via an input file with the .egsinp extension. It includes five blocks of main input parameters, namely: source geometrical configuration; particle transport; EGS; components modules (BEAMnrc) or phantom (DOSXYZnrc) geometrical configuration; and, MC control [64]. Each line in the input file corresponds to a specific parameter as explained in the manual. The BEAMnrc and DOSXYZnrc are linked together by the PSF, as illustrated in Figure 1.9. Both BEAMnrc and DOSXYZnrc codes are written in MORTRAN3.

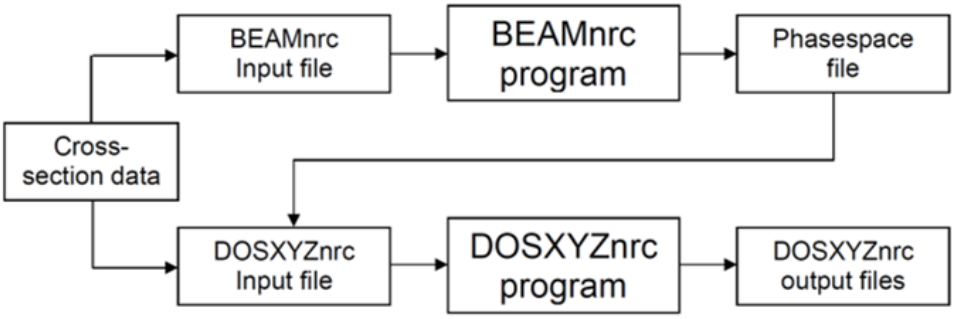

Figure 1.9: The link between BEAMnrc and DOSXYSnrc [64].

1.4.2.1 Simulation uncertainty in EGSnrc

The results in EGSnrc are associated with statistical uncertainty being used to express a standard deviation, whereas the simulated number of events can be any number less than infinite ($< \infty$) [76]. As previously stated, acquiring an adequate statistical result requires a high number of events (n) and it is directly proportional to the calculation time (T) which, in turn, is inversely proportional to the efficiency (ε) as ε is defined (1.2):

$$\varepsilon = \frac{1}{s^2 T} \tag{1.2}$$

Here, s is the estimated variance (σ^2). In order to address the calculation speed issue whilst maintaining the efficiency, variance reduction techniques (VRTs) have been proposed for minimising statistical variance for specific computation time [77, 78].

1.4.2.2 Variance reduction techniques in EGSnrc

- **Transport cutoffs:**

  Transport cut-offs are, by far, the most effective and common techniques used to improve calculation time. This is done by setting the electron and photon cut-offs energies (in which the particles are eliminated) at levels where they are unlikely to be able to contribute to the result [79]. The cut-off energies for photons and electrons have been studied, and it has been concluded that for photon cut-off, it is suggested to set it from 0.005 to 0.1 MeV; for electron cut-off, the range is 0.1 to 1.0 MeV. It is noticeable that the cut-off for photons is less than electrons since photons, unlike electrons, tend to travel longer relative distances despite their low energy [79].

  In EGSnrc, the photon cut-off is symbolised as PCUT which stands for global photon cutoff energy and electron cut-off appears as ECUT, a short form of global electron cutoff energy [73].

- **Electron range rejection:**

  This parameter is frequently invoked in linac modelling, and is used to terminate an electron with insufficient energy to exit the current boundary. The energy should be set at a level where the bremsstrahlung has an insignificant effect and cannot travel nor deposit energy far away from the original site. The common values for this energy are from 2 to 3 MeV. Thus, any electron with an energy above this range will not be rejected because it is able to escape the region and thereby reach the scoring region, or it can produce bremsstrahlung which can also do this [73, 79].

- **Bremsstrahlung splitting and Russian Roulette:**

  Bremsstrahlung splitting helps to boost and augment the bremsstrahlung (brem) photon production from primary electron collisions (in the target range) within the linac. In this manner, each event will not produce only one brem photon, but numerous photons determined by the number of bremsstrahlung splitting value (NBRSPL). Each photon will have a weight of $NBRSPL^{-1}$. This parameter has three options: Selective (SBS); Uniform (UBS); and, directional (DBS). All three are available in the BEAMnrc, but SBS is excluded in DOSXYZnrc. All the three usually work in conjunction with Russian Roulette (RR): this governs the secondary charged particles' interactions and optimises the bremsstrahlung splitting.

  - *Selective Bremsstrahlung Splitting (SBS):*

    Although the electrons have a high chance to emit the brem photon forward (aiming at the field of interest), there is also a chance to emit it in all directions and to be absorbed by the linac components. This causes a decrement in photon numbers arriving below the jaws. Selective bremsstrahlung splitting was developed in order to overcome the photon absorption issue in linac components: hence, it is only available in BEAMnrc (for linac modelling). It solves this issue by varying the bremsstrahlung splitting based on pre-calculation of the probability for various incidents of electron directions. The drawback of this option is that it creates an uneven distribution of photon weights which, in turn, causes low efficiency [73, 78].

  - *Uniform Bremsstrahlung Splitting (UBS):*

    By applying the UBS, each event will uniformly produce NBRSPL photons with a weight equal to $NBRSPL^{-1}$ for each photon, multiplied by the electron energy that is responsible for that particular bremsstrahlung event. It is highly recommended to apply Russian Roulette (RR) in parallel in order to speed up the simulation and control the secondary charged particles. The secondary particles subject to RR are those elec-

trons resulting from photoelectric, Compton, and pair production events.

- *Directional Bremsstrahlung Splitting (DBS)*

  The DBS has the same concept as the SBS, whereby the brem photons directed to the field of interest are split whilst those intended away from the field are not split, according to field size and the source to surface distance [78]. The resultant photons have the weight of $NBRSPL^{-1}$ (this is referred to as a non-fat photon). If the photon has weight higher than $NBRSPL^{-1}$, the RR will be applied on these photons so as to eliminate them since they tend to interact above the field of interest, and then undergo Compton scattering into the field, thereby compromising the statistics. This technique is the most efficient when simulating small field sizes as proven by [80].

- **Photon interaction forcing:**

  This technique is probably less beneficial in linac modelling since the target has a high atomic number (Z) (i.e., the photons tend to interact readily with high Z materials, with no need for forcing). As the name suggests, this technique forces the photons to interact with linac component modules (CMs) and split according to pre-defined input variables of the maximum photon interaction number (NFMAX) [79]. If the primary photons are forced to undergo NFMAX interactions, the remaining number will be passed onto secondary photons.

1.4.3 MC application

Recently, MC has been increasingly used thanks to improvements in computational efficiency and quality. This has helped to solve many problems in radiotherapy. Consider the following examples [81]:

- Fluence and spectrum calculations;
- Dosimetric parameters, for instance, stopping powers;

- Correction factors such as back scatter factor and peak scatter factor;
- Dosimeter response simulations;
- Treatment head simulations;
- Treatment planning dose calculations;
- Beam delivery and dosimetry verification.

With regard to radiotherapy treatment planning, MC is in currently used to calculate the dose of the radiation beam incident on the patient by simulating the transport of the particles through the patient and thereby scoring the absorbed dose in a PSF. The PSF, as previously discussed, has information on radiation particles including electrons, photons, or positrons. This information is needed in order to initiate the particles transport at the patient surface. For the clinical beam, this measurement is difficult if not impossible, to obtain directly. This is due to some obstructing factors, two of which are the availability of suitable detectors to perform this kind of measurement and the high radiation intensities. Thus, MC-based software is currently the choice tool for patient dose calculations [82].

1.5 Gamma analysis

One of the most famous metrics for dose distribution comparison in radiotherapy is the gamma index (γ- index). Gamma analysis was introduced by Low et al. in 1998 [83]. Two-dimensional (2D) gamma analysis has been modified and extended later into a third-dimensional axis (i.e., 3D gamma analysis) [83, 84]. The comparison is established between two matrices, one of marked as a reference (measured) matrix, whilst the other is marked as a target (evaluated or calculated) matrix. This tool measures the numerical difference between these matrices in terms of the variety in the dose, and space via the dose difference (DD) and distance to agreement (DTA) methods. The dose difference (DD) is a straightforward tool of dose evaluation between the evaluated matrix points and corresponding points in the reference matrix.

However, the DTA calculates the distance between a point in the reference matrix and the nearest point in the target matrix with the same value [83]. For each point (r_m) in the reference matrix, the gamma-index $(\gamma(r_m))$ is defined by the following equation (1.3):

$$\gamma(r_m) = \min\Gamma(r_m, r_c)\forall(r_c) \tag{1.3}$$

where $\Gamma(r_m, r_c)$ is defined by the following equation (1.4):

$$\Gamma(r_m, r_c) = \sqrt{\frac{\mid r_c - r_m \mid^2}{DTA^2} + \frac{(D_c(r_c) - D_m(r_m))^2}{DD^2}} \tag{1.4}$$

and $\forall(r_c)$ means for all (for every), $\mid r_c - r_m \mid$ is distance difference between the two voxels r_c in the calculated matrix and r_m in the measured matrix. The $D_c(r_c) - D_m(r_m)$ is the dose difference between the same points.

Therefore, the pass/fail criterion is mathematically determined by:

$$\gamma(r_m) \leq 1, \text{ calculation passes,}$$

$$\gamma(r_m) > 1, \text{ calculation fails.}$$

The user defines the passing criteria for DD and DTA which is usually written in this form DD (%)/ DTA (mm).The commonly used criteria in radiotherapy are 1%/ 1 mm, 2%/ 2 mm or 3%/ 3 mm. This is based on the size of the tracked error [85, 86].

1.6 Head and neck anatomy

The pharynx is an anatomical part of the head and neck area. It is the common path for swallowing and respiration. It is divided into three main regions: the nasopharynx; the oropharynx; and, the laryngopharynx (according to the neighbour organ). The nasopharynx is the upper airway system component, linking the nasal cavity to the laryngopharynx and then the trachea (through the oropharynx) as shown in

Figure 1.10 [87].

Nasopharyngeal cancer is considered a rare cancer type amongst people in the United Kingdom, according to the National Health Service (NHS). As the name implies, it affects the nasopharynx region, behind the nasal cavity [88]. Patients with nasopharyngeal cancer frequently receive a combination of radiation therapy and chemotherapy for the nasopharynx area and neck lymph nodes. If the suggested treatment does not cure the lymph nodes, surgery can be an option to remove the nodes [89, 90].

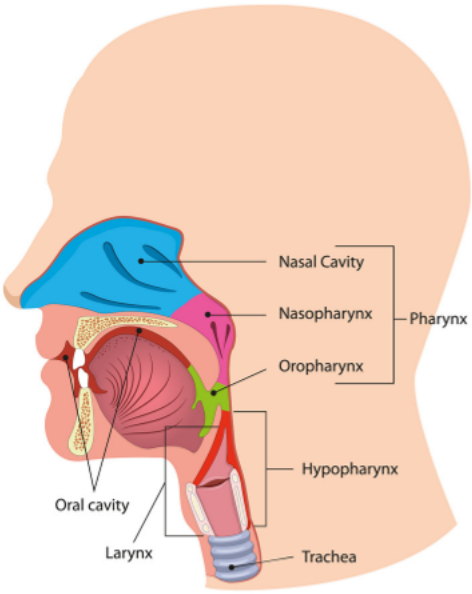

Figure 1.10: Head and neck anatomy [87].

Radiotherapy, however, has a number of side effects depending on the part of the body being treated. For head and neck radiotherapy, patients may suffer from overall fatigue, headache and swallowing difficulty due to parotid glands shrinkage and lack of saliva [91]. As demonstrated in Figure 1.11, the parotid glands are the largest salivary glands which provide the mouth with 60% to 70% of saliva (in collaboration with other salivary glands) in order to keep the mouth moist for better chewing, swallowing, and digestion [92]. Furthermore, saliva functions to minimise dental decay. Hence, a reduction in saliva production can affect life quality since a lack of saliva causes mouth dryness, medically known as ‘xerostomia’. This can

lead to multiple problems: taste alteration; oral infections; dental caries; and, oral pain in general. Moreover, as mentioned previously, saliva plays an important role in digestion and xerostomia definitely generates difficulty in chewing and swallowing [93].

The parotid glands are located in the anterior and inferior of both ears, on the surface of each cheek. This means that they are overlapped with nasopharyngeal and oropharyngeal regions and are therefore exposed to radiation during treatment [92].

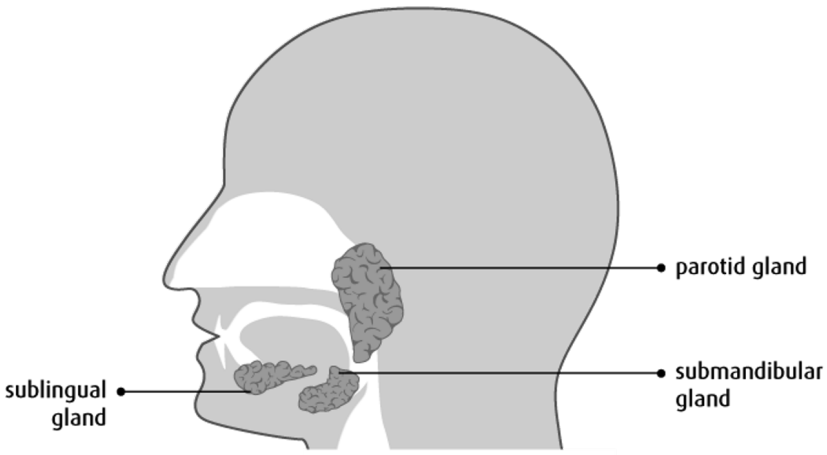

Figure 1.11: The salivary glands anatomy [92].

Radiation causes a reduction in parotid glands volume, as has been clinically proven by many studies. For instance: [91, 94–96]. Normally, the parotid glands have a volume of 16.99- 20.98 cm^3 for adult males, and 13.91- 16.70 cm^3 for adult females. Radiation can lessen their volume by up to - 70% (minus sign is used to indicate a reduction) of the total volume depending on how they are affected by the treatment plan [97].

Sinuses

The paranasal sinuses are four paired air-filled cavities in the human head. They are named: maxillary; frontal; sphenoid; and, ethmoid. This corresponds to the bone wherein they are located. Figure 1.12 shows the sinuses' anatomy and location [98]. Their main functions are: lightening the skull; enhancing immune defences within

the nasal cavity; humidifying inhaled air; increasing voice resonance; and, it also gives shape to the skull and eyes [99]. In case of inflammation, the mucus inside the nasal cavity and paranasal sinuses becomes dry, thick, and filled with fluid instead of air [98, 100]. This alters the head anatomy and should be taken into account during radiation therapy in relation to accurate dose calculations [101].

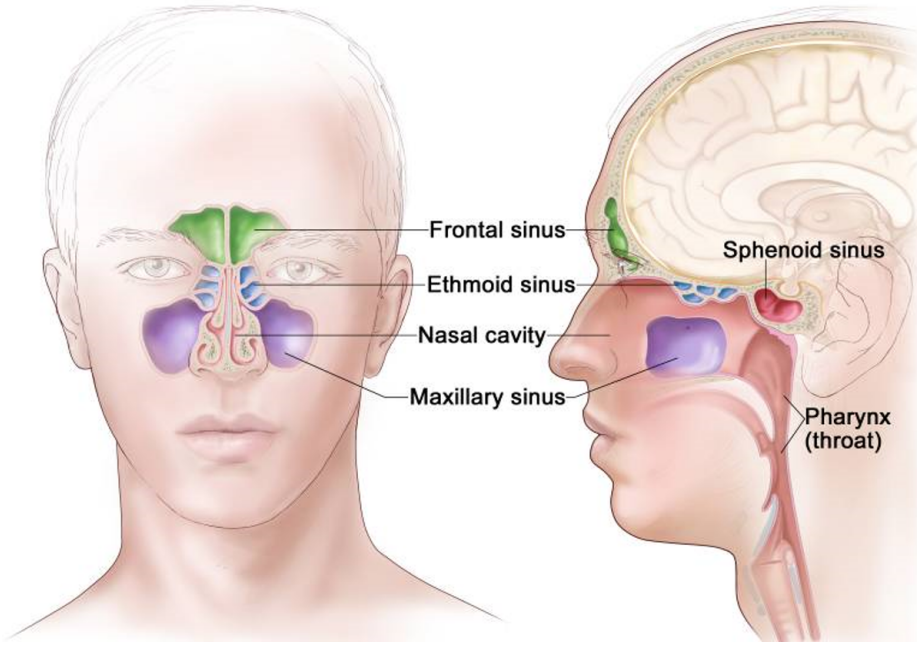

Figure 1.12: The anatomy of paranasal sinuses [98].

1.7 Anatomical changes during radiotherapy for head and neck cancer, and detection

Radiotherapy for head and neck cancer remains a crucial treatment modality despite its side effects. Radiation can substantially alter a patient's tumour but also normal tissues during a course of treatment. This often results in differences between intended radiation dose and delivered dose: furthermore, differences in dosages to organs risk causing under-dosing to the tumour and/or overdosing to critical normal tissues [102]. The organs at risk are tissues which, if irradiated, may suffer major morbidity and therefore affect the treatment plan and dose prescription. They can be divided into five main groups: optic structures; intracranial structures; swallow-

ing related structures; structures related salivation; and, brachial plexus (a bundle of nerve roots in the neck). In order to protect these at risk organs and avoid complications, a dose limit has been set and defined for each organ [103–106].

The common changes reported in head and neck patients are tumour and/or node shrinkage, parotid glands shrinkage, and weight loss during treatment [102]. Weight loss has a significant correlation with parotid gland volume loss, as proven in [107]. The parotid gland volume varies over the treatment period in relation to whether the gland is located at the beam entrance or exit. For IMRT, it has been reported the volume is reduced downwards by 5%, 23%, 32%, 34%, 37%, 45% and 58% with an average volume loss of 43.5% for the ipsilateral parotid gland (at the beam entrance). Likewise, the volume has been observed to reduce downwards by 2%, 16%, 23%, 29%, 36%, 39% and 41% with an average volume loss of 44% for the contralateral gland (at the beam exit). These results were taken over a seven week treatment period using cone beam computed tomography (CBCT) images every other day for ten patients with head and neck cancer. This implies that the volume loss rate per day for the glands is about 1.5% [108]. Such changes require the treatment plan to be adapted in order to account for these changes, and this process is called adaptive radiotherapy (ART) [109]. However, there is no international standard nor a limit for volume loss during radiotherapy as to when ART is deemed to be necessary. In the case of parotid glands, it has been suggested to consider re-planning when the volume is reduced by 24 - 30%, which is more likely to occur during the third week of treatment for first time by [108]. EPID has been utilised in order to monitor and detect other changes in different cancer cases [110–113]. EPID offers an efficient means of identifying anatomical changes for both lung and prostate cancer patients. For lung cases, the detected progressive changes were 57%, and random changes were 37% (in 81 patients). The changes were mainly due to a dose increase to the lung as a result of tumour shrinkage. Random changes were dominant in prostate cases at 82% (in 34 prostate cancer patients). These changes came from gas pockets located in the rectum [113].

There are several methods and tools used to detect anatomical changes caused by radiation. The kilovolt cone beam computed tomography (kV-CBCT) images taken during treatment can report the changes by comparing them to the treatment planning (pCT) images taken before the treatment (i.e., those used for planning) [114]. The contoured kV-CBCT images can also be evaluated against the dose histogram produced by the treatment planning system [108]. Mega-voltage CT image-guidance (MVCT-IG) via tomotherapy can also be used for tracking changes via contouring the images and comparing them with the dose histogram [102]. Tomotherapy is a radiation therapy modality that combines treatment planning, CT image-guided patient positioning and treatment delivery into one integrated system. In vivo dosimetry is also used to estimate anatomical changes: this is done by positioning dosimeters (such as diodes or thermos-luminescent dosimeters) on the patient's skin, or within patients, in order to record the dose at a certain point. However, this is not practical and is time consuming. Alternatively, the dose at a specific point inside patients can be reported using EPID and back projection, or dose reconstruction techniques [19, 115]. Nevertheless, the back-projection technique thus far is not functional in large heterogeneities (as in cases with the lungs or thorax). This is a result of using a water-based correction kernel: as such it cannot account for the real scattering conditions within the patient [116, 117]. Another method for tracing the anatomical changes is simply to use the EPID application. The first EPID image captured in the first fraction of analysis can be compared to the other EPID images captured afterwards, and any dissimilarity between them will be detected and reported [113, 118].

It seems that kV-CBCT is a preferable tool for reporting non-rigid changes (i.e., soft tissue related changes) given that the images are of a high quality and high resolution whereas the smallest visible bar group is 0.6 lp/mm [119]. Also, kV-CBCT images can provide a direct comparison to the pCT. However, kV-CBCT tends to suffer from metal artefact interference more than images obtained via MV sources since the photoelectric (photon-electron) interaction, which relies heavily on the pertinent atomic number, is more probable in the kV range [120]. Moreover,

CBCT requires additional equipment appended to linac which makes isocentre of kV-CBCT and MV source is difficult to match [121]. MV-CBCT is a conventional CT approach which uses an MV source and EPID: combine, these overcome the isocenter issue, however, it delivers very high doses to patients, higher than kV-CBCT [121]. EPID is easy to both use and access since it is attached by a supportive arm to most linac machines available on the market [122]. EPID images cannot be directly compared to pCT images, but they can be compared to treatment planning system (TPS) by reconstructing the dose [123]. Additionally, they can be compared to the first EPID image taken in the first fraction of measurement, as previously mentioned. The main feature of EPID is that does not require extra time for setup or radiation doses to patients since images can be obtained during treatment [124]. A summary of the advantages and disadvantages of the tools used for tracking anatomical changes is shown in Table 1.1. Figure 1.13, adopted from [125], shows a linac with the dual implementation of the kV imaging system (kV CBCT) and electronic portal.

The feedback from these tools can benefit adaptive radiotherapy (ART): however, ART retains a paucity of clinical usages despite its effectiveness to ensure better life quality to cancer patients [126]. It is observed that the normal tissue constraint in 50% of 28 cases of nasopharyngeal carcinoma was violated when reimaging at a fraction number 25 [127]. Likewise, it is found that 65% of 23 head and neck patients gain benefits from re-planning [128]. The main challenge facing the ART application is contouring target tumour and organs at risk for each of these plan adaptations. Doing this is time-intensive and creates a heavy workload [129]. Thus, using a simple method such as EPID to trace the changes during the treatment may reduce the workload.

It is reported, by using EPID and 3%/3mm gamma analysis, that 40% out of 55 head and neck cases had medium to important changes, and which occur in the third week of radiation therapy [118]. Similar results were observed by CBCT in [108]. This makes the third week of the treatment the crucial week to observe any

Table 1.1: A summary of main advantages and disadvantages of tools used for tracking the anatomical changes

The model	**Advantages**	**Disadvantages**
kV-CBCT	1) Better soft tissue contrast at low radiation doses. 2) Direct comparison to planning CT.	1) Needs additional hardware. 2) Difficult to match isocentres of kV and MV systems.
MV-CBCT	1) No additional hardware required. 2) Less susceptible to artifacts due to metallic objects. 3) No extra dose to patients.	Poor image contrast and quality.
EPID	1) No additional hardware required but it needs software. 2) Less susceptible to artifacts due to metallic object. 3) No extra dose to patients. 4) Available with most linacs.	Poor image contrast and quality.

critical changes. As a conclusion, the dose verification must be obtained at least once a week, and the adaptive radiotherapy is more likely to be taken into account in the third week of treatment for head and neck cancer patients.

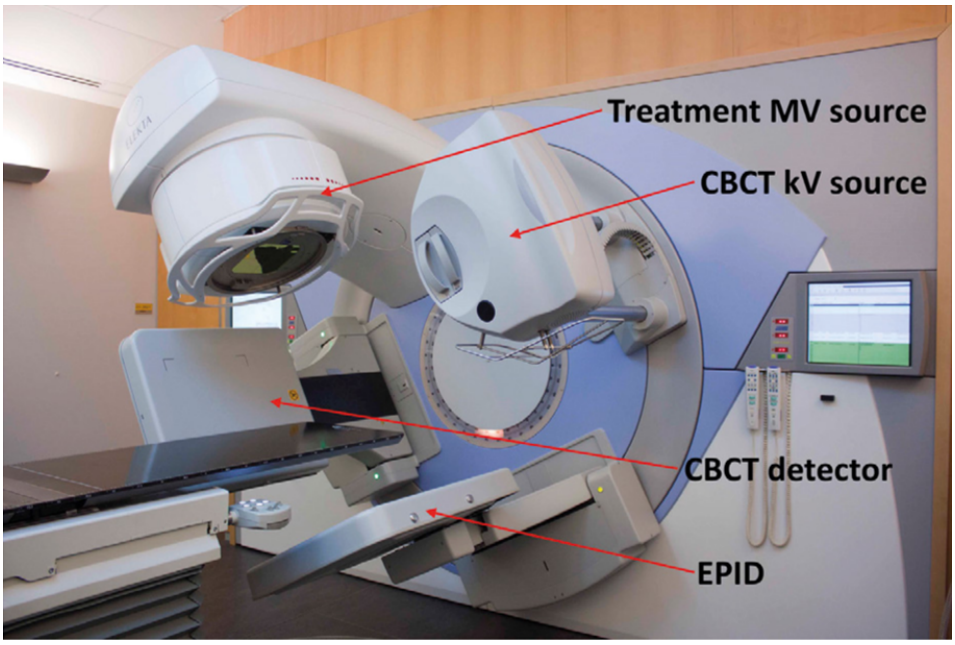

Figure 1.13: A linac with the implementation of kV imaging system (CBCT kV) and EPID [130].

1.8 Dosimetry methods using EPID

The information gained by EPID can be utilised on the basis of clinical needs. There are four main applications for EPID dosimetry, and these can be divided into two main branches [131]. Firstly, the non-transit (i.e., without phantom or patient in the beam path); secondly, transit (whilst phantom or patient are irradiating). The dose calculation for the two branches can be either forward- or back-projected as shown in Figure 1.14 [131]. The direct and conventional method that has been widely used is called 'forward-projection'. A comparison between forward- and back-projection was made, and it was shown that both methods presented a moderate agreement in prostate volumetric arc therapy (VMAT) patients using gamma criteria of 3% and 3 mm [132].

Basically, the forward non-transit dosimetry approach (Figure 1.14, a) is used to ensure that the calculated fluence intensity distribution by the TPS has been correctly transferred to, and delivered by, the linac [131]. The 3D dose calculation resulted from the back-projection non-transit dosimetry approach (Figure 1.14, c)

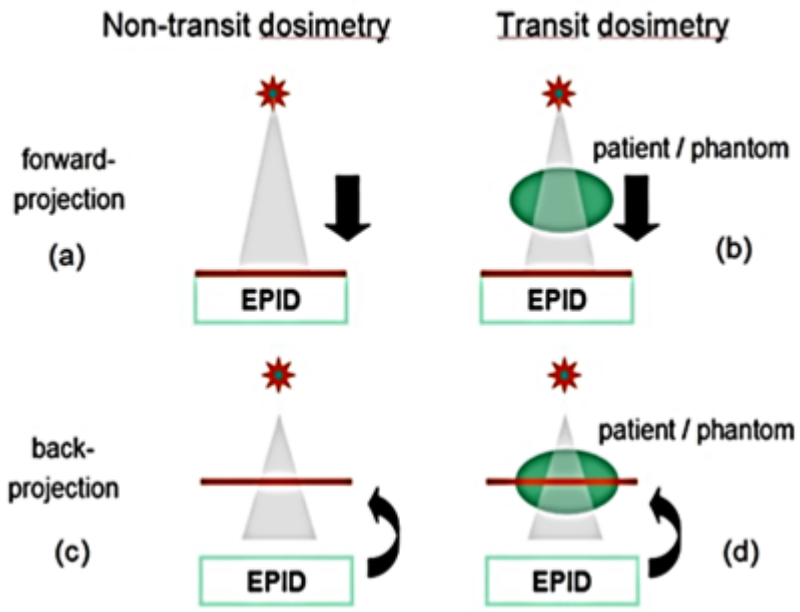

Figure 1.14: Schematic representation for the various dosimetric applications of EPID. The first row represents forward-projection methods; the second row represents back-projection methods. The first column represents non-transit (without patient/phantom) dosimetry; the second column represents transit dosimetry (with patient/phantom) [131].

called 'pseudo-3D' or 'virtual 3D' [131, 133]. These two approaches (referred to as 'pre-treatment verification') help to detect errors arising from dose calculation via TPS or linac, but not errors related to patients wrong positioning or anatomical changes [131, 134]. Transit dosimetry is suitable for patient related errors because it measures the dose after passing through the patient: additionally, it is also able to report the errors related to the TPS or linac [135]. The forward-projection (Figure 1.14, b) performs 2D image comparisons, whilst the back-projection (Figure 1.14, d) performs 3D image comparisons [131].

1.9 The aim of this work and the technical objectives

Detectors are essential in both research and industrial facilities that use radiation beams for diagnostic or therapeutic purposes. To that end, this work was devoted to evaluating radiation detectors for a particular function and assessing their suitability for the suggested function in radiology and radiotherapy departments. Specifically, I will characterise two new detectors named Lassena for the first time. One will be used for CBCT applications and radiology imaging, the other one will be used for MV imaging in radiotherapy departments as EPID. Furthermore, I will examine EPID as an error detector by mimicking real case scenarios of anatomical changes in parotid glands and the maxillary sinus for nasopharyngeal cancer cases.

1.9.1 The technical objectives

- Characterising new radiation detectors named Lassena for the first time. One is used for radiology (kV) applications (such as diagnostic imaging and CBCT); the other is used for radiotherapy (MV) applications (such as imaging and dosimetry purposes). The main features of both detectors are the fine pixel pitch and the thick scintillator which aim to enhance image quality.

- Assessing EPID for dose verification and error detection due to anatomical changes in head and neck cases using EPID images. This is performed via computer simulations and mimicking parotid gland variations resulting from radiation exposure based on cases reported in the literature.

- Evaluating EPID's ability to detect dose discrepancies due to changes in heterogeneous volumes arising from sinusitis in a head and neck case in silico. Furthermore, discussing the limiting factors (including anatomical overlapping and evaluation tools) of the EPID application.

1.10 The structure of this thesis

This thesis contains six chapters. They are organised as follows:

Chapter 1:

A brief introduction of the clinical problems and unmet needs regarding present day detectors and their applications, as well as an explanation of the main terms and parameters used in subsequent chapters.

Chapter 2:

Describes the new detectors' characterisation and performance evaluation according to certain criteria.

Chapter 3

Explains the methodology of building and calibrating a treatment head (linac) using EGSnrc software performing a Monte Carlo simulation.

Chapter 4:

Discusses EPID's ability to detect errors arising from parotid shrinkage in head and neck cases in silico compared to CBCT results from the literature. Additionally, it presents the results of parotid gland variations during radiotherapy observed from published articles in head and neck cases.

Chapter 5:

Demonstrates the computational experiment of creating different case scenarios of sinusitis, and evaluating the EPID sensitivity to these changes. Furthermore, there is a discussion of limiting factors of the EPID application.

Chapter 6:

Provides a summary of the main findings and recommendations for future work.

Chapter 2

Empirical performance evaluation of two radiation detectors

2.1 Overview of chapter

Two radiation detectors, one for diagnostic radiology and another for radiotherapy, were designed by the Rutherford Appleton Laboratory (Oxford, UK). These had the purpose of reducing image noise by enhancing the light production (without sacrificing image resolution) by controlling the scintillator thickness and pixel size. In this chapter, I aim to perform a critical appraisal for the kV radiation detector in terms of its performance and assess its suitability for general X-ray imaging and cone-beam computed tomography (CBCT) applications. This will be done by computing a normalised noise power spectrum, pre-sampling modulation transfer function, and lastly, detective quantum efficiency.

Secondly, the MV detector is tested in terms of linearity, reproducibility, and uniformity. Some suggestions and recommendations are provided for creating an optimal design in order to make the detector usable for dosimetry and imaging applications within radiotherapy. The Rutherford Appleton Laboratory has designed this MV detector in order to overcome the limitations of current detectors since they suffer from poor image quality.

The outcomes of this work resulted in the following:

- **Alzahrani, H.**, Richards, S., Sedgwick, I., Seller, P., Konstantinidis, A., Royle, G., Ricketts, K. (2018, November). Image Quality Determination of a Novel Low Energy X-ray Detector. In 2018 IEEE Nuclear Science Symposium and Medical Imaging Conference Proceedings (NSS/MIC) (pp. 1-2). IEEE. Poster presented.
- **Alzahrani, H.**, Richards, S., Sedgwick, I., Seller, P., Konstantinidis, A., Royle, G., Ricketts, K. (2020). Image quality determination of a novel digital detector for X-ray imaging and cone-beam computed tomography applications. Nuclear Instruments and Methods in Physics Research Section A: Accelerators, Spectrometers, Detectors and Associated Equipment, 968, 163914. Paper publication.

2.2 Hypotheses of chapter

- The kV detector (Lassena) has less noise owing to the thick scintillator and better image resolution arising from its fine pixel size. Therefore, it has better overall image quality compared to other kV detectors evaluated in the literature.
- The scintillator within the MV detector has been modified and optimised in terms of thickness in order to gain sufficient presentation as an imager.
- Lassena (MV) can also act as a dosimeter.

2.3 Criteria of success

Concerning kV detector characterisation, the image quality is evaluated by quantifying the signal transfer property (STP), pre-sampling modulation transfer function (pMTF), and normalised noise power spectrum (NNPS). This is done in order to obtain the detective quantum efficiency (DQE) according to the international standards

of the International Electrotechnical Commission (IEC 62220-1). These parameters are sufficient to indicate the performance of the detector in terms of the input signal. The STP displays the relationship between the mean pixel values (signal) and the radiation dose. Ideally, the detector should respond linearly to the dose. The NNPS and pMTF describe the noise components and image resolution as a function of spatial frequency, respectively. The ideal radiation detector for radiography should have a limiting resolution between 3 and 5 lp/mm. Theoretically, an optimum radiation detector would have a DQE equal to one at all spatial frequencies.

The MV detector evaluation is divided into two main categories: dosimetric properties and imaging quality. The previous criteria for imaging quality can be followed in order to evaluate the MV detector as an imager. The dosimetric properties are assessed by studying the linearity of the detector mean signal as a function of the radiation dose or dose rate, uniformity, and long and short reproducibility. The expectation of an outstanding MV detector is to respond uniformly and linearly to the dose and dose rate, with a high degree of agreement in both the long- and short- term clinical dose rate. Generally, for conventional linac the dose rate lies from 600 to 1400 MU/min [136].

2.4 Materials and methods

2.4.1 Imaging system devices

In this study, two CMOS sensors, both named Lassena, were evaluated. They are designed by the Rutherford Appleton Laboratory (Oxford, UK). One is for the kV range of X-ray imaging and cone-beam computed tomography (CBCT) applications; the other is for MV usages, including positioning verification and dosimetry. Lassena (kV) will be used to refer to the detector designed for X-ray imaging and cone-beam computed tomography (CBCT) applications. Its construction is shown in Figure 2.1, a. Lassena (MV), the second detector, intended for positioning verification and dosimetry, and its construction, is shown in Figure 2.1, b.

Both Lassena detectors measure 12.0 cm × 14.5 cm, have a resolution of 2800 × 2400 pixels and a pixel pitch of 50 μm. For Lassena (kV) detector evaluation, beam dependence and image quality were measured according to IEC 62220-1 (2003) at UCL X-ray laboratory, with a focal spot of 1 mm and tungsten target [3]. In order to evaluate the image quality of medical electrical equipment, detective quantum efficiency (DQE) was determined [137].

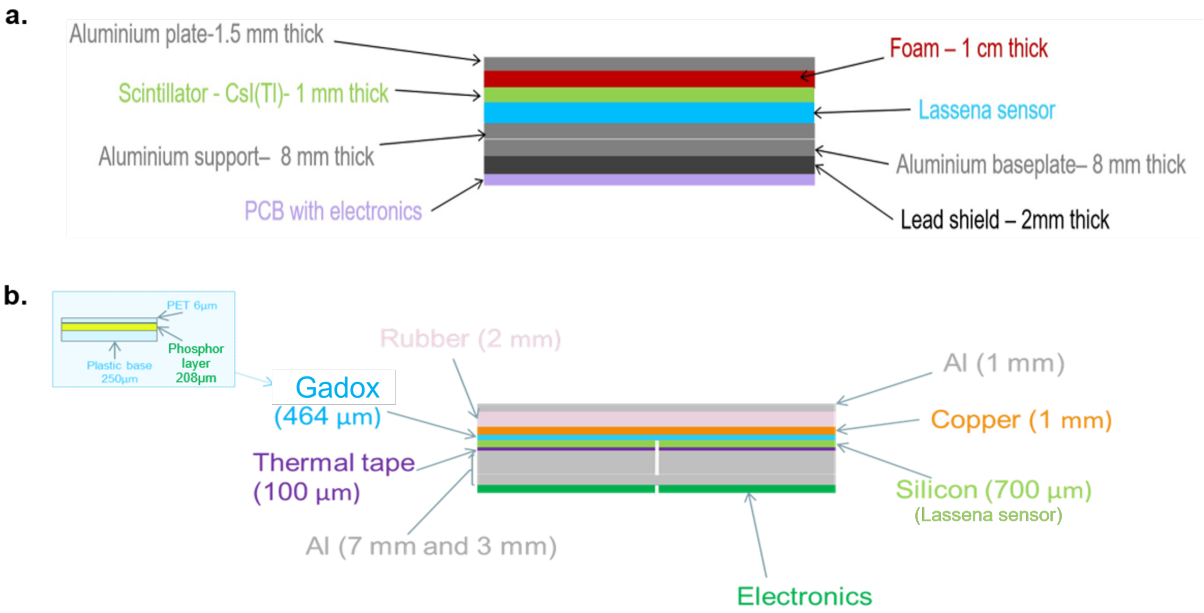

Figure 2.1: A schematic of **a.** Lassena (kV) **b.** Lassena (MV) detectors. PCB: printed circuit board, PET: polyethylene terephthalate (plastic). These drawings are not to scale.

2.4.2 Lassena (kV) detector

2.4.2.1 Experiment setup for Lassena (kV) characterisation

For DQE measurements, the detector was placed 150 cm from the X-ray source, as shown in Figure 2.2. An additional filter was applied for each radiation quality considered in order to obtain uniform exposure onto the detector surface. More specifically, for pre-sampling modulation transfer function measurements, a tungsten plate (known as a test device) was placed directly in front of the detector, as shown in Figure 2.3, b. Further details will be provided in section 2.4.2.6. Two

blocks of lead were used as a diaphragm in order to function as collimators.

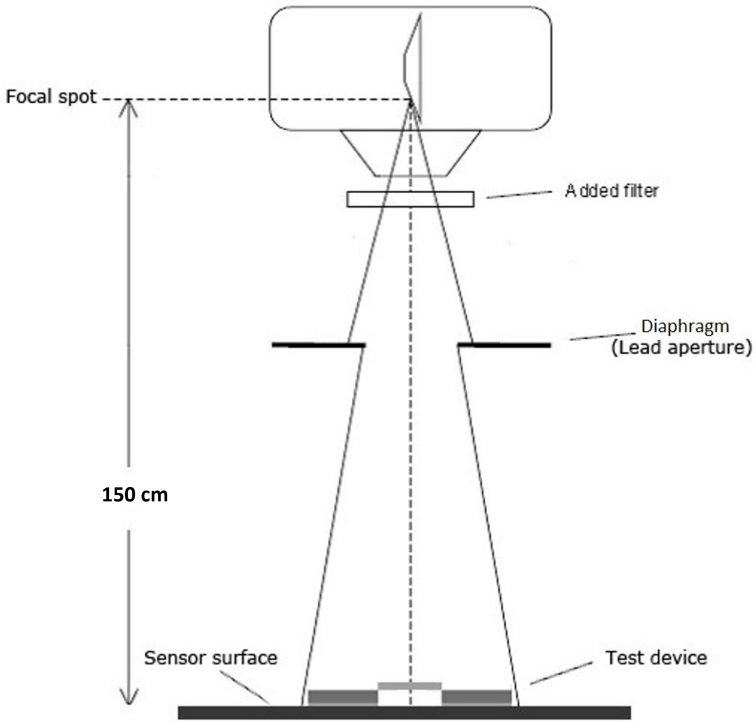

Figure 2.2: Test geometry for DQE as stated in IEC 62220-1 protocol. The additional filter was 10 mm Al, 21 mm Al and 30 mm Al for 54 kV, 74kV and 92 kV respectively. The radiation field was larger than 16 cm × 16 cm [3].

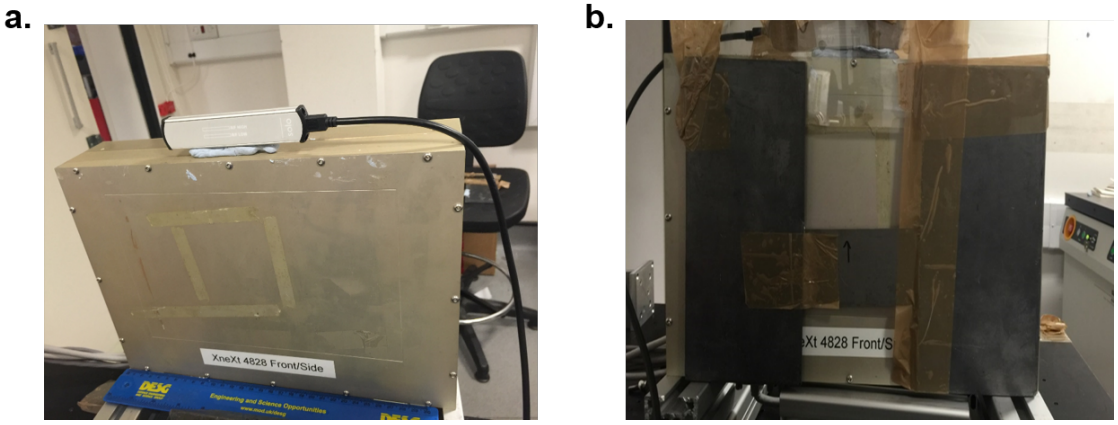

Figure 2.3: Lassena (kV) whilst measuring the K_a values with RaySafe Solo solid state (a) and whilst measuring the pMTF (b).

2.4.2.2 Beam quality

The half value layer (HVL) has been measured to to comply with IEC standard requirements and thus determine the corresponding parameters since every voltage

produces differing radiation quality. According to IEC 62220-1, radiation quality assurance (RQA) 5 is preferred if a sole radiation quality will be used [3]. In this case, in order to achieve a fair evaluation, RQA 3, 5 and 7 were selected since they are the commonly used energies in medical imaging: RQA 3 is usually used for paediatric extremities imaging; RQA 5 for adults extremities radiography; and, RQA 7 since this detector was designed for cone beam CT imaging where high energies are used (above 90-120 kV). For X-ray tube at UCL, 90 kV is the highest voltage that can be reached.

The geometry for these measurements was compliant with IEC 62220-1 standards (see Figure 2.2). In order to obtain the HVL of 4 mm Al, 7.1 mm Al and 9.1 mm Al using the X-ray source in the lab at UCL, it was found that the energies should be 54 kV, 74 kV and 92 kV respectively instead of 50 kV, 70 kV and 90 kV with additional filtration of 10 mm Al, 21 mm Al, 30 mm Al respectively (see Table 2.1).

Table 2.1: The radiation qualities according to IEC 62220-1 [3]

Radiation quality	**Approximate X-ray tube voltage (kV)**	**Additional filtration (mm Al)**
RQA 3	54	10
RQA 5	74	21
RQA 7	92	30

2.4.2.3 Air-Kerma (K_a) at detector surface

The air-kerma was measured for 54 kV, 74 kV, and 92 kV at a range of radiation spectra using RaySafe Solo solid state (Unfors, Billdal, Gothenburg, Sweden). It was placed on the detector (see Figure 2.3, a). The inverse square law was applied in order to correct for a small gap between the top layer and the scintillator. For each source tube current (mA), ten readings were taken after 200 s and then averaged in order to increase the accuracy of the readings.

2.4.2.4 Signal transfer property (STP)

Signal transfer property (STP) describes the relationship between the detector mean pixel value (MPV) and K_a. The ideal response should be linear and without image processing except for the pixel defect calibration and non-uniformity correction [3]. The mean pixel value was studied in addition to the detector's response fit using the linear equation (2.1):

$$MPV = BK_a + A \tag{2.1}$$

Where A and B are offset and the STP gradient of the fit parameters respectively.

2.4.2.5 Normalised noise power spectrum (NNPS) determination

The normalised noise power spectrum (NNPS) is an essential component required in order to measure the DQE. The NNPS determines relative noise properties in the detector response. The same geometry as shown in Figure 2.2 was used, but without the test device. For this measurement, 30 images of dark field were taken (without radiation exposure) at an integration time of 0.13 s via software developed by Lassena designers. Subsequently, another 30 images of bright (light or flood) images were taken at different tube currents (e.g., from 1-8 mA) below the saturation level. A second-order polynomial fit was applied to correct for the beam non-uniformity, such as the heel effect. The NNPS analysis was done according to IEC protocol by dividing an image into a number of squares (called regions of interest (ROIs)), with each measuring 256×256 pixels with an overlapping ratio of 128 pixels. The NPS was acquired as a function of spatial frequency by applying the fast Fourier transform (FFT) using equation (2.2).

$$NPS(u,v) = \frac{\Delta x \Delta y}{M N_x N_y} \sum_{m=1}^{M} \mid FFT\{I_{(}x_i, y_{i)} - S_{(}x_i, y_{i)}\} \mid \tag{2.2}$$

Where u and v are the spatial frequencies reflecting x and y; $\Delta\, x$ and $\Delta\, y$ are pixel pitches in x and y directions; N_x and N_y express the x and y directions of the *ROI*; M is the *ROIs* number that is used in averaging; and, $S(x,y)$ and $I(x,y)$ are the fitted

2D function and corrected flat field image, respectively. FFT is the fast Fourier transform [34]. The *NNPS* is obtained by applying the following equation (2.3):

$$NNPS = \frac{NPS}{(mean\,signal\,value)^2}. \tag{2.3}$$

The coefficient of variation (CoV(%)) was calculated by dividing the standard deviation of the pixel values in the image by the mean pixel value. This metric was utilised in order to easily compare the detector under investigation with other commercially available detectors for CBCT applications. For the MV detector, the NNPS was measured using the same steps mentioned above, but with a different setup which will be discussed in section 2.4.3.1.

2.4.2.6 Pre-sampling modulation transfer function (pMTF) determination

pMTF is another important parameter used to measure the DQE. In this research, it was measured using the edge method recommended by the IEC 62220-1 protocol. The test geometry in Figure 2.2 was used with the test device, and which consisted of a polished edge tungsten plate (50 mm long and 75 mm wide). It was placed at a tilted angle of 2° between two thick lead plates in order to prevent the scattering radiation from the tungsten plate to reach the detector under investigation. The plate is shown in Figure 2.4. This arrangement is recommended by IEC 62220-1 in order to examine the pixels in both row and column directions. This test device should be placed directly in front of the digital detector, and parallel to rows, in order to measure the vertical pMTF, as shown in Figure 2.3, b. When this was done, 30 light images were taken at the highest current for each radiation quality assurance (RQA) level in order to decrease the statistical noise. Subsequently, the test device was rotated 90° clockwise with the aim of measuring the horizontal pMTF. Each half of the detector was treated individually: this meant the horizontal and vertical pMTF for each half were examined separately. Afterwards, the results were averaged for the four pMTF outcomes in order to acquire one averaged figure for pMTF.

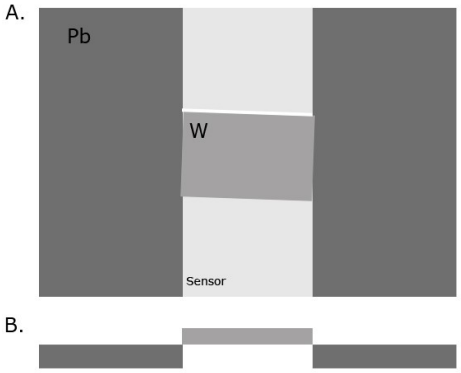

Figure 2.4: The test device used to determine the MTF. Pb is lead plate, W is polished edge tungsten plate. **A.** the device front view **B.** the device lateral profile. As shown, the tungsten is tilted by 2° (IEC 62220-1 recommends 1.5° to 3°). This drawing is not to scale.

2.4.2.7 Detective quantum efficiency (DQE) measurement

After measuring the K_a, NNPS and pMTF, the DQE was calculated using equation (2.4):

$$DQE(f) = (\frac{SNR_{out}}{SNR_{in}})^2 = \frac{pMTF^2(f)}{\frac{\phi}{K_a} K_a NNPS(f)} \tag{2.4}$$

SNR_{out} and SNR_{in} are output and input signal to noise ratio respectively. SNR_{out} refers to the output information of the detector, and SNR_{in} refers to input information carried by the X-ray field impinging onto the detector [138]. The photon fluence (ϕ) was provided by IEC 62220-1 (as shown in Table 2.2), whilst the K_a values were measured at detector surface (as previously explained in section 2.4.2.3).

The calculations of pMTF, NNPS and DQE are presented in spatial frequency from 0.5 lp/mm to Nyquist frequency with 0.5 with an interval of 0.5 as recommended by IEC standard [3]. The zero frequency is excluded because low frequency artifacts causes underestimation of DQE results [34].

Table 2.2: Photon fluence per K_a values according to the IEC 62220-1 standard

RADIATION QUALITY	$\frac{\Phi}{K_a}$ $(1/(mm^2.\mu Gy))$
RQA 3	21759
RQA 5	30174
RQA 7	32362

2.4.2.8 Accumulation of dark current

This indicates the accumulation of dark charge in the pixels as a function of the integration time. Likewise, testing the effectiveness of the dark frame subtraction was involved. The accumulation of dark current was calculated using the following equation (2.5):

$$i_d = \frac{\bar{S}_d K q_e}{A T_{int}} \tag{2.5}$$

Where i_d (A/cm^2) is the dark current ; $\bar{S}_d$ (DN) is the mean dark signal at different integration times; K (e$^-$/DN) is the conversion gain (obtained from the relationship between dark current and integration time (see Figure 2.11)) ; q_e is the electron charge (which is equal to 1.6x10^{-19} Cb); A is the pixel area (cm^2) ; and, T_{int} is the integration time (s).

The accumulation of dark current was evaluated based on the mean pixel value as a function of the integration time. The dark frame subtraction was assessed by subtracting two consecutive images taken at the same integration time.

2.4.3 Lassena (MV) detector

2.4.3.1 Radiation dosimetry and dose-response behaviour

Six MV photon beams were used to test Lassena (MV), as shown in Figure 2.1, b. The main features of this new detector are the scintillator (208 μm thick of gadolinium oxysulfide doped with terbium) and the fine pixel size. The radiation source of 6 MV (linac) was calibrated in order to deliver 1 cGy per monitor unit

(MU) at 100 cm source to surface distance (SSD) and at a depth of d_{max}, which is 1.5 cm for 6 MV, in the water for a field size of 10 cm ×10 cm. The MV detector was placed at the same distance as EPID (160 cm) in order to comply with the clinical requirements. The evaluation method was designed according to several previously published papers in terms of dose-response and radiation dosimetry [139–142]. The images were calibrated using dark-field and flood field images.

- **Linearity based on dose rate**

  For linearity evaluation, the dosimeter was irradiated using the same beam energy and same field size at different doses (MU). Ideally, the detector should respond linearly as a function of dose or dose rate [139–142]. In this case, 100 images were taken at different dose rates (51, 105, 203 MU/min) at 5 MU in order to avoid detector saturation since the detector showed a high degree of sensitivity to radiation. Firstly, the images were corrected using flat field correction and, secondly, the mean pixel value within image ($>$ 5 million pixels) was studied as a function of dose rate.

- **Reproducibility**

  The reproducibility was evaluated throughout a day by determining the mean pixel value for a group of corrected images (i.e., using flat field correction) taken with the same parameters but at a different time during the day [139, 142, 143]. Subsequently, the percentage difference between the first and last images was calculated.

- **Uniformity**

  The pixel uniformity-response across the irradiated field was determined by relating the several points at a different position to point at the centre (P_0) [144]. The mean pixel response was measured over 48 $\times$ 39 pixels for each point. The P_T, P_B, P_R and P_L are points at the top, bottom, right and left of the image, respectively. These points were averaged to represent penumbra ($P_{penumbra}$) (see Figure 2.5).

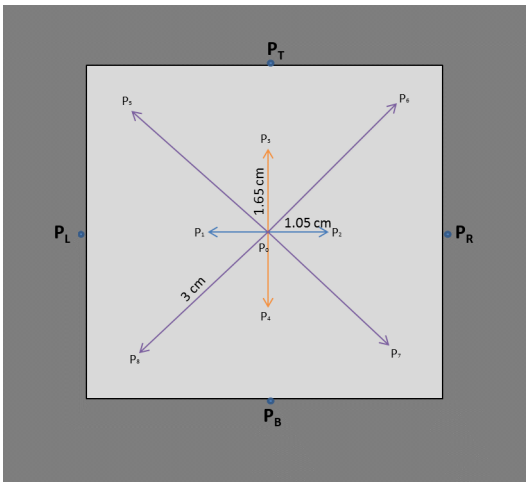

Figure 2.5: Points locations for pixel uniformity-response for 6.4 cm × 6.4 cm at 160 cm. The light grey is the exposed field and the dark grey is the area outside the field.

Flatness and symmetry of the photon beams were calculated for radiation beam quality assessment using the following equations (2.6, 2.7):

$$Flatness = \frac{D_{max} - D_{min}}{D_{max} + D_{min}} \times 100 \tag{2.6}$$

$$Symmetry = \frac{area_{left} - area_{right}}{area_{left} + area_{right}} \times 100 \tag{2.7}$$

Where D_{max} and D_{min} are the maximum and minimum doses and $area_{left}$ and $area_{right}$ are the doses on left and right areas of the dose profile, respectively.

Since this detector might be used for positioning verification and imaging, the NNPS and dark current accumulation were calculated according to parameters outlined in sections 2.4.2.5 and 2.4.2.8, respectively.

2.5 Results and discussions

2.5.1 Lassena (kV) detector

2.5.1.1 Signal transfer property (STP)

Figure 2.6 demonstrates the relationship between the MPV and K_a for all RQAs. It is clear that Lassena (kV) has a linear response within the range of investigated exposures (0.26– 2.17 μGy for RQA3 and 0.29- 1 μGy for RQA 5, 7) with the coefficient of determination (R^2) more than 0.9995 in all cases. The error bars (which express the precision of the measurement) were not included since it was found that the coefficient of variation (CoV) was less than 9% for all beam qualities. Furthermore, in general if the CoV does not exceed 15% for a large sample and 18% for a small sample, the measurements are considered accurate; on the other hand, if the CoV is beyond this limit, the measurements are not precise and therefore must be reassessed [145].

A signal increase was observed as the beam energy increased. As reported by [4, 146–148], one reason for this observation is that the photon fluence per exposure ratio has a direct relationship (i.e., as one increases, the other increases) with the radiation energy. Thus, more X-ray photons are hitting the detector surface as the energy boosts. The other explanation is that the production of the optical light in the scintillator takes place near the sensor surface since radiation energy increases, thereby causing more light to be collected [149].

It is very remarkable that the detector has a considerable degree of sensitivity to radiation compared to other detectors studied by [4–6]. Looking at Figure 2.7, the detector saturates at 2.17 μGy for 54 (RQA3), 1.02 μGy for 74 (RQA5), and 0.93 μGy for 92 kV (RQA7) whereas for the digital X-ray detectors in general radiography, the K_a levels commonly range from 0.8 to 8 μGy [57]. Nevertheless, Lassena (kV) can supply a satisfactory image quality in terms of DQE at low exposures, and this will be discussed in section 2.5.1.4.

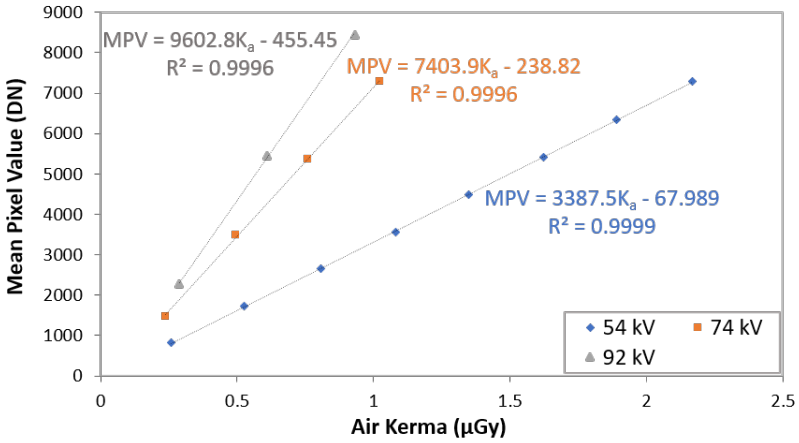

Figure 2.6: The relationship between the MPV and K_a for all three energies.

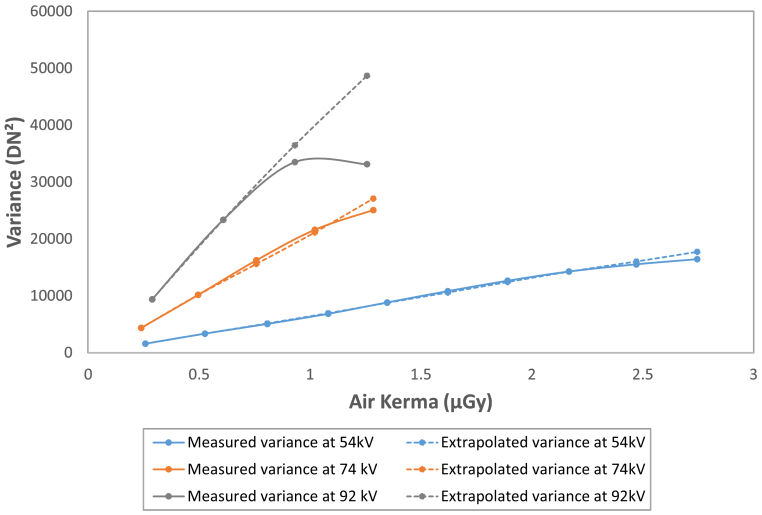

Figure 2.7: The relationship between the variance and K_a for all three energies.

2.5.1.2 Pre-sampling modulation transfer function (pMTF)

It was found that the pMTFs are not dependent on the beam energy for this detector within the investigated range (see Figure 2.8). At low frequencies between 1 and 3 lp/mm, it is worth mentioning that raising the beam energy slightly improved the resolution. This behaviour is attributed to the longer mean free path of the higher energy X-rays leading to a greater number of interactions near the sensor, and as a result limiting the spread of the scintillation photons [4]. The pMTF reaches 50% at 0.9 lp/mm for 54 kV, 1.08 lp/mm for 74 kV and 1.1 lp/mm for 92 kV beam qualities (see Figure 2.8). It is well known that the frequency corresponding to 10%

MTF describes the limiting resolution of a system: to that end, Lassena (kV) has a limiting resolution of 3 lp/mm for all three beam qualities. The adequate limiting resolution for a detector resolution in general radiography ranges between 3 and 5 lp/mm [4, 15].

Lassena (kV) was compared to other available CBCTs on the market, and the outcomes are shown in Table 2.3 [7–11]. The small pixel size allows Lassena (kV) to achieve a better resolution: it records 1.5 and 3 lp/mm at MTF 50% and 10% respectively, whilst others record between 0.28 to 0.55 lp/mm at MTF 50%, and between 0.45 to 0.93 lp/mm at MTF 10%. For radiographic imaging usage comparison, Table 2.4 [4–6, 150] illustrates that Lassena (kV) detector has modest pMTF due to the scintillator thickness. Latterly, this increases the opportunity for light to spread and scatter which will, in turn, lower the overall image quality as the DQE is directly proportional to pMTF [48].

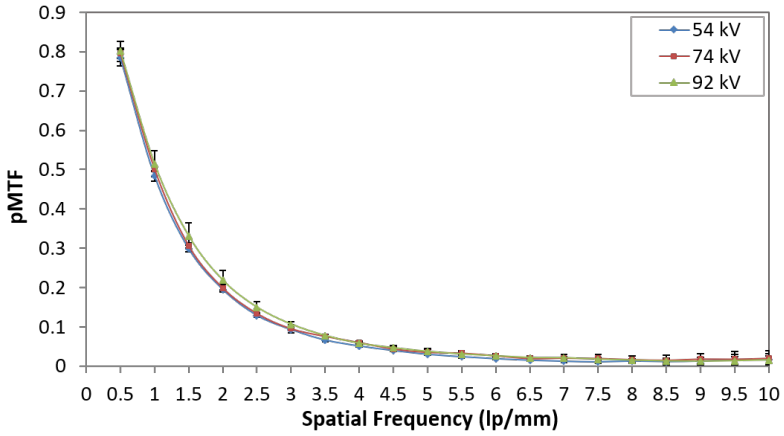

Figure 2.8: The averaged pMTFs for Lassena (kV) at three different energies.

2.5.1.3 Normalised noise power spectrum (NNPS)

The NNPS for the detector under investigation showed that the NNPS reduced as the radiation energy and dose (which is equivalent to K_a value in this case) increased at different beam qualities as shown in graphs a, b and c in Figure 2.9. This reduction in NNPS values is due to the signal intensification given the higher number of photons hitting and interacting with the material within the detector. Therefore, it will result in a higher number of absorbed photons [147, 148]. This outcome implies

that NNPS heavily relies on exposure: consequently, it is anticipated that the DQE values will rise at a higher K_a value because the DQE is inversely proportional with NNPS. As displayed in Table 2.3, Lassena (kV) has a coefficient of variation (CoV) of 0.11% and this is lower than other commercially accessible detectors designed for CBCT applications [7–11].

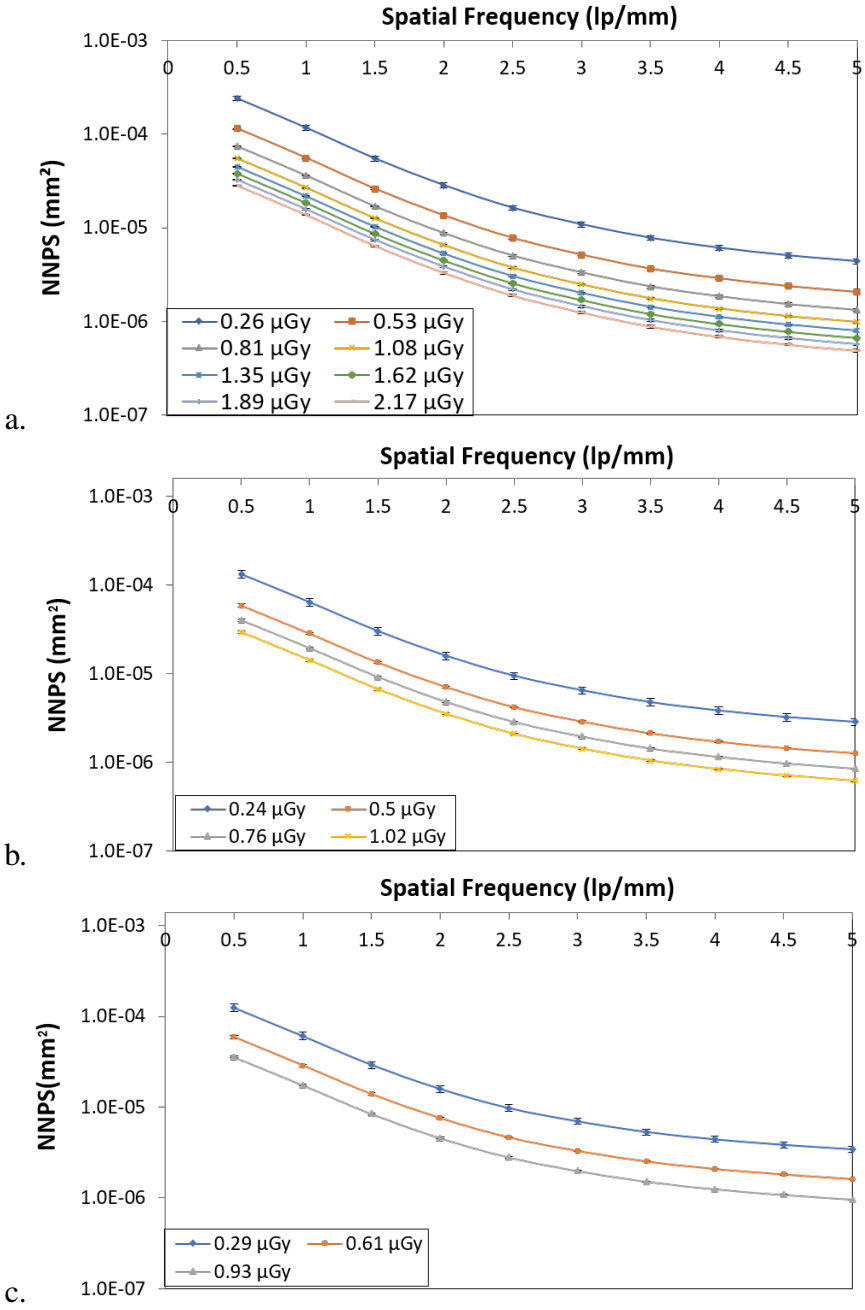

Figure 2.9: 1D NNPS of **a.** RQA3 (54 kV) **b.** RQA5 (74 kV) **c.** RQA7 (92 kV) at different K_a values.

2.5.1.4 Detective quantum efficiency (DQE)

For the three beam energies, it was found that the DQE values decrease as a function of spatial frequency, especially at high frequencies. The DQE noticeably became less reliant on exposure due to the intensification of the photon shot noise and reduction of the pMTF [147, 148]. On the other hand, DQE was enhanced when the radiation current or dose and voltage or energy increased, as shown in Figure 2.10. The DQE values at 0.5 lp/mm (DQE(0.5)) are around 0.46 for RQA3 at all K_a values, and they are 0.52–0.56 for RQA5. Lastly, for RQA7, the DQE (0.5) values are about 0.55–0.59. For RQA3, it can be observed the under investigated imaging system demonstrates a quantum-limited condition: in other words, it is less reliant on exposure at low energies. This could be explained by the residue fixed pattern noise (FPN), or the amplified effect of CMOS APS inherent non-linearity as verified by [34]. Even so, this imaging system displays higher DQE values at higher beam energies [29, 40, 151, 152]. Looking at Table 2.4, Lassena (kV) offers suitable DQE values at low doses as a detector for general radiography usages. The detectors in [5, 6] studies require around 31 and 8 μGy in order to obtain DQE value 0.1 and 0.8 at 0.5 lp/mm for RQA5 (usually around 70 kV), unlike Lassena which requires 0.24 to 1.02 to get a DQE value of 0.52 to 0.56 at 0.5 lp/mm using 74 kV (RQA5). Hence, this makes Lassena applicable for radiography imaging.

Table 2.3: Comparison between Lassena (kV) and other available detectors that can be used for CBCT in radiotherapy departments [7–11]

	Varian	**Elekta**	**Siemens**	**Lassena (kV)**
Resolution (Pixels)	2048 × 1536	1024 × 1024	1024 × 1024	2786 × 2400
Physical size (cm^2)	39.73 × 29.8	41 × 41	41 × 41	24 × 14.4
Image depth (bit)	16	16	12/16	14
Pixel pitch (μm)	388	500	400	50
Max frame rate (fps)	30	5.5	25	30
Tube voltage	30-140 kV	70-150 kV	6 MV	54-92 kV
MTF 50%/10% (lp/mm)	0.548/0.939	0.28/0.45	0.3/0.5	1.5/3
Coefficient of variation (%)	0.7	1.4	2.7	0.11*

*Obtained at the energy of 92 kV and K_a value of 0.93 μGy.

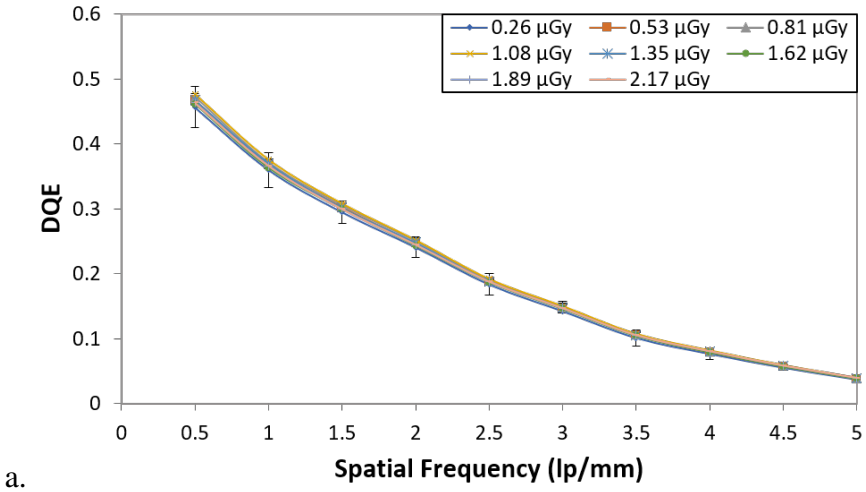

a.

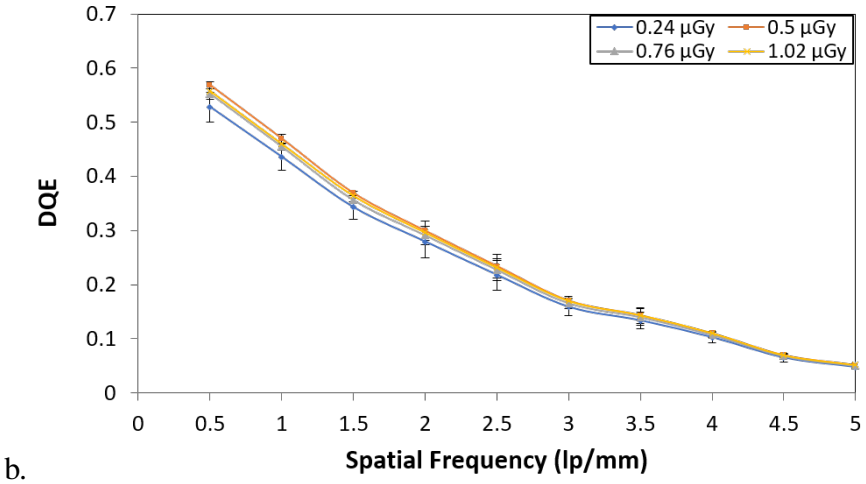

b.

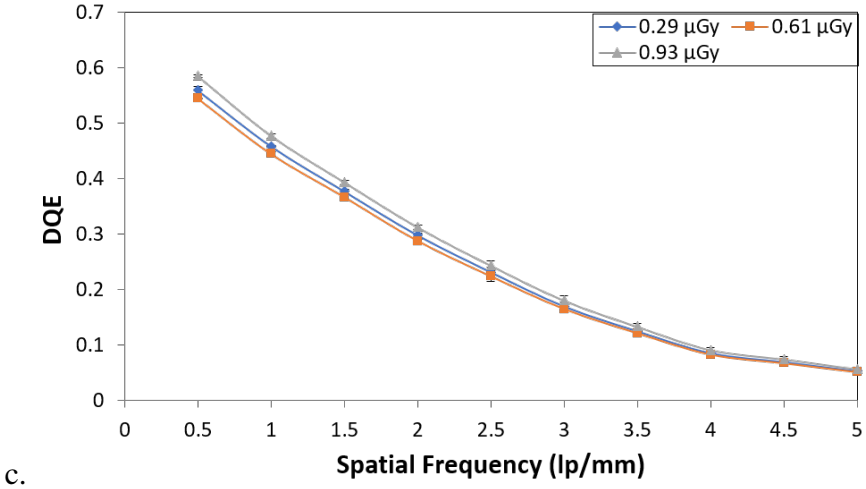

c.

Figure 2.10: DQE of **a.** RQA3 (54 kV) **b.** RQA5 (74 kV) **c.** RQA7 (92 kV) at different K_a values.

Table 2.4: List of Studies that evaluated a new detector and the main findings compared to Lassena (kV) [4–6, 150]

		Konstantinidis et al. [4, 150]	Michail et al. (2015) [5]	Michail et al. (2016) [6]	Lassena (kV)
Resolution (Pixels)		3888 × 3072	1200 × 1600	1200 × 1600	2786 × 2400
Physical size (cm²)		29 × 23	-	-	24 × 14.4
Image depth (bit)		14	-	-	14
Pixel pitch (μm)		74.8	22.5	22.5	50
Max. frame rate (fps)		26	-	-	30
Scintillator material		CsI(Tl)	CsI(Tl)	CsI(Tl)	CsI(Tl)
Scintillator thickness (µm)		200	170	490	1000
MTF 50%/10% (lp/mm)		1.2/4.5	3.6/9.6	1.9/5.8	1.5/3
DQE at 0.5 lp/mm	RQA3	0.53-0.68	-	-	0.45-0.47
	Range of dose (μGy)	0.14-3.09	-	-	0.26-2.17
	RQA5	0.68-0.75	0.1	0.8	0.52- 0.56
	Range of dose (μGy)	0.13-6.45	31.05	8.39	0.24-1.02

2.5.1.5 Accumulation of dark current

The accumulation of dark current was determined in order to determine the optimal integration time for this experiment. It was computed according to equation (2.5), and is calculated as 2.51 pA/cm^2 with a standard deviation of 0.07 pA/cm^2 for a system with 50 μm pixel pitch. Correspondingly, the imaging system collects 391.3 e^-/s in the illuminations absence. In Lassena (kV)'s case, it scored 12798 e^- at 0.04 s and 14074 e^- at 3.3 s (see Figure 2.11). Accordingly, the integration time was selected at 0.13 s for the current study [29, 147].

Furthermore, the effectiveness of the fixed-pattern noise correction using dark signal noise (DSN) subtraction was assessed. It was found that the correction removed 99.7% of the dark fixed-pattern noise, as expected [6]. The mean noise dropped from 2053 DN with standard deviation of 849.5 DN to 4.3 DN, with standard deviation of 6.6 DN after the correction at the selected integration time (0.13

s) (see Figures 2.12 and 2.13). Hence, this demonstrates the effectiveness of the DNS subtraction for fixed-pattern noise correction and means that signal to noise ratio (SNR) is limited only by the shot noise (which is nonetheless required for a fair comparative analysis) [153].

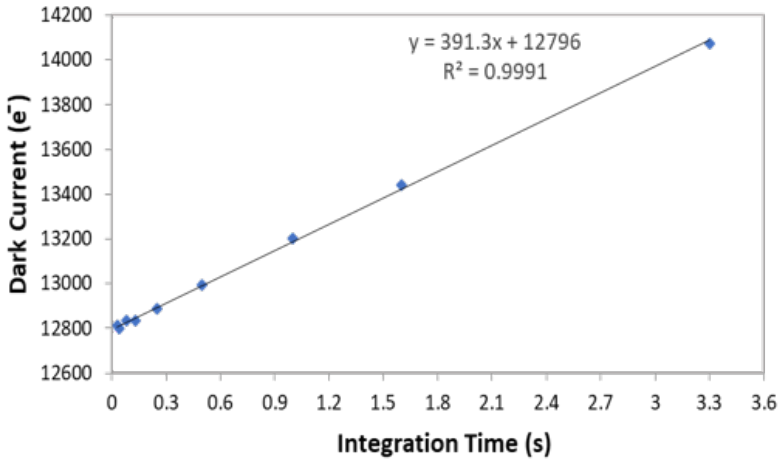

Figure 2.11: The relationship between the integration time and the dark current in the absence of illumination.

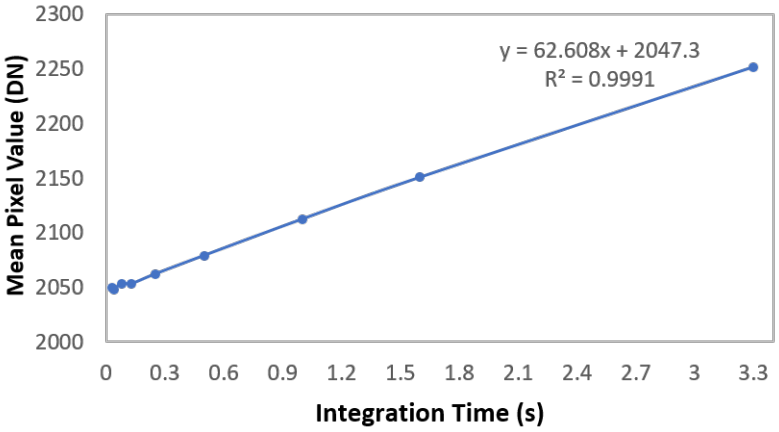

Figure 2.12: The relationship between the integration time and the MPV in the absence of illumination before applying FPN correction. The standard deviation is 849.5 DN.

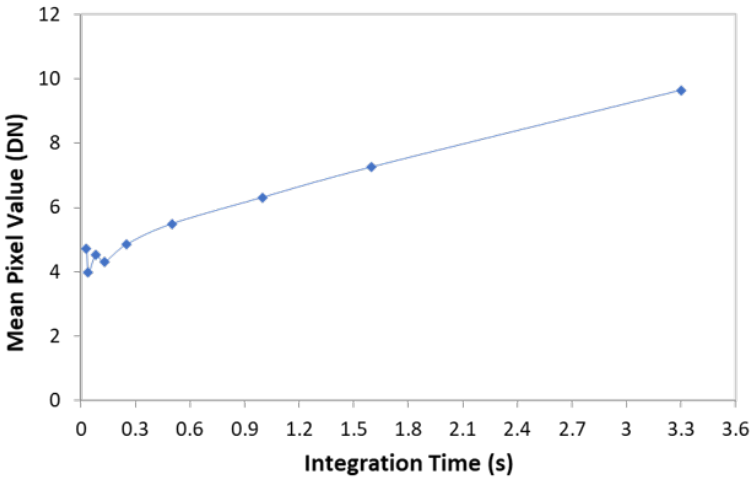

Figure 2.13: The difference of two subsequent DNS images as a function of exposure time after applying FPN correction. The standard deviation is 6.6 DN.

2.5.2 The impact of the scintillator and the sensor on Lassena (kV) dynamic range

The performance of this detector system should be considered in terms of the scintillator (Cesium Iodide activated with Thallium (CsI(Tl)) and the sensor (Lassena) since there are additional factors related to the design which might degrade the image quality. Lassena CMOS sensor has 40 e^- root mean square (rms) noise according to a measurement by the detectors' designers, whilst ubiquitous amorphous silicon (a-Si(H)) detectors have typical noise values of 800-1000 e^- rms [154]. The Rose criterion states a resolvable signal needs to be five times the noise level in order to be resolved [155]. For Lassena, which has a quantum efficiency of 50%, a point source would need to emit 400 optical photons to be resolved, whilst an a-Si(H) detector would need 8000 optical photons. Hence, Lassena requires less photons and consequently less radiation dose in contrast to the a-Si(H) detector. This low noise performance comes at the cost of dynamic range: Lassena has a full well capacity of 112,000 e^-, and a bright scintillator such as CsI(Tl) will result in Lassena saturating quickly. The dynamic range of Lassena could be significantly increased by using a shorter integration time, or using a dimmer scintillator. However, if the absorption remains the same the noise at a lower flux will increase. Ideally, a scintillator with

higher absorption and a lower light yield would be preferred. Given that low noise digital sensors such as Lassena are relatively new to the market, no such sensor is available in a suitable form for imaging.

The calculation of how signal and associated noise propagate through each stage of the entire imaging system is known as quantum accounting, and this allows regions which limit the DQE to be identified [156]. This approach has shown the benefit of increased X-ray absorption in improving DQE. Traditionally the signal transfer stages that limit the DQE (also known as the quantum sinks) have typically been in the collection of the optical light from the scintillator. In other scintillator based detector systems, the quantum sink associated with the collection of scintillation light has been a result of the poor efficiency of lens-based systems, or the high noise of the image sensors. Considering the low noise observed in Lassena performance trials, the X-ray absorption of the scintillator is the most significant factor in obstructing sensor performance. More specifically, a high gain optical stage (i.e., bright scintillator) is responsible for the limited dynamic range of this system.

2.5.3 Lassena (MV) detector

In this study, several measurements have been performed in order to initially assess the design of Lassena (MV) detector. Specifically, these have been in terms of: linearity; uniformity; reproducibility; dark noise; and, NNPS since this MV detector is designed for radiotherapy applications. These can include the positioning of patient and dose verification using the imaging and dosimetric properties of the detector.

The main difference between Lassena (kV) and (MV) is that the scintillator (see Figure 2.1) for Lassena (kV) is made of CsI (Tl), which is commonly used in X-ray imaging detectors alongside gadolinium oxysulfide doped with terbium. This is also known as Gadox. Both materials have wide conversion gains, and their emission wavelength peaks are in the green part of the visible spectrum at 550 nm and 545 nm for CsI(Tl) and Gadox, respectively. This means that their peaks match the peak quantum efficiency of silicon-based sensors thereby leading

to a high signal collection [157]. CsI(Tl) can, however, be grown to obtain a micro-columnar structure resulting in less lateral spread of the scintillation light, and hence better spatial resolution than other phosphor screens. Thus, CsI (Tl) is preferable in radiation imaging in the kV range [157]. Gadox was used in Lassena (MV) since it is cheaper and also because the designers at RAL state that image quality is poor in MV images regardless of whether the scintillator is CsI or Gadox due to the predominance of Compton scattering (which takes place at MV energies). This interaction does not rely upon atomic number, unlike photoelectric methods which are predominant in kV energies and are responsible for image contrast [61].

All the measurements for MV detector testing were done at the Royal Berkshire Hospital (RBH) in Reading using a 6 MV Elekta linac (Elekta, Crawley, UK). There were only 12 hrs (i.e., one day during working hours) to use the linac. The following measurements have been examined for only one field size: 4 cm $\times$ 4 cm at 100 cm which will, in turn, be 6.4 cm $\times$ 6.4 cm at 160 cm in order to be within the detector boarders. The images were taken at 0.03 s with 30 frames per second (fps) in order to avoid saturation.

- **Linearity:**

  The response of Lassena (MV) detector was assessed as a function of dose rate. These preliminary results showed that the detector is very sensitive to radiation, and that it saturates very quickly. For this reason, the linearity was evaluated at the following dose rates: 51, 105, and 203 MU/min using 5 MU. The coefficient of determination (R^2) was 0.8624, as shown in Figure 2.14. The standard deviation was 1186.48 DN. The detector has a limited dynamic range, and it saturated at 5 MU with a dose rate of 203 MU/min. Despite this, the clinical dose rates for conventional linac range from 600 to 1400 MU/min [136]. This is in order to ensure sufficient lethal damage to cancer cells whilst simultaneously sparing the normal ones. Furthermore, linac is more likely to terminate before delivering the complete dose at low dose rates, as has been reported by [158]. The maximum pixel value was 14710.06 DN, although the

expected maximum pixel value is 16384 DN. On the other hand, the clinical EPID responds linearly at the clinical dose rates, as reported in many studies undertaken by [139, 140, 142].

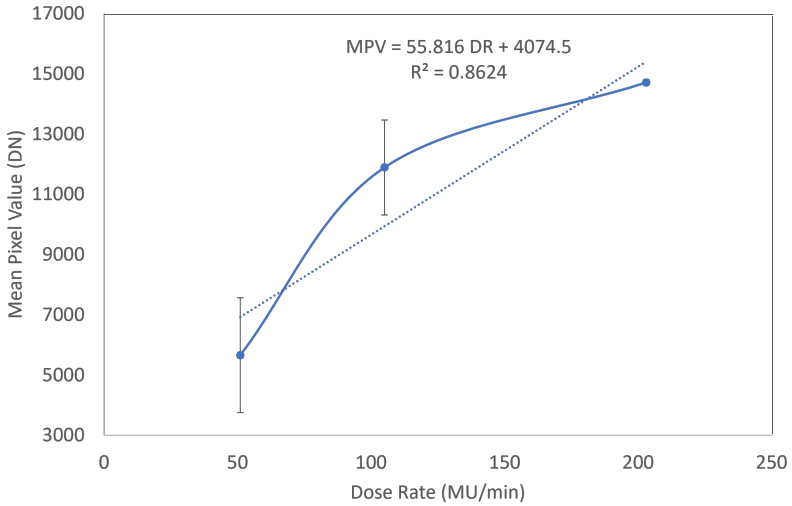

Figure 2.14: Lassena (MV) response as a function of the dose rate. The standard deviation for 200 MU/min is $<$ 85 DN. DR is dose rate.

- **Uniformity:**

  Another important aspect for the assessment is uniformity-response. For uniformity, a measurement 4 cm $\times$ 4 cm field exposed to 5 MU at 51 and 105 MU/min was used. It was challenging to examine the uniformity since the detector was not synchronised with the beam due to the hospital regulations which forced us to synchronise both pieces of equipment manually by operating the detector and the beam simultaneously. This resulted in non-uniform image generation along the x axis because the linac beam is generated and then delivered in pulses of a duration at a given repetition frequency, as is clearly seen in Figure 2.15, a. Each time the pulse will be in different location. With the goal of enhancing the uniformity, 200 images were averaged in order to enhance the (deliberately aggregated) uniformity (see Figure 2.15, b). In summary, the detector responded uniformly within the exposed field with a standard deviation of ±0.012 and ±0.004 for 51 and 105 MU/min respectively. These results are summarised in Table 2.5.

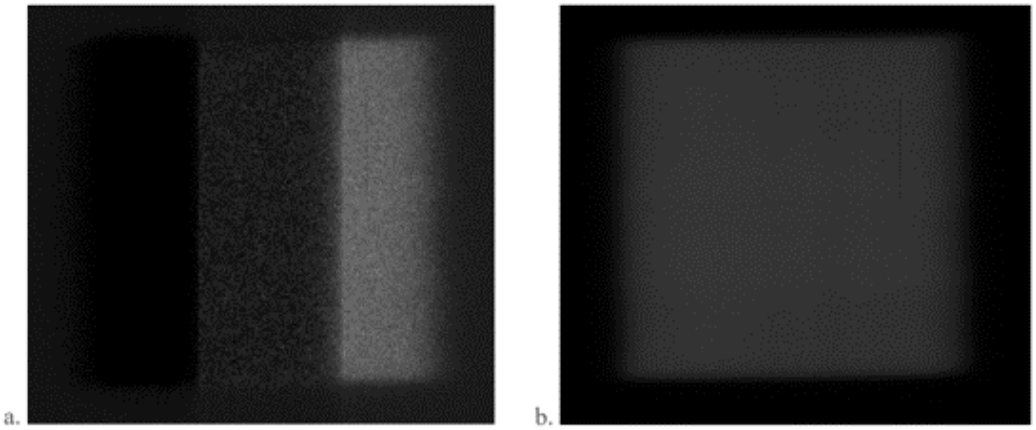

Figure 2.15: An image of bright field showing the non-uniformity along the x axis (a) and an averaged image (corrected) (b).

Table 2.5: The normalised detector response at different points and at penumbra region ($P_{penumbra}$)

	P_0	P_1	P_2	P_3	P_4	P_5	P_6	P_7	P_8	$P_{penumbra}$
51 MU/min	1	0.99	0.988	0.97	0.97	0.99	1.005	0.97	1.006	0.72
105 MU/min	1	1.002	0.99	1	1.002	1.007	1.005	1.007	1.008	0.95

The flatness and symmetry of the used beam were calculated using equations (2.6 and 2.7) and Lassena (MV) detector in order to test beam uniformity. This is because the radiation beam at these dose rates is not stable: consequently, this may cause incorrect evaluation for the radiation detector performance in terms of uniformity. Standard specifications of linac mostly demand that beam flatness be less than 3% when it is measured in a water phantom at 100 cm SSD and 10 cm depth for the largest field size available, and which is 40 cm $\times$ 40 cm in many cases [66]. Typically, symmetry specification is that for any two areas or points of the dose, equidistant from the point of central axis, on a beam profile must be within 2% of each other. A figure greater than 2% indicates that the beam is not symmetrical [66]. The results in Table 2.6 demonstrated that the beam itself it is not flat, but rather symmetrical at 51 MU/min which is to be expected since linac is not stable at low dose rates, but became more stable at 105 MU/min where the beam was both flat

and symmetrical. This explains the higher standard deviations of uniformity which were observed in the test of the detector at 51 MU/min compared to 105 MU/min. The standard deviations were ± 0.012 and ± 0.004 for P_0 to P_8 (within the irradiated field); and, ± 0.09 and ± 0.02 for P_0 to $P_{penumbra}$ (within the irradiated field and the penumbra region) for 51 and 105 MU/min, respectively.

Table 2.6: The flatness and symmetry measurements for the used 6 MV beam

	Flatness (%)		Symmetry (%)	
	Y direction	X direction	Y direction	X direction
51 MU/min	11.02	8.78	-0.53	0.28
105 MU/min	2.96	3.80	-0.30	-0.38

- **Reproducibility:**

  Whilst the accuracy of dose verification remains limited by detector stability, it is essential to assess the detector reproducibility. In this instance, the short-term reproducibility only was assessed, and the detector demonstrates a high degree of short-term stability at a high dose rate, as is shown in Figure 2.16. The percentage difference between the first and the last frames is 6.2% at 51 MU/min, and it is 4.3% at 105 MU/min. The percentage difference at 105 MU/min is lower since the radiation beam is more uniform and stable at a higher dose rate as is shown in Table 2.6 [158, 159]. The mean and standard deviation (STD) appear in Table 2.7: these represent the average value in the 40 frames and the spread of the data from the mean value, respectively. Given that it is relative response, the reproducibility of this detector increases as the mean is equal or close to a value of one, and the STD should be equal or close to zero. Consequently, Lassena (MV) has a higher reproducibility at high dose rate. Similarly, EPID has both long- and short-term stability [139, 142, 143].

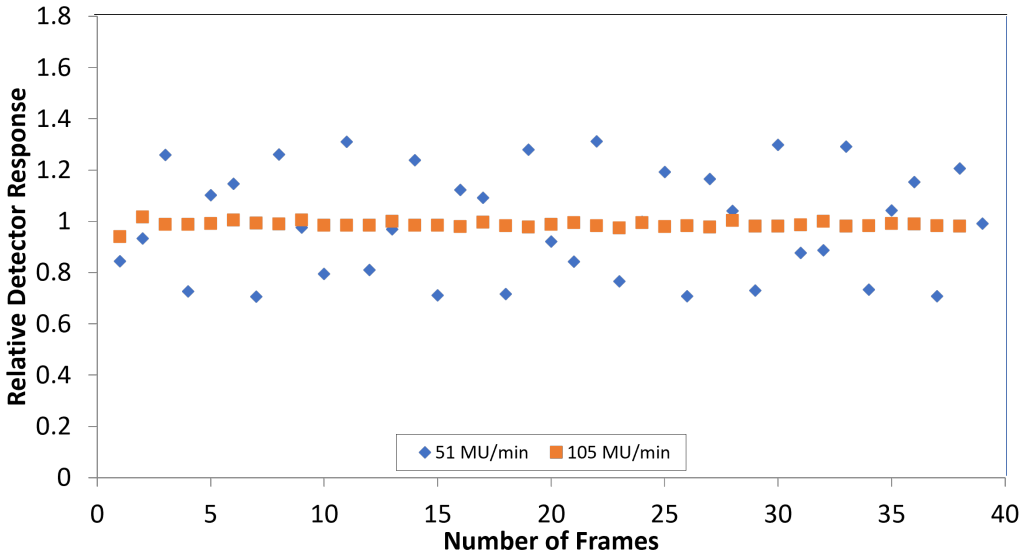

Figure 2.16: The short-term stability of 40 consecutive frames for Lassena (MV) at two dose rates.

Table 2.7: The mean and STD of Lassena (MV) short-term reproducibility for 40 frames

	51 MU/min	**105 MU/min**
Mean	1.17	1.05
STD	$\pm$ 0.25	$\pm$ 0.02

- **Dark current accumulation:**

  For this experiment, the integration time of 0.03 s was used in to avoid detector saturation and to eliminate the accumulation of dark current. It is preferable that the dark current be near zero since it contributes to image noise, is constant, and can be easily removed by FPN correction [160]. Using the equation (2.5), the dark current is 1.36 pA/cm^2 which is equivalent to 212.84 e^-/s for 50 μm pixel (Figure 2.17). It is noticeable that the higher integration time will result in a higher accumulation of dark current, as has been explained by [147]. The dependence of the mean pixel values of the dark images on the integration time is linear, from 0.04 s to 2 s, as Figure 2.18 illustrates. The mean noise is 1547.23 DN, and the standard deviation is 1417.16 DN. Looking at Figure 2.17, the dark current is higher at the start (at 0.04 s) and this could be due to afterglow which is delayed luminescence from the scintillator happening after the irradiation has stopped [161].

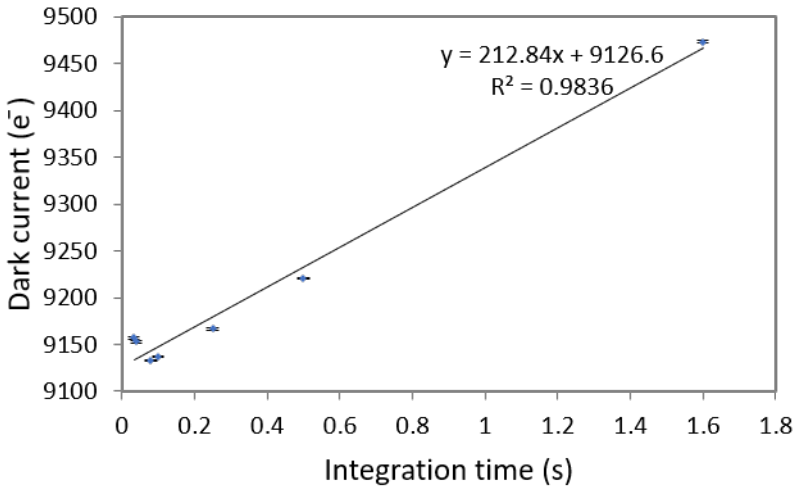

Figure 2.17: The dependence of the dark current on the integration time.

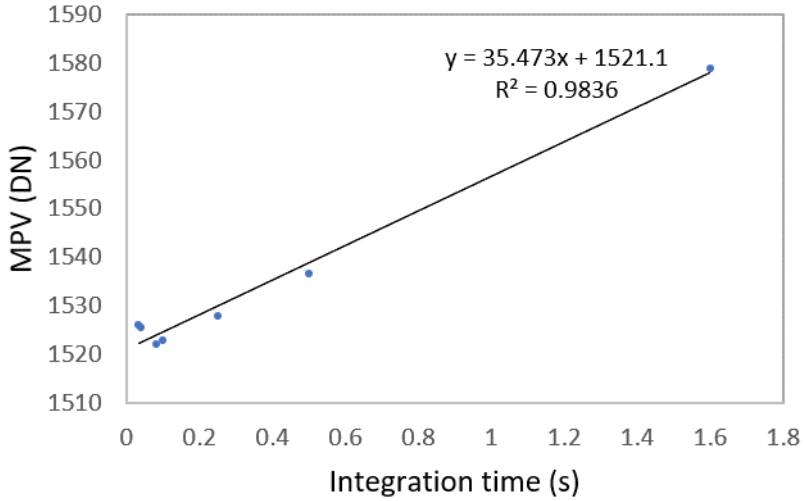

Figure 2.18: The dependence of the MPV on the integration time. The standard deviation is 1417.16 DN.

- **Normalised Noise Power Spectrum (NNPS):**

  The imaging quality assessment is required for detectors used in position verification situations. Figure 2.19 demonstrates the preliminary results of the normalised noise power spectrum for two different dose rates. It is clearly seen the noise decreased at 105 MU/min by almost 70%: this was due to a high signal to noise ratio at the high dose rate. Compared to the noise in Lassena (kV) (see Figure 2.9), the noise in Lassena (MV) is higher: this can be explained by the increased incidence of Compton scattering in the MV

range [13]. However, the pMTF should be quantified in order to get the detector DQE.

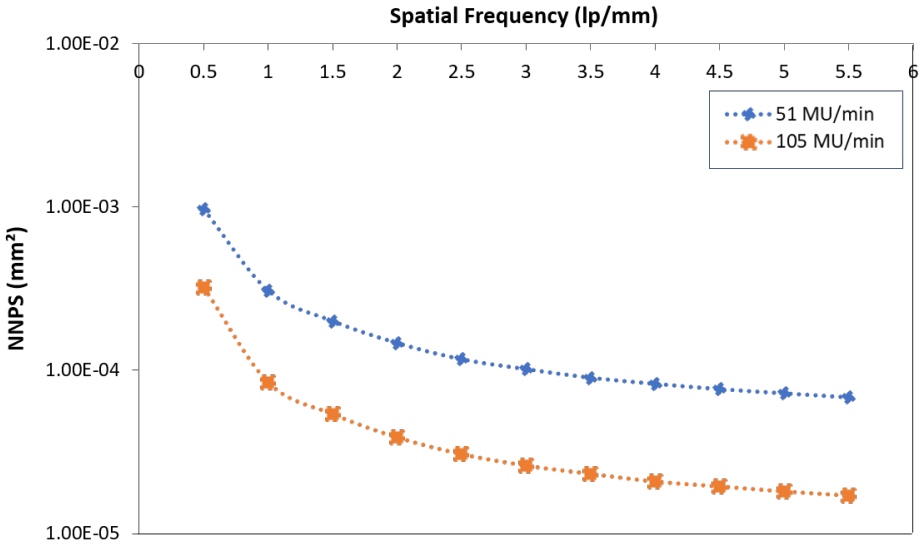

Figure 2.19: 1D NNPS at different dose rates for Lassena (MV).

Based on these results, Lassena (MV) is not yet suitable as a clinical device since the detector becomes saturated after 105 MU/min, which in turn results in a limited dynamic range for the detector whilst the clinical dose rate is between 600 to 1400 MU/min [136]. These results might be due to the sensor (Lassena) as discussed in section 2.5.2 or the scintillator thickness: more specifically, the thick scintillator will guarantee a large production of optical light. Therefore, it is highly recommended to use a thinner scintillator or thicker build up layer. Following this, the modified detector must go under new testing in order to verify whether or not acceptable results have been achieved within the necessary parameters.

2.6 Conclusions

Lassena (kV) detector is designed to be used for imaging in general radiography and cone beam CT applications. This project aimed to characterise the performance of Lassena (kV) detector, at three beam energies with different tube currents (doses), in order to measure the detective quantum efficiency. The DQE values were determined at diverse radiation qualities as recommended by IEC standards. Normally, RQA3 is used for paediatric extremities, RQA5 for extremities of adults, and RQA7 is for cone beam CT imaging where the high energy (usually above 90 kV) are used. The relationship between the mean pixel values and the air-kerma displayed a linear correlation, however, this detector has a very high radiation susceptibility which therefore limited its dynamic range. The spatial resolution and NNPS results led to acceptable DQEs at all energies. DQE (0.5) values were 0.46 for RQA3, 0.52–0.56 for RQA5, and 0.55–0.59 for RQA7 at an integration time of 0.13s. Examining the DQE curves, it can be seen that the detector under investigation demonstrates better performance at high energies (above 70 kV). For CBCT applications, Lassena (kV) showed very promising results, and the development of new scintillators in order to take advantage of low noise sensors (i.e., such as Lassena (kV)), could drastically improve the performance of imaging systems based on this type of sensor.

For Lassena (MV), the dosimetric properties and image noise were investigated with the purpose of evaluating Lassena (MV) detector by means of high energy beams in the MV range as produced by linac. In conclusion, it is worth mentioning that the detector under investigation has a high degree of short-term reproducibility, with an STD of $\pm$ 0.25 and $\pm$ 0.02 for 51 and 105 MU/min. It also has an acceptable pixel uniformity-response at high dose rates with an STD of $\pm$ 0.012 and $\pm$ 0.004 for 51 and 105 MU/min, respectively. There is also decent linearity with a coefficient of determination (R^2) at 0.8624. However, this device showed high susceptibility to radiation which presently prohibits its clinical use given that it saturates at 203 MU/min whilst the clinical dose rates range from 600 to 1400 MU/min. In terms of image quality, the NNPS was measured, however, the pMTF is required

to determine the DQE of the detector. Overall, based on these preliminary measurements, the detector cannot presently be used as an imager nor dosimeter since it needs some modifications to make it clinically viable. These would include the use of a thinner scintillator, or a thicker build up layer in order to increase the dynamic range. This detector may address unmet clinical needs if it can be used routinely as EPID for dose and position verification, in light of the fact that fine pixel size that may lead to superior resolution.

In the summary, the DQE values for Lassena (kV) supports the hypothesis which says this detector can be used for general X-ray imaging and cone-beam computed tomography (CBCT) applications. However, the results for Lassena (MV) disproves the claim that the scintillator within the MV detector has been modified and optimised in term of thickness in order to gain sufficient presentation as an imager. The scintillator thickness did, in fact, result in a rapid saturation. There is insufficient evidence to reject the claim that Lassena (MV) can act as a dosimeter since the detector displayed a high sensitivity to radiation which, in turn, limited the evaluation thereof.

Chapter 3

MC system: building, execution and calibration

3.1 Overview of chapter

This work is a preliminary step for the following two chapters. A radiation source is an essential requirement in order to mimic real case scenarios, but also to calculate the dose in EPID in order to evaluate its performance for error detection applications. In this chapter, the MC system of a linear accelerator was built and validated against measurements using a 1%/1mm and 2%/2mm gamma criteria. The accurate model records less discrepancy against measurements.

The outcomes of this work resulted in the following:

- **Alzahrani, H.**, Royle, G., Ricketts, K. (2019). Monte Carlo Modelling and Calibration of Radiotherapy X-ray Beams. In 2019, UCL Computational Sciences Symposium. Poster presented.

3.2 Hypothesis of chapter

The radiation beam can be simulated and replicated via MC software (BEAMnrc (EGSnrc user code)) to conduct computational trials, thereby mimicking the clinical

experiments. This comes from the fact that BEAMnrc is an accurate tool for linear accelerator constructing.

3.3 Criteria of success

The percentage depth dose (PDD) curve and lateral dose profile are frequently used to assess Monte Carlo (MC) modelling of a radiation beam. The PDD relates the deposited absorbed dose by a radiation beam into a medium, specifically to the depth along the axis of the beam. Likewise, the dose profile describes the absorbed dose in the medium in the x (cross-plane) or y (in-plane) directions, perpendicular to the radiation beam. The linear accelerator (linac) built by BEAMnrc component modules is benchmarked to the measurement data of an actual linac. The percentage dose difference and gamma analysis are the common evaluation tool utilised in order to quantify the accuracy of the simulated system to the actual system. The precise MC system should record a dose difference within $\pm$ 5% for both evaluation tools given that the area ($\geq$ 95%) will contain the true parameter value or acceptable parameter value for safe treatment. This is discussed in more detail in section 3.4.5. In order to obtain high precision in modelling, the linac specifications must correspond to the actual linac.

3.4 Materials and methods

3.4.1 Monte Carlo simulation for linac modelling

In this study, a photon beam was simulated by the means of International Atomic Energy Agency (IAEA) compliant phase space files (PSFs) for 6 and 10 MV, which are available at myvarian account at [162]. These files were specified for components of the TrueBeam Varian accelerator head and scored above the jaws. The files were used as a radiation source for the linac which has been compiled and built using the EGSnrc software, specifically the BEAMnrc user code (National Research Council of Canada, Ottawa, Canada). The input file (see appendix A), with an ex-

tension of .egsinp, was written and defined each component according to available dimensions online (since Varian was not willing to share their linac parameters). The linac consisted of an ion chamber, mirror, and jaw in both x and y directions (see Figure 3.1 and Table 3.1).

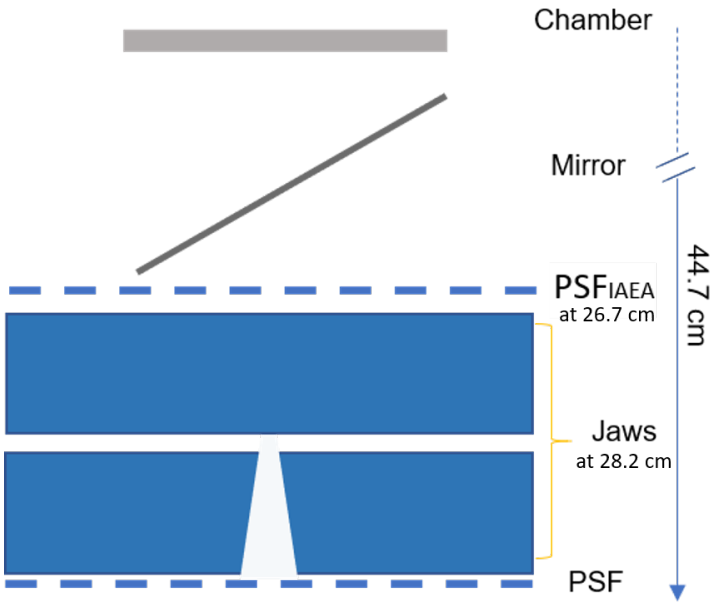

Figure 3.1: MC Linac structure.

Table 3.1: The linac components and the materials of each one

Component modules (CM) as named in the manual	**Composition and material density**	**CM role in the simulation**
CHAMBER	The central region: air- 1.20 $\times 10^{-3} g/cm^3$	Acting as ion chamber
MIRROR	Mylar- 1.38 g/cm^3	A model of mirror
JAWS	Lead- 11.34 g/cm^3	Representing the secondary collimators

The jaws were defined to form field sizes of 10 cm $\times$ 10 cm and 15 cm $\times$ 15 cm for 6 MV, and 10 cm $\times$ 10 cm and 20 cm $\times$ 20 cm for 10 MV at a 100 cm source-axis distance (SAD) with a 95 cm source to surface distance (SSD). This was done in order to comply with the required measurement data. In my case, the

PSF_{IAEA} used was scored above the jaws it was indicated in the PSF headers (i.e., files that come with PSF_{IAEA}). It was scored at 26.7 cm where the jaws in my model start at 28.2 cm. Thus, another PSF was scored underneath the jaws at 44.7 cm for the following step of the dose calculation.

The BEAMnrc has 15 source options, and because the IAEA phase space files were used for this study, source number 21 was chosen. This option permits the user to define the phase space file as the incident source on any component module. The surrounding medium of the linac was air. The charge of the incident particles included photons, electrons and positrons. All these parameters were selected carefully to comply with the actual situation.

Some variance reduction techniques were used to increase the number of particles and furthermore to accelerate the simulation. The energy cut-offs were turned on for electron and photon transports. Based on the literature, the electron cut-off energy was 0.7 MeV and the photon energy cut-off was 0.01 MeV. No range rejection was used in the simulation as there are a limited number of particles in the IAEA files. The bremsstrahlung splitting was applied uniformly with splitting factor of 20, without Russian Roulette [79]. The photon forcing was not activated given that it is less helpful in linac modelling. Please refer to section (1.4.2.2) in chapter 1 for more details on each technique.

The simulation used 3×10^9 histories to achieve an uncertainty lower than 1% and to maintain the calculation efficiency; the simulation was accelerated by running it in parallel jobs. For my computer, the optimum number of parallel jobs without being in the swap mode was 15. The default settings were used for the EGSnrc simulation as they are recommended by EGSnrc expert users in the EGSnrc manual [75]. These setups were applied for both beams 6 and 10 MV. The BEAMnrc gives various possibilities for dose computing: it either calculates the total dose only, or the dose deposited at each linac component. For this project, the total dose was considered.

The details of the virtual linac configuration can be found in the appendix A.

3.4.2 Monte Carlo simulation for dose calculation

The virtual linac was assessed and calibrated using the measured data, received from Royal Free Hospital. This data is discussed in more detail in section 3.4.4. For the PDD and lateral profiles at various depth, the dose calculation for the virtual linac was performed in DOSXYZnrc on a water block phantom. This phantom was defined manually using an option called non-CT phantom in the EGSnrc software. Overall, the water tank dimensions were 30 cm $\times$ 30 cm $\times$ 30 cm with a voxel size of 0.4 cm $\times$ 0.4 cm $\times$ 0.4 cm placed at a distance of 95 cm from the radiation source in order to mimic the measurement setup (see Figure 3.2). The voxel size was selected so as to balance between the statistical uncertainty and resolution since the smaller voxel size in this instance will result in a better image resolution, but also a higher statistical uncertainty due to the limited number of scored photons and vice versa. Additionally, it should be noted that a smaller voxel size requires a longer simulation time [163]. The user must balance between these parameters based upon need on a case-by-case basis. The water tank was voxelised in x, y and z directions in order to easily extract the PDD and lateral profiles data. The phantom material was water surrounded by air. The global electron cut-off energy (ECUT) and global photon cut-off energy (PCUT) were set at 0.7 MeV and 0.01 MeV, respectively [79].

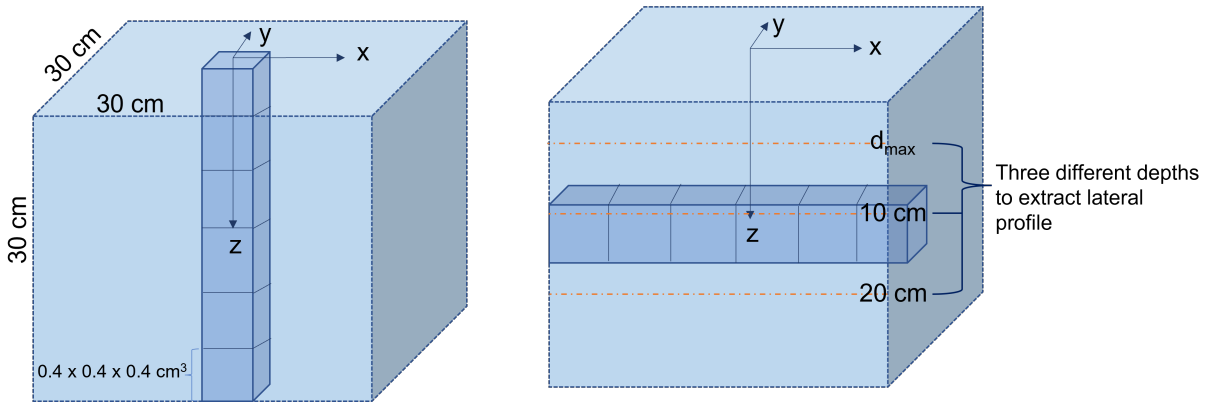

Figure 3.2: The voxelised phantom to extract the PDD and lateral profiles. These drawings are not to scale

The input parameters for dose calculation were entered and invoked by

DOSXYZnrc during the execution process. The file pertaining to dose calculation is appended in Appendix B. For the source parameters, all particles (electron, photon, and position) were chosen in order to irradiate the phantom via PSF (the BEAMnrc output). The number of histories was 4×10^9: this number was chosen so as to achieve a lower than 1% statistical uncertainty in dose calculation. It is recommended to use the HOWFARLESS algorithm for homogeneous phantoms: however, this should only be in order to significantly boost the efficiency of dose calculations in a short time by way of ignoring the voxel boundaries and being restricted only by the phantom outer boundary. The curve path of the particle steps that have been taken will be approximated for the dose deposition purpose (this is because solely phantom outer boundaries are considered with the HOWFARLESS algorithm); further details in [164]. Given that a homogeneous phantom is used in this study, the HOWFARLESS was turned on for this experiment. The air surrounding the phantom was distributed uniformly, with a thickness of 50 cm. Recycling was set at zero: this implies that the computer will use the optimum number of recycling iterations to ensure that the entire PSF_{IAEA} has been sampled. This technique is commonly applied when using PSF_{IAEA} as a way to increase the number of particles in order to obtain low uncertainty. Recycling boosts the number of particles by using the same particle whereas each duplicate (recycled) particle will follow a different path as it receives different random numbers during transport. This leads to a wider sampling of the transport space, thus reducing the statistical uncertainty [73, 165].

The radiation source was recalled in the DOSXYZnrc user code using source number 2. The key feature of this source that it can be incident from any direction, and this is essential in order to accurately mimic the linac rotation. The direction could be determined by three angles: theta (θ); phi (ϕ); and, phicol(ϕ_{col}). Furthermore, the user is able to describe the isocentre in x, y and z coordinates and the source to surface distance (SSD). The software defines the SSD from the target to the surface, implying it is very important to know precisely where the PSF was scored. For my model, the PSF was at 44.7 which means that the SSD should be at

50.3 cm in order to get the SSD of 95 cm, as shown in Figure 3.3. The isocentre was at zero for all three coordinates. The beam was placed at 0° by setting the three angles at 180°, 0°, 0° for theta, phi and phicol, respectively.

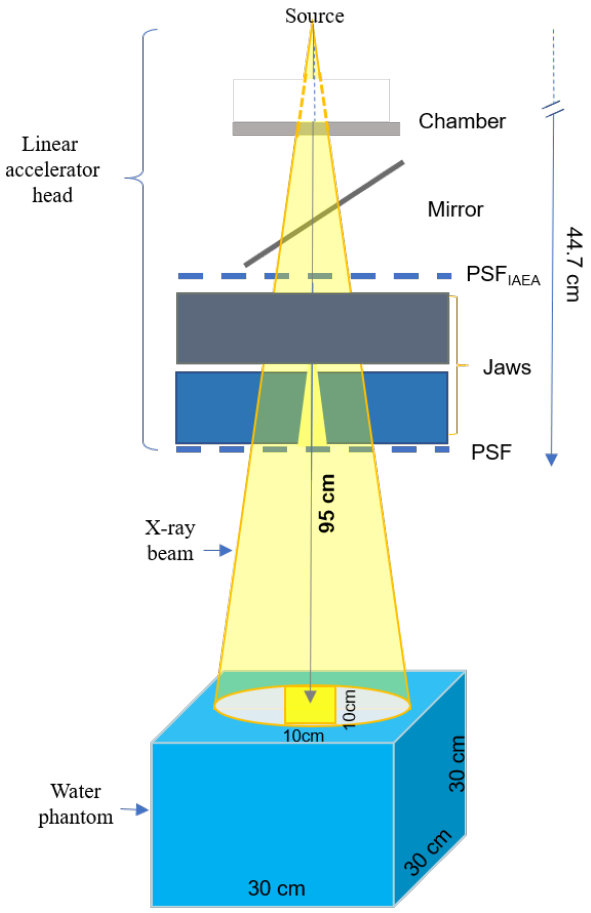

Figure 3.3: The simulation setup.

Variance reduction techniques were kept to a minimum. The range rejection was inactivated in order to avoid useful photons being decremented; however, the photon splitting was active with a splitting number of 80. The EGSnrc simulation parameters were kept the same as with the BEAMnrc. The dose calculation process was applied for 6 and 10 MV. The calculations were performed on a computer with an Intel Xeon (R) Gold 5118 with a 2.30 GHz processor.

3.4.3 PEGS4

The cross-section data of different materials is stored in the pre-processor EGS 4 (PEGS4). There are two available data sets in the software as default: the first is 521 ICRU (International Commission on Radiation Units and Measurements); and, the second is 700 ICRU. The former is for low energy photon beams (i.e., in the kV range), and the latter is for high energy beams (i.e., in the MV range) [73]. For each medium used in the simulation each file has information on the energy range, electron interactions, and physical density (including electron density, mass density and atomic number). Moreover, the software allows the user to define new materials. Since I dealt with high energy photons in this study (i.e., in the MV range), the materials cross section data was received from 700 ICRU.

3.4.4 The PDD and lateral profile measurement

The measurement data was received from Royal Free Hospital for Truebeam Varian linac. The data was given as a percentage depth dose (PDD) and dose profiles in cross plane format (i.e., in x direction) at 95 SSD for 10 cm $\times$ 10 cm, 15 cm $\times$ 15 cm for 6 and 10 MV beams. The lateral profiles were extracted at three different depths, namely: d_{max}, 10 cm and 20 cm for 10 cm $\times$ 10 cm; 15 cm $\times$ 15 cm for the 6 MV beam; and, 10 cm $\times$ 10 cm and 20 cm $\times$ 20 cm for the 10 MV beam. The measurement was made on a water block and it includes the 6 MV and 10 MV beam energies. It is worth mentioning that the measured maximum dose at the depth (d_{max}) is at 1.5 cm and 2.5 cm for 6 MV and 10 MV respectively.

The PDD was computed using this equation (3.1):

$$PDD = \frac{d}{d_{max}} \times 100 \tag{3.1}$$

Where d is the dose at any depth, and d_{max} is the maximum dose at the depth. For the lateral profile, the dose was normalised to the dose at zero (the centre).

For the purposes of validation, the simulated data was benchmarked to the

measured data sent from the Royal Free Hospital in terms of the PDDs as well as the lateral profiles at various depths (d_{max}, 10 cm and 20 cm). Specifically, this related to two beam energies, and for various field sizes. These were (10 cm $\times$ 10 cm) for two beam energies, specifically 15 cm $\times$ 15 cm for 6 MV and 20 cm $\times$ 20 cm for 10 MV. For a clear assessment, the percentage relative dose was plotted against the depth using equation (3.1) for PDDs. They were extracted from the central axis of the phantom from 0 to 30 cm whilst the lateral profiles were normalised at a dose from zero in the x direction (cross plane) for various depths.

3.4.5 Evaluation methods

The comparison between the calculated data and the measurement data was made via the 1D gamma analysis and the percentage difference (these are the standard tools for comparison in radiotherapy). Gamma analysis is a quantitative tool since it considers the differences in dose and distance whilst the percentage (%) difference calculates the difference compared to the reference data. The percentage difference was calculated using equation 5.2. The dose profile and percentage depth dose (PDD) were extracted at different depths (for later profiles only), and for different field sizes. For validation, the simulated data was compared to the measured data using 1D gamma analysis with various criteria (i.e., 1 %/ 1 mm and 2 %/ 2 mm). This method was used since the gamma analysis sensitivity decreases as the criteria become looser, whereas in radiotherapy precision is necessary [166]. Furthermore, it is impossible to mimic the exact linac without obtaining the precise dimensions from the manufacturer, and using the PSF_{IAEA} as a radiation source limits the beam tuning since changing the incident electron energy may sometimes diminish the variations.

The tolerance level for this study was set to be equal or bigger than 95% ($\geq$ 95%). In radiotherapy, the tolerance level is placed at 95% in order to ensure the process is operating normally and correspondingly to the plan (see Figure 3.4). The process in this area (green) is subject to random errors only given that the area ($\geq$ 95%) will contain the true parameter value or acceptable parameter value

for safe treatment. This is because the confidence interval (95%), statistically, will contain the true parameter value and this implies that 5% of the individual measurements/points may exceed the limit [167]. The action limit is the amount of permitted deviation from the plan without risking harm to the patient (namely, between 95%-90%, which is shown in yellow). Anything below 90% means that the treatment is prohibited [85, 168].

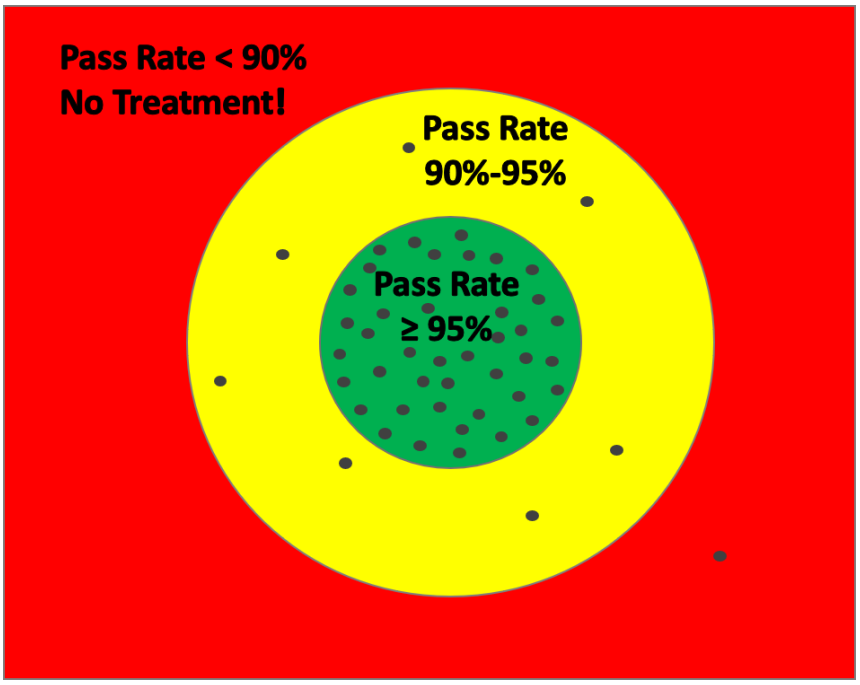

Figure 3.4: The pass rate $\geq 95\%$ is where the process considered to be operating normally (green circle). Between 90% and 95% in the yellow circle starts warning that a system is deviating. Below 90%, the treatment is prohibited [85].

3.5 Results and discussions

3.5.1 The phase space files

The PSFs were scored underneath the jaws at 44.7 cm in the z plane (see Figure 3.3) to be used later for dose calculation. The files were analysed via Beamdp user code using the x and y scatter plot option in order to verify particle distribution and field size. Figure 3.5 shows 70000 particles distributed homogeneously for 6 MV (10 cm $\times$ 10 cm) and 10 MV (20 cm $\times$ 20 cm), and pinned from -20 cm to 20 cm in x

and y orientations. These particles are the residual particles from around 9.86×10^8 particles that were initially in the PSF_{IAEA}, after going through the stimulation. The other particles will have been absorbed by jaws or deviated from the path (i.e., are outside the irradiated field). The software plotted the two overlapped PSFs: the large one represents the PSF_{IAEA} (the green square); the small one (the red square) is the collimated PSF using jaws resulting from the BEAMnrc simulation. A similar result was found for the other field sizes. Consequently, they are not displayed.

Looking at Figure 3.5, the maximum field sizes can be achieved with International Atomic Energy Agency PSFs are: 35.84 cm $\times$ 35.84 cm at 100 cm SSD, and 34 cm $\times$ 34 cm at 95 cm SSD. This is because the files were scored at 27.9 cm with 10 cm $\times$ 10 cm field size. This is one downside of using PSF_{IAEA}.

Further analysis was made to list file parameters, specifically: including particle and photon numbers in order to ensure that the files contain photons and particles. In addition, I looked at the highest energy scored in the file given that the beam is not mono-energetic. It was found that the highest energy in the spectrum of 6 MV beam is 6.3 MeV, and in a 10 MV beam is 10.9 MeV.

3.5.2 The PDDs and lateral profiles comparisons

Graphs of PDD in Figures 3.6, 3.7, 3.8 and 3.9 display that the maximum dose (d_{max}) for simulated PDD is overlapped with d_{max} of the measured PDD for both beam energies. The d_{max} was recorded at 1.4 cm for 6 MV, and 2.2 cm for 10 MV. The highest discrepancies were noticed at the build-up region, specifically the $< d_{max}$ region. Beyond the build-up region ($> d_{max}$) the MC calculation agrees strongly with the reference data, with a percentage difference between -0.06% and 0.0013% for 6 MV, and between -0.05% to 0.002% for 10 MV for both 10 cm $\times$ 10 cm and 15 cm $\times$ 15 cm filed sizes. This could be because the scatter contribution from the treatment head decreases as the depth increases. Such a contribution can lead to high statistical fluctuation and thus higher uncertainty in this area [169–172].

The gamma indices for PDDs are shown in Table 3.2. They were calculated

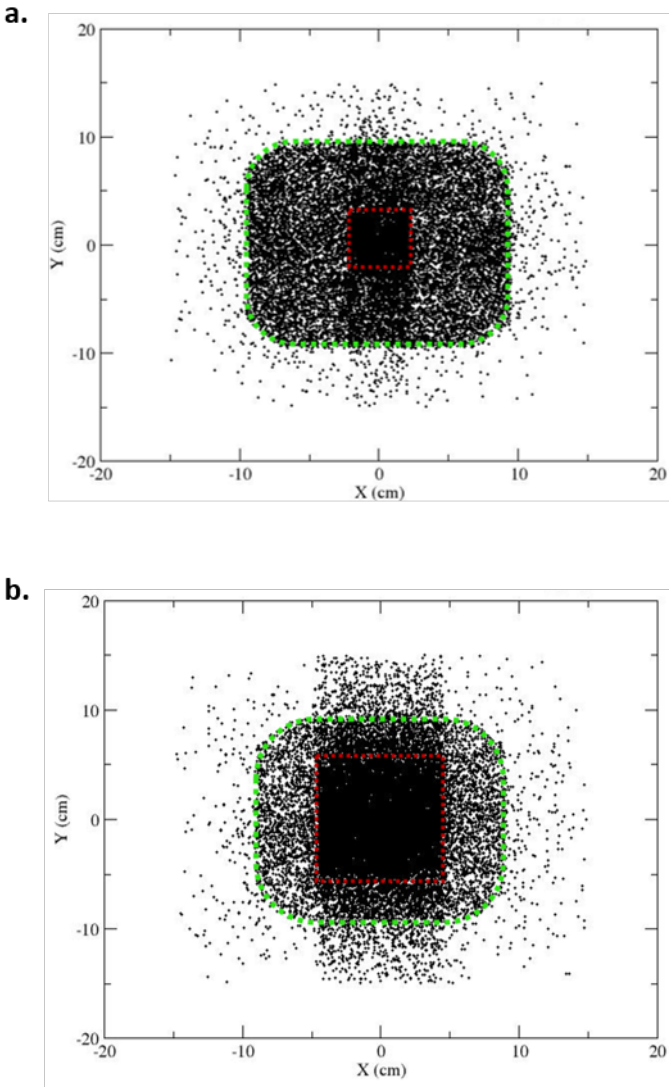

Figure 3.5: The scatter plots in x and y directions at 44.7 cm (below linac jaws) **a.** 10 cm ×10 cm for 6 MV **b.** 20 cm × 20 cm for 10 MV. The green square represents PSF_{IAEA} and the red square represents the the resultant field size from the BEAMnrc simulation.

with different criteria (namely, 1%/ 1 mm and 2%/ 2 mm) and with a tolerance level of $\geq 95\%$. More than 98% of the points from MC calculations passed a 1%/ 1 mm gamma analysis, whilst all points passed 2%/ 2 mm criteria when compared against measurements for both field sizes of the 6 MV beam. For the 10 MV, 96.3% and 98% of the simulated points had $\gamma < 1$ with 1%/ 1 mm gamma criteria at 10 cm $\times$ 10 cm and 15 cm $\times$ 15 cm jaws open, respectively. All points in the simulated PDD passed 2%/ 2 mm criteria at both field sizes.

The lateral profiles for the field sizes of 10 cm $\times$ 10 cm and 15 cm $\times$ 15 cm for the 6 MV beam, and 10 cm $\times$ 10 cm and 20 cm $\times$ 20 cm for the 10 MV beam are shown in Figures 3.6, 3.7, 3.8 and 3.9 at differing depths, d_{max}, of 10 cm and 20 cm. In the flatness region (between the shoulders) where there is no dose gradient, the MC dose calculation agreed closely with the measurements: in other words, all the points in this region passed 2%/2 mm gamma comparison. The majority of variations in all lateral profiles was more pronounced in penumbra regions, within the gradient area, at the depths, d_{max}, of 10 cm and 20 cm. The field width difference comparisons are listed in Tables 3.3 and 3.4 for 6 MV and 10 MV respectively. These outcomes are as similar as to those reported in numerous other studies [169–171].

The highest discrepancies were observed in 20 cm $\times$ 20 cm. This could be due to several factors. One is latent variance, where there is a certain limit of variance which cannot be removed despite using the VRTs to increase the particle numbers and reduce the variance. The smallest possible variance value is termed the latent variance [172, 173]. This variance is inversely proportional to the number of particles, and 20 cm $\times$ 20 cm PSF scored the lowest number of particles. As a remedy for this issue, a larger size of PSF_{IAEA} is necessary [169, 173]. The other possible reason is due to the long time needed to simulate the large field sizes: this can result in less efficiency since it is inversely related to the simulation time [12]. Furthermore, inaccurate initial electron parameters may cause inconsistent outcomes within the gradient region [174].

Tables 3.3 and 3.4 demonstrate the gamma results and field width difference of lateral profiles for both energies, at two field sizes at various depths. More than 97% of the points of the calculated data agreed with the measured data at 2%/ 2 mm gamma criteria for both field sizes of 6 MV and the 10 cm $\times$ 10 cm field size of 10 MV. For 20 cm $\times$ 20 cm, the passing rate was the lowest: 87% of the MC points had $\gamma < 1$ based on 2%/ 2 mm. This low rate might be due to the low particle numbers in the phase space file.

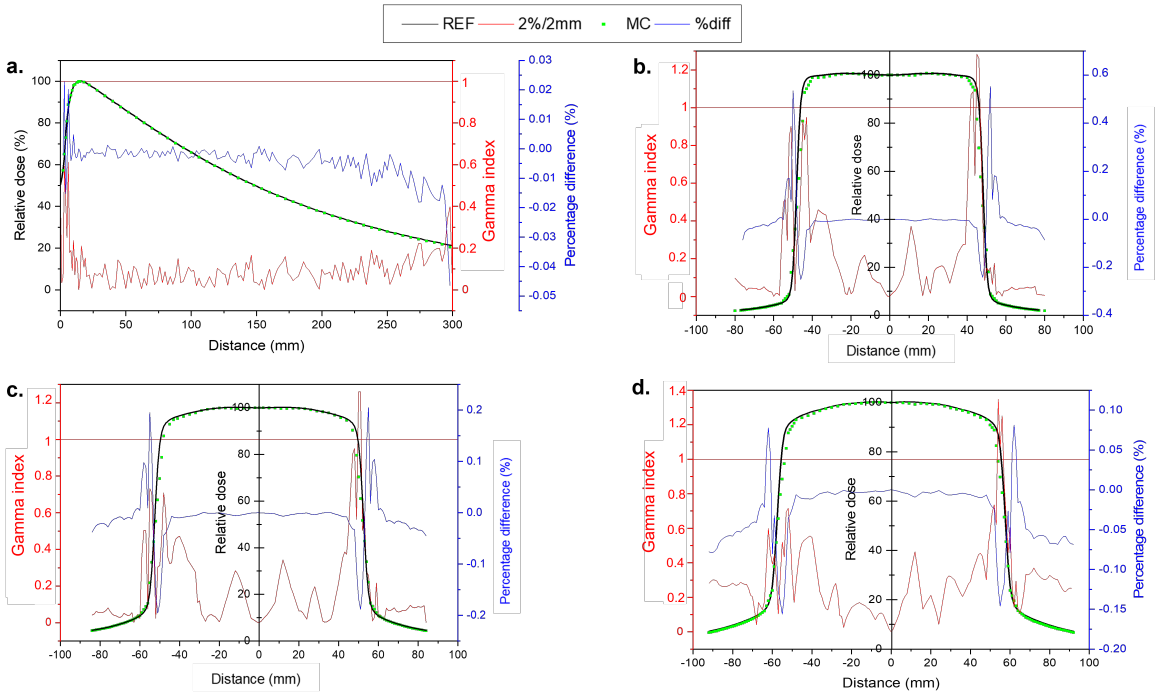

Figure 3.6: PDD (a) and lateral profiles at different depths d_{max} (b), 10 cm (c) and 20 cm (d) for 6 MV beam 10 cm x 10 cm field size.

The field width difference was computed in order to investigate the variations in width between the calculated and the experimental measurements. The variations ranged from -2 mm to -0.9 mm for 10 cm × 10 cm and 15 cm × 15 cm for 6 MV. For 10 MV, they were between 2 mm to 2.5 mm for 10 cm × 10 cm, and between 7 mm to 8.7 mm for 20 cm × 20 cm. The beam of 10 MV at 20 cm × 20 cm has the highest variations in field width given the low number of particles in PSF. For MC simulation in general, the penumbra is the most difficult region to simulate since there is a smaller number of particles in that region thereby leading to vast statistical fluctuations [169–172]. The percentage difference results show that the differences in the penumbra region reduced with low energy: this is due to a reduced scatter contribution in dose calculation [169–172].

In the following chapters, this beam will be used for irradiated phantoms based on real patient data in order to evaluate EPID suitability to detect errors emerging from anatomical changes. As such, the discrepancies will have a minute effect on the results. Based on the literature, where MC results were benchmarked to mea-

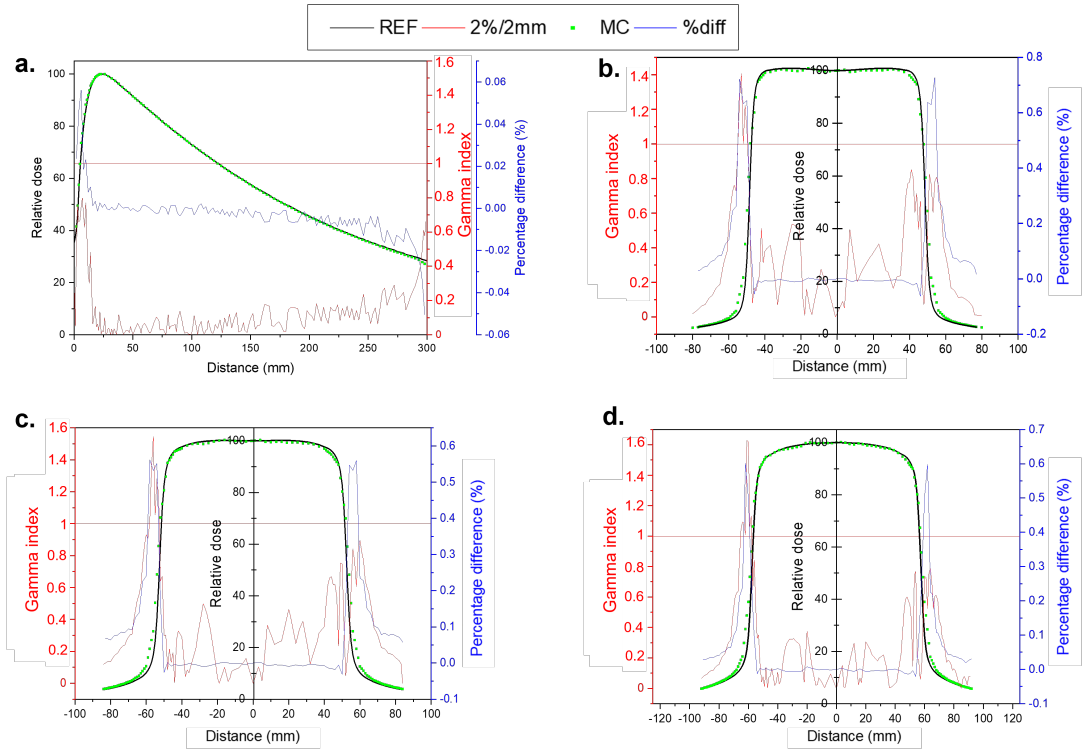

Figure 3.7: PDD (a) and lateral profiles at different depths d_{max} (b), 10 cm (c) and 20 cm (d) for 10 MV 10 cm x 10 cm field size.

sured data, statistical uncertainty of less than 1% and a gamma level of 95% have a very small impact on dose calculation [175, 176]. Consequently, for the 6 MV beam the discrepancy in the build-up will not affect EPID since the discrepancies decrease with depth. In my case, it is difficult to estimate the impact of dose discrepancy in the penumbra region on EPID as it is necessary to benchmarked the simulation results to clinical EPID. However, according to [177], statistical uncertainty $< 1\%$ in MC has a negligible impact on dose analysis. Moreover, the discrepancy penumbra region decreases as a function of depth, however, in order to diminish it as much as possible the pixels outside the ROI are set to a value of zero. This is done to avoid blurring the anatomical changes happening close to this region since this may cause a devaluation of EPID detection ability. This will be explained in detail in section 4.5 in the next chapter (4). Alternatively, the voxel size in the penumbra region can be increased to allow scoring an increased number of photons, thereby leading to reduced uncertainty [163].

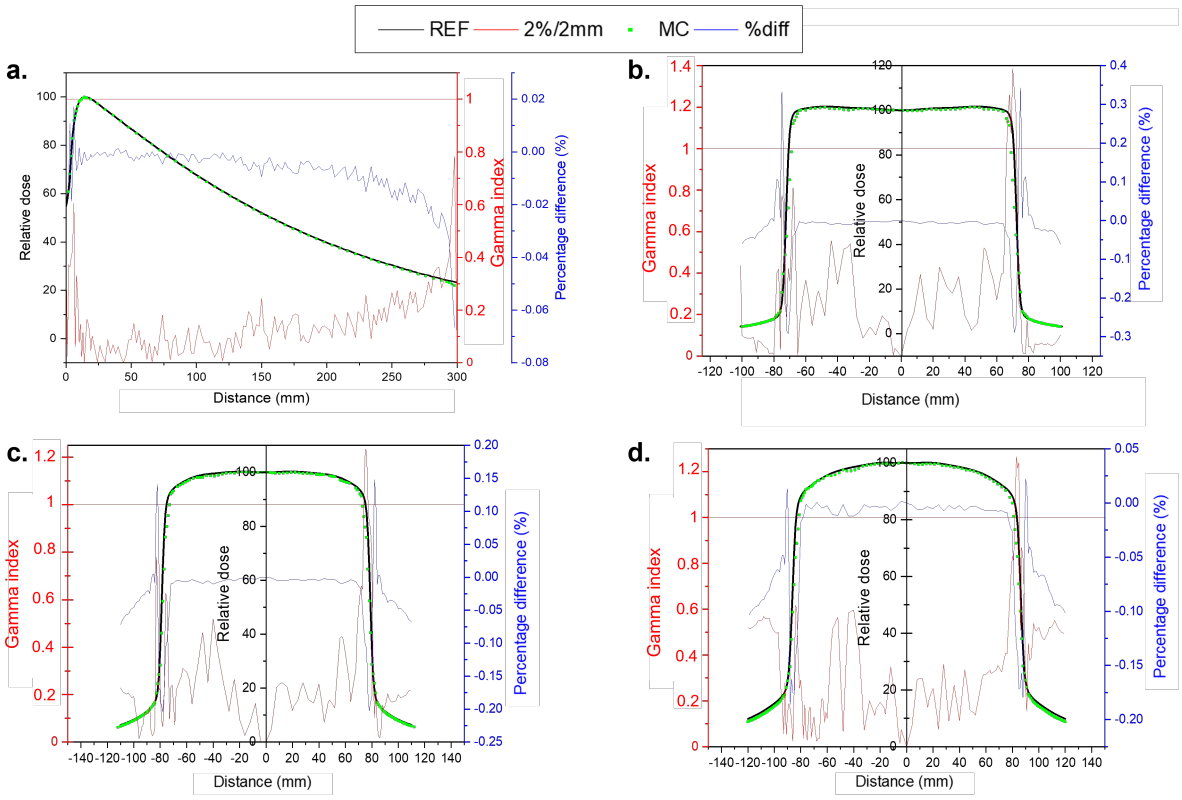

Figure 3.8: PDD (a) and lateral profiles at different depths d_{max} (b), 10 cm (c) and 20 cm (d) for 6 MV 15 cm x 15 cm field size.

Table 3.2: The gamma passing rate for PDDs of two beam energies

Radiation energy	6 MV		10 MV	
Field size	10×10	15×15	10×10	15×15
1%/1mm Gamma	98.7%	98.1%	96.3%	98%
2%/2mm Gamma	100%	100%	100%	100%

Table 3.3: The gamma passing rate for lateral profiles at different depths for 6 MV

Radiation energy	6 MV					
Field size (cm^2)	10×10			15×15		
Depths (cm)	d_{max}	10	20	d_{max}	10	20
2%/2mm Gamma (%)	97.4	98.8	98.4	97.0	98.2	98.3
The field width difference (mm)	-1.4	-1	-0.9	-2	-1.6	-1.7

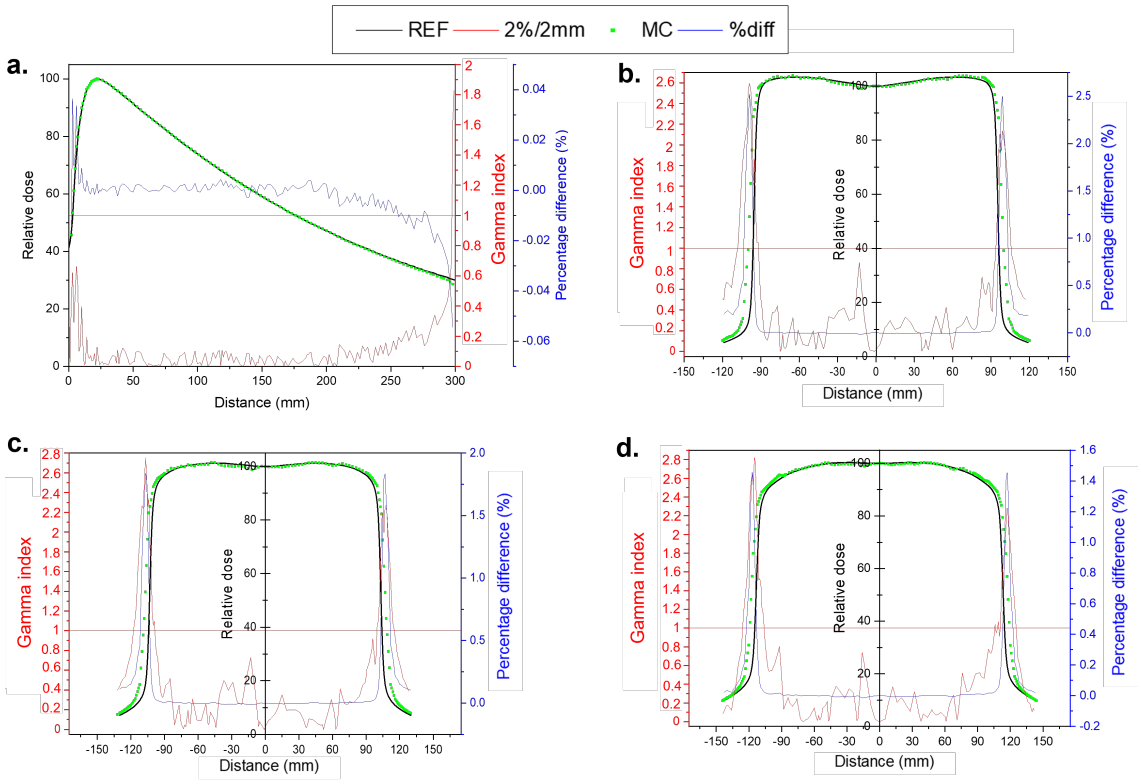

Figure 3.9: PDD (a) at 15 cm x 15 cm and lateral profiles at different depths d_{max} (b), 10 cm (c) and 20 cm (d) at 20 cm x 20 cm for 10 MV.

Table 3.4: The gamma passing rate for lateral profiles at different depths for 10 MV

Radiation energy	10 MV					
Field size (cm^2)	10×10			20×20		
Depths (cm)	d_{max}	10	20	d_{max}	10	20
2%/2mm Gamma (%)	96.1	96.4	95.7	87.8	86.5	87.1
The field width difference (mm)	2	2.4	2.3	7	7.8	8.7

3.6 Conclusions

In this chapter, a virtual linac was built and calibrated in order to be used for the next step. The 6 MV and 10 MV beams were mimicked by means of PSF_{IAEA} and BEAMnrc which are dedicated to build and compile a linac according to the user input. This produces the phase space files which were later used for dose calculation. DOSXYZnrc was utilised in order to calculate the dose in the water tank. For the purposes of verification, the PDDs and lateral profiles at different depths were extracted in order to be compared to measured data provided by the Royal Free Hospital.

With a tolerance level of 95%, the results of gamma analysis displayed a high agreement. Each of the MC points of PDD passed 2%/ 2 mm gamma comparison for two field sizes (at 10 cm $\times$ 10 cm and 15 cm $\times$ 15 cm) for both 6 MV and 10 MV. It was noticed that the inconsistency was more pronounced at the build-up region due to head treatment scatter, however, in the equilibrium region the differences were negligible. The percentage difference was very low between the simulation and the measurement. The PDD of both energies had a percentage difference between – 0.06% to 0.002% at 10 cm $\times$ 10 cm and 15 cm $\times$ 15 cm.

For the lateral profiles, the penumbra regions scored the highest inconsistent results. This disagreement within the gradient region increased with the larger field size due to the high statistical fluctuations resulting from a lack of particles. It did, however, reduce with depth since there is an electron equilibrium and less radiation scatter as depth decreased. The MC flatness region, outside the gradient area, had good agreement with the reference data. For 10 cm $\times$ 10 cm field size, more than 95% of the simulated points passed the gamma analysis for both energies. For 15 cm $\times$ 15 cm field size, more than 97% of the simulated points passed the gamma analysis for 6 MV beam. Yet, for 20 cm $\times$ 20 cm field size at both energies, around 14% of the points, located mainly in the penumbra region, failed 2%/ 2 mm gamma comparison with reference to the measured data. As a remedy, this area will be eliminated so as to avoid any complications and erroneous blurring. Alternatively,

the voxel size in the penumbra region can be increased in order to allow scoring a higher number of photons, thereby leading to lower uncertainty.

To conclude, the beam energy 6 MV is eligible to be used for the next step, namely that concerned with EPID simulation and dose verification. This supports the claim that the radiation beam can be simulated and replicated via MC software (specifically, BEAMnrc (EGSnrc user code)) in order to conduct computational trials which will successfully mimic clinical experiments.

Chapter 4

MC system applications- Anatomical changes: parotid glands shrinkage for nasopharyngeal cases during radiotherapy

4.1 Overview of chapter

The main aim of this chapter is to evaluate EPID sensitivity to parotid gland changes in head and neck patients owing to the fact that morphological changes frequently occur during radiotherapy treatment. EPID is easily accessible in many radiotherapy departments, and can be used to monitor such changes by applying the detector during radiotherapy in order to test its capabilities of quantitative dose mapping.

Based on computational calculations, and using the virtual linac discussed in the previous chapter (3), the sensitivity of EPID was quantified to the parotid glands' variations in a nasopharyngeal case. According to [108], re-planning in head and neck patients, it is suggested that when parotid gland volume is reduced by 24-30%, consequently, EPID should be able to detect and suggest re-planning for this volume range.

The outcomes of this work resulted in the following:

- **Alzahrani, H.**, Gidenne, M., Collins-Fekete, C. A., Royle, G., Ricketts, K. (2020). In Silico Study of Investigating the Sensitivity of Three EPID Models to Anatomical Changes. International Journal of Radiation Oncology, Biology, Physics, 108(3), e263-e264. Poster abstract publication.

4.2 Hypotheses of chapter

- EPID works not only for position verification, but it can also be used for dose verification via quantitative dose mapping given that it is sensitive to dose differences arising from soft tissue discrepancies which will be utilised for adaptive radiotherapy. This will eventually lead to a successful treatment outcome for the patient and therefore an improved quality of life.

- A simple EPID structure can replace the complex EPID structure in computational studies for rapid simulation and improved efficiency.

4.3 Criteria of success

Similarly to chapter 3, the gamma analysis in addition to the sensitivity index were adopted as the main assessment methods for the performance of the simulated portal imaging devices (namely, PID) in detection errors arising from anatomical changes during radiotherapy. For instance, parotid shrinkage in nasopharyngeal cancer patients. The gamma analysis provides a dose distribution comparison by combining both dose difference (DD) and distance to agreement (DTA) into a single quantity. The gamma analysis level is set at 95% since it is commonly used and recommended by [178]. This is explained in more detail in section 3.4.5 in chapter 3. Consequently, the dose difference between the reference and the evaluated images below this level is considered not passable. The sensitivity index describes the relationship between the mean difference (signal) and the standard deviation (noise)

difference of two distributions. A higher index indicates that the error has a larger effect on dose distribution and therefore can be more readily detected [179].

4.4 Materials and methods

4.4.1 Portal imaging devices (PIDs) configurations

Three different configurations representing the EPID are involved in this study. These configurations vary in structural complexity. The simplest model was a water block, the others consisted of 5 and 17 slabs containing one gadolinium oxysulfide (Gadox) layer. The total dimensions for the three devices were 30 cm $\times$ 30 cm in x and z directions: however, they varied in the y direction as shown in Figure 4.1. The exact overall dimensions are: 30 $\times$ 30 $\times$ 5 cm^3; 30 $\times$ 30 $\times$ 5.21 cm^3; and, 30 $\times$ 30 $\times$ 10.34 cm^3 for water, 5- and 17 –slab, respectively.

- **Water-slab**:

  The first PID model is a water slab only. Since it has the simplest geometry, it has some advantages over the other two. One benefit is that it directly measures the dose in water, dissimilar to the PID based on Gadox, whereas the signal is primarily proportional to the absorbed energy in the scintillation layer [180]. The other advantages are that it is fast to simulate with low uncertainty, and is also effortless to implement because it contains only one material. Furthermore, in Gadox-based PID, the copper and phosphor layers contain a high atomic number thereby producing more low energy photons due to the photoelectric effect. Consequently, the absence of the copper layer in this model could decrease the over-response [181]. For this model, the PID response was extracted from d_{max}.

- **Five-slab**:

  The second geometry is a simplified Gadox-based PID consisting of five layers with a 1 cm thick of Gadox scintillator adopted from [182]. This particular system was developed for precise dosimetric verification of intensity

modulated radiotherapy (IMRT) treatments. It was reported that this simple structure EPID scored less than $\pm 5\%$ dose difference within the beam against the treatment planning system and film. Consequently, this model was taken into account as having fewer layers (the main layers only) which may, therefore, result in reduced simulation time and better efficiency. To that end, it can be suggested as a suitable replacement for the complex PID structure in the computational studies presented in this study. The model considers only the basic components of the EPID structure: a thin layer of copper acting as build up and removing the low energy photons; the phosphor layer, which converts the photons into lights to be collected by the next layer; namely, a glass layer with embedded electronics for readouts. The water layers above and below the three mentioned layers are intended to account for all materials lying above and below them within the EPID apparatus [183]. The dimension is 0.5 cm $\times$ 0.5 cm in x (cross-plane) and z (in-plane) direction, however, the thickness varies in y (depth) direction. The voxels in the Gadox layer have dimensions of 0.5 cm $\times$ 0.5 cm $\times$ 0.5 cm in order to obtain uncertainty below 1%. According to [184], statistical uncertainty of 2% or less does not significantly affect the results of the beam simulation.

- **Seventeen-slab**:

  The third geometry consists of 17 layers based on a 1 cm thick Gadox layer taken from [185]. The voxel dimensions are 0.5 cm $\times$ 0.5 cm in x and z directions, however, the thickness varies in y direction. The voxel size in the Gadox layer specifically has dimensions of 0.5 cm $\times$ 0.5 cm $\times$ 0.5 cm in order to reach a compromise between resolution and simulation speed, and also in order to obtain uncertainty below 1%. This model is most likely accurately describes the clinical EPID: however, due to the many layers involved, the simulation will require a long time for processing. The copper layer of 1 mm minimum prior to a phosphor screen is essential for the Gadox-based detectors to be able to absorb the low energy photons. The signal in the two Gadox-based models is proportional to the dose as is the case with all Gadox-

based detectors currently available in clinics. Hence, the EPID response is calculated from the energy deposition within Gadox material for these two Gadox-based models. The density correction files for the undefined materials were generated using the EStar program, provided by National Institute of Standards and Technology (NIST). This calculates the stopping-power, range and radiation yield tables for electrons in a custom material [186]. Subsequently, the data file was appended to 700 ICRU via EGSnrc GUI (EGSnrc user code).

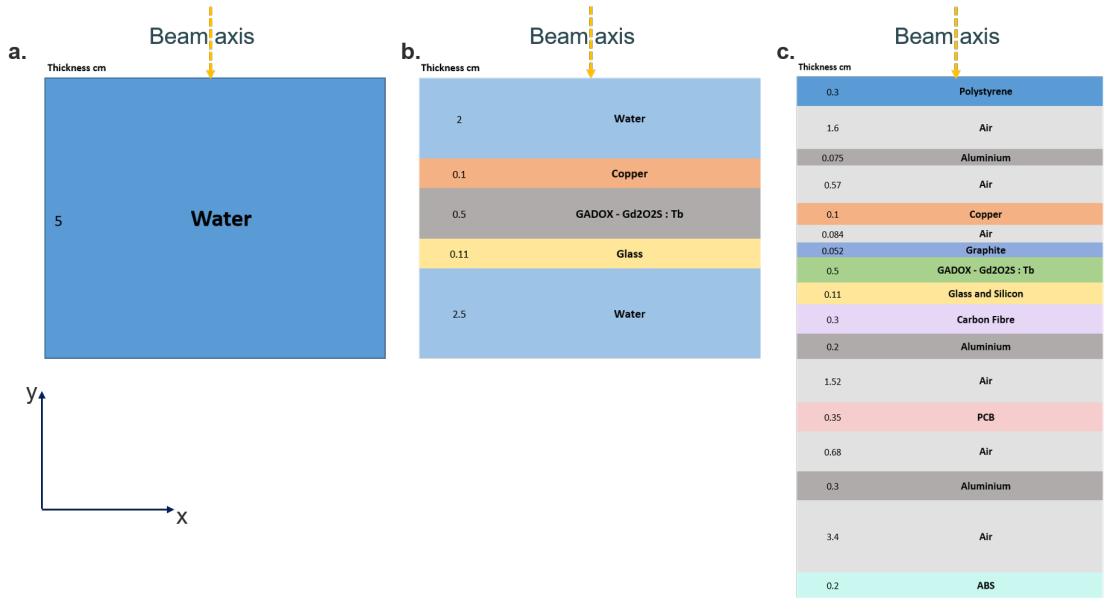

Figure 4.1: Schematic drawing of the three PID models examined in this study **a.** water-slab, **b.** 5- slab, **c.** 17- slab. These drawings are not to scale.

4.4.2 Phantom preparation

The head and neck areas hold many critical organs and losing them can lead to a dramatic reduction in life quality. Some of these organs are characterised by high radiosensitivity, for instance the parotid glands [103]. The parotid glands display acute and chronic responses to radiotherapy, and for this reason, the dose has been restricted to be less than 25 or 26 Gy in order to avoid complications such as xerostomia (i.e., a dry mouth) [103, 187, 188]. Furthermore, radiotherapy of head and neck areas displays a high degree of reproducibility and low random and sys-

tematic errors compared to radiotherapy of the pelvis, as reported in [189]. This is because in cases involving the head and neck, the immobilisation devices (called thermoplastic face masks) have contributed to reduction of setup uncertainties and increased the reproducibility [190]. In turn, this results in a low contribution of the uncertainty due to patient positioning errors as part of the EPID response. Since this simulation does not account for such errors, head and neck cases were selected in order to obtain a closer response to real ones via EGSnrc simulation. Based on these factors, head and neck cancer was chosen for this study.

- **Variations in the parotid glands volume during radiotherapy**

  This step aimed to extract the most commonly volumetric variations occurring in nasopharyngeal cases. Apolline Assaud, an exchange student from France, was responsible to collect this data, whilst I subsequently decided which data would be considered for simulation. For this purpose, a total of 2142 articles discussing the anatomical changes in nasopharyngeal cases during radiotherapy from 2004 to 2018 were screened and assessed for eligibility. Some studies were excluded for the following reasons: unable to access the full text article; abstract only; non-relevant outcomes; and, non-relevant tumour location. Ultimately, five articles were deemed suitable for inclusion in the eventual analysis (see Figure 4.2).

  The outcome assessment of previously published studies discussing the parotid gland volume variation during radiotherapy treatment is illustrated in Figure 4.3, a [191–195]. These findings were observed in 46 patients (see Table 13) who reported with the parotid gland volume change in nasopharyngeal cases, and being at different cancer stages (see Figure 4.3, b). It is found that radiation can cause alteration in gland volume from -6% up to -84% (the minus sign indicates a reduction) in nasopharyngeal cases. The common volume of change is between -37% and -46.9%. Accordingly, the gland volume variations, in this present study, were selected following these meritorious figures.

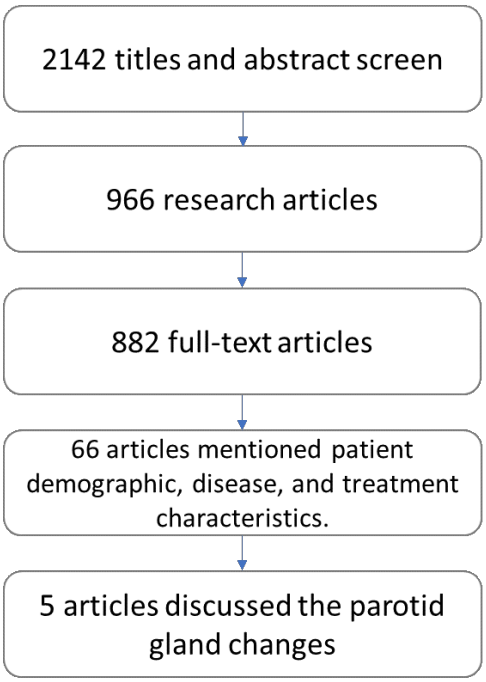

Figure 4.2: PRISMA diagram of literature search results disposition.

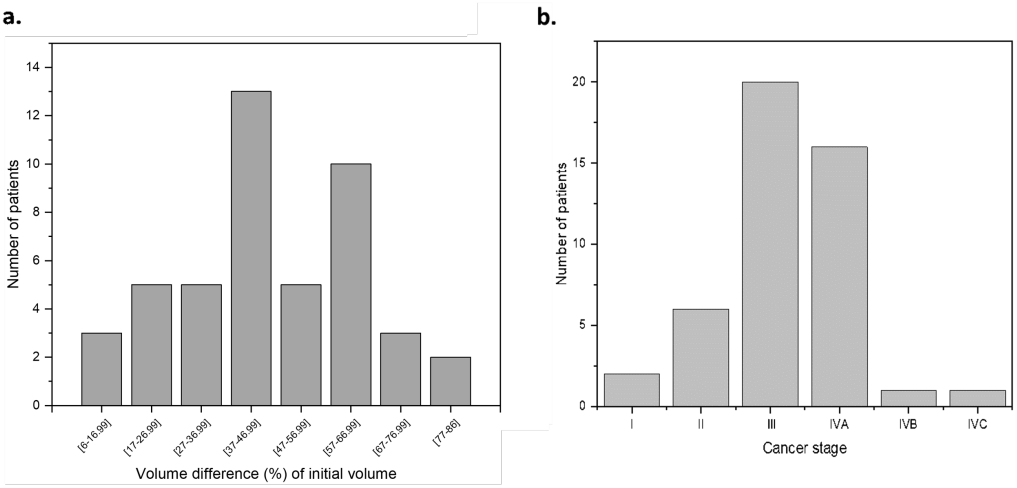

Figure 4.3: The volume variation in the parotid glands during the radiotherapy in nasopharyngeal cases (a) and the cancer stage (b) [191–195].

- **Organ deformation**

  The study was initiated with a retrospective case of nasopharyngeal cancer received from University College London Hospital (UCLH). It included DICOM images of the CT scan, manufactured by a GE medical system, using a helical mode scan with 120 kVp and 2.5 mm slice thickness. These images were used for an IMRT plan. The patient data was anonymous for patient

Table 4.1: Summary of patients characteristics adopted from five articles [191–195]

Study	**Patients no.**	**Gender**	**Age (years)**	**Treatment type**	**Monitoring tool of parotid glands changes**
Wu et al. (2018) [191]	30	Males and Females	12- 72	IMRT chemoRT	kVCT at 1^{st}, 10^{th} and 30^{th} fractions
Powell et al. (2013) [192]	1	Male	42	IMRT chemoRT	Conventional (CT and MRI) and functional (MRI and PET/CT) imaging at baseline and following two cycles of chemotherapy prior to definitive chemoradiotherapy
Lee et al. (2008)* [194]	10	-	-	IMRT chemoRT	kVCT and MVCT
Han et al. (2008) [193]	5	Males	44-56	IMRT	kVCT and MVCT
Lee et al. (2008)* [195]	10	-	-	IMRT chemoRT	MVCT

* These two studies used the same patient data.

privacy and security.

The left parotid gland in DICOM images of the nasopharyngeal case was selected to be locally deformed since the simulated beam was left anterior, oblique. The deformation was performed using deformation algorithms in the ImSimQA software toolkit (Oncology Systems Limited, Shrewsbury, Shropshire, UK). This software allows the user to manipulate the volume by placing landmark points at the edge of the organ (see Figure 4.4). A large number of landmark points will give enhanced control of the deformation. The deformation was performed on contour-based CT images in order to easily define the organ and thereby avoid the issues associated with low contrast images. The normal volume of the left parotid gland was 25.39 cm^3 and it was reduced by 5.6%, 9.6%, 17.7%, 26.3%, 31.9%, 38.8%, 44.9%, 50%, 60%, 68.4% and 72% and then saved as DICOM files. The gland is shifted towards the head centre after the shrinkage by default which make the gland close to the high dose delivered to tumour volume [191–195]. The weight loss is not included

in this simulation. These percentages of volume reduction were selected to reflect typically observed volume changes between -6% to -84% during treatment, and based on statistical outcomes from previously published studies (see Figure 4.3, a). The phantoms were created via CTCREATE tool available in egsnrc in order to make phantoms compatible with BEAMnrc user code. The voxel dimensions of 0.25 cm $\times$ 0.25 cm $\times$ 0.25 cm were used for phantoms in order to reach a compromise between resolution and simulation speed (see appendix B.1).

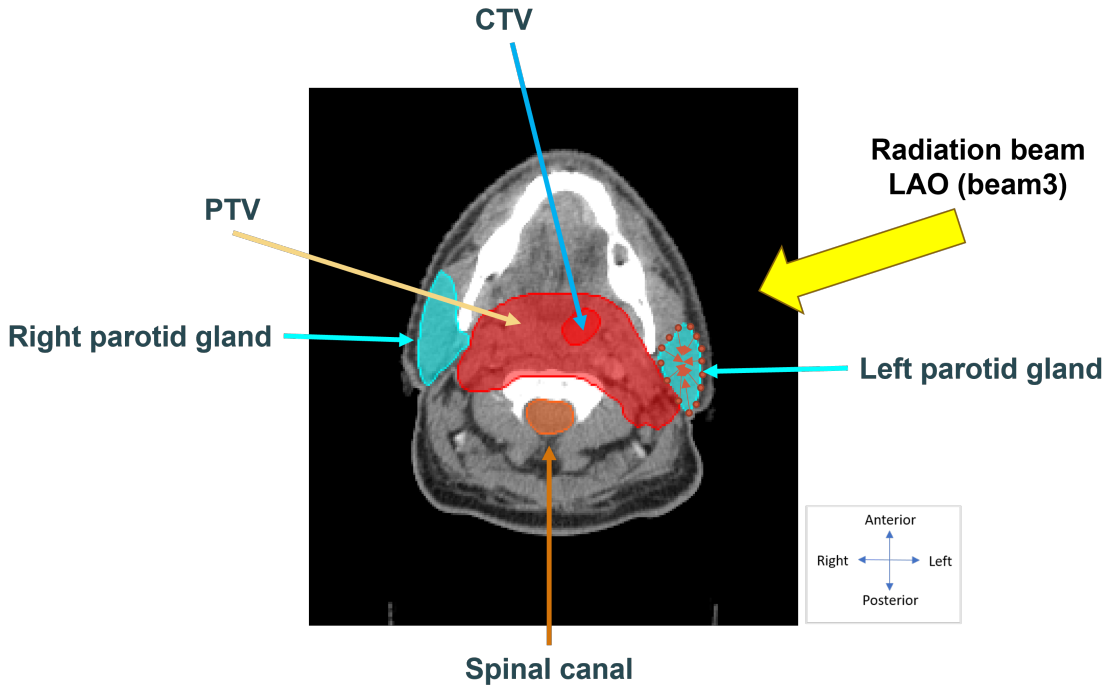

Figure 4.4: The left parotid gland location and beam direction. The red points around the parotid gland were placed to shrink (deform) the selected gland in ImSimQA

4.4.3 Inserting the phantom into the simulated beam of intensity modulated radiation therapy (IMRT)

The two main steps of this simulation are IMRT beam simulation (to generate the 4D PSF_{IAEA}), and obtaining the EPID response.

- **Single IMRT field simulation and 4D PSF_{IAEA} generation:**

The aim of this work was to investigate the impact of parotid gland dimension changes measured via EPID signal in order to identify whether transit EPID measurement is sensitive to parotid gland shrinkage, and following, the magnitude of shrinkage that EPID can detect. It is not absolutely necessary to include EPID from each irradiated beam given that similar results could be gained with an EPID response utilising a limited number of beams. Indeed, anterior or lateral views are commonly used [118]. Accordingly, one field from a head and neck IMRT plan was selected to test sensitivity in relation to detecting parotid gland changes. The left anterior oblique (LAO) field (see Figure 4.8) was selected since it was the field that demonstrated the greatest coverage for the parotid gland, planning target volume (PTV) and clinical target volume (CTV) within the beam's eye view (see Figure 4.4). Moreover, in clinical terms LAO would be the most useful field in detecting this anatomical change. The other IMRT fields demonstrated the lowest parotid gland coverage, and hence would have little clinical benefits in detecting anatomical changes to the parotid gland (see Figures 4.5 and 4.8). Consequently, they were excluded in order to test the hypothesis that EPIDs can detect changes in the parotid gland. Figure 4.7 shows the tumour volumes (CTV and PTV), and main organs at risk.

EGSnrc has been widely used and has proven its ability to replicate IMRT plans [182, 196–199]. Firstly, the IMRT plan received from UCLH (where the patient was being treated) was analysed in order to extract the key parameters. These were: monitor unit index; the isocentre; MLC and jaws positions; and, gantry angles for the control points. The IMRT plan consists of seven beams to irradiate the patient from different directions as is shown in Figures 4.5 and 4.6. For the IMRT simulation, the user must supply a file of the MLCs opening data in a specific format as is explained in the BEAMnrc manual [73]. The file was created using an in-house MATLAB code (see appendix C). The isocentre was at (0.11, -7.40, 0.00) for x, y and z respectively. The main IMRT parameters are listed in Table 4.2. The dose rate was

400 MU/s. A dynamic delivery IMRT field file contains a number of control points which defined MLC shapes to deliver a marked fraction of the monitor units. For LAO, the control points were 159 points. Table 4.3 lists the angles used for each beam in terms of gantry, collimator, and couch rotations. The beam coordinates where transformed from DICOM in order to comply with BEAMnrc and DOSXYZnrc coordinates. This was accomplished by using the method published [200].

Table 4.2: The main parameters of the IMRT plan used in this study, PLO= posterior left oblique, LPO= left posterior oblique, LAO= left anterior oblique, ANT= anterior, RAO= right anterior oblique, RPO= right posterior oblique, PRO= posterior right oblique

Patient case	Nasopharyngeal carcinoma
Treatment planning technique	IMRT
Dose rate	400 MU/s
Source-axis distance (SAD)	100 cm
MLC	Dynamic
Cumulative MasterSet weight (MU index)	0-1
Number of beams	7 beams (PLO, LPO, LAO, ANT, RAO, RPO, PRO)
Control points of beam3 (LAO)	159

Table 4.3: Gantry, collimator and couch rotations for each beam in the used IMRT plan according to the TPS. LAO is beam 3

Beam number	Gantry angle (°)	Collimator Angle (°)	Couch angle (°)
Beam 1	157.0	5.0	0.0
Beam 2	107.5	3.2	1.0
Beam 3	82.9	5.0	6.4
Beam 4	0.0	0.0	0.0
Beam 5	308.0	355.0	0.0
Beam 6	255.0	357.0	0.0
Beam 7	203.0	0.0	0.0

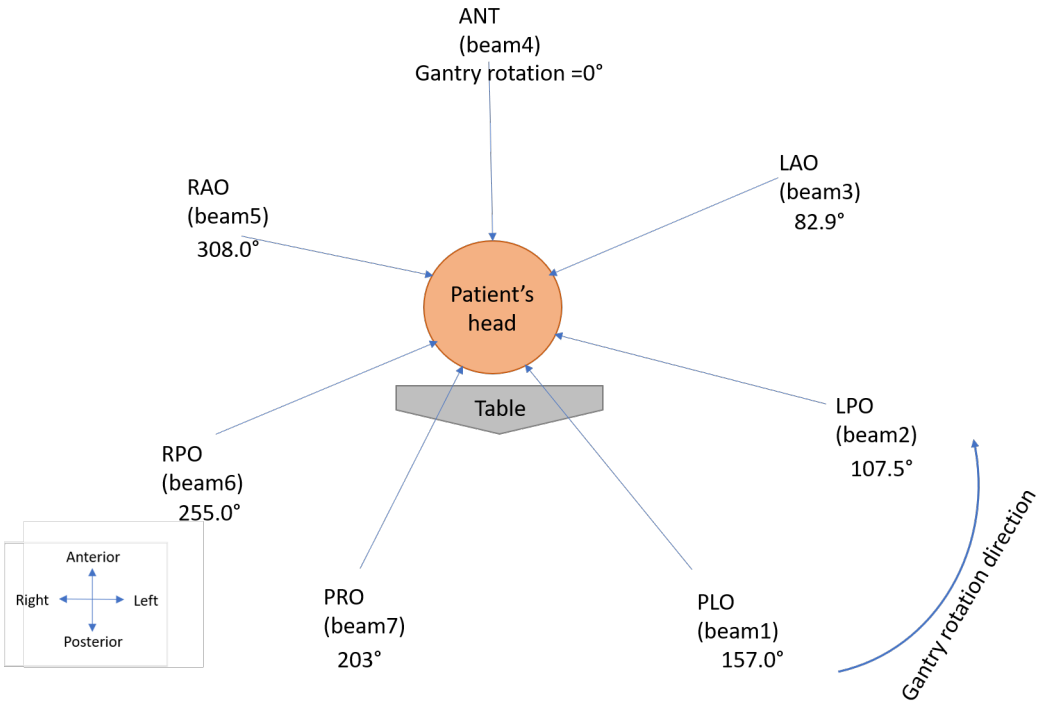

Figure 4.5: Beam directions in the IMRT plan received from UCLH.

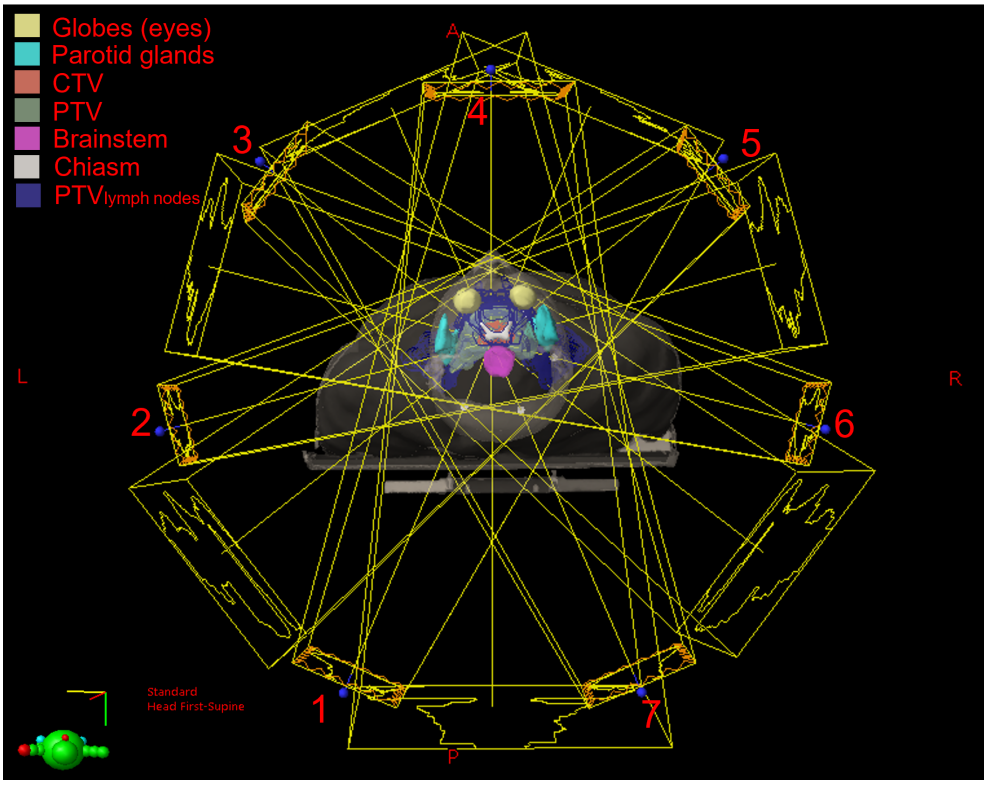

Figure 4.6: Beam directions in the IMRT plan received from UCLH as shown in the TPS. L: left, R: right, A: anterior, and P: posterior.

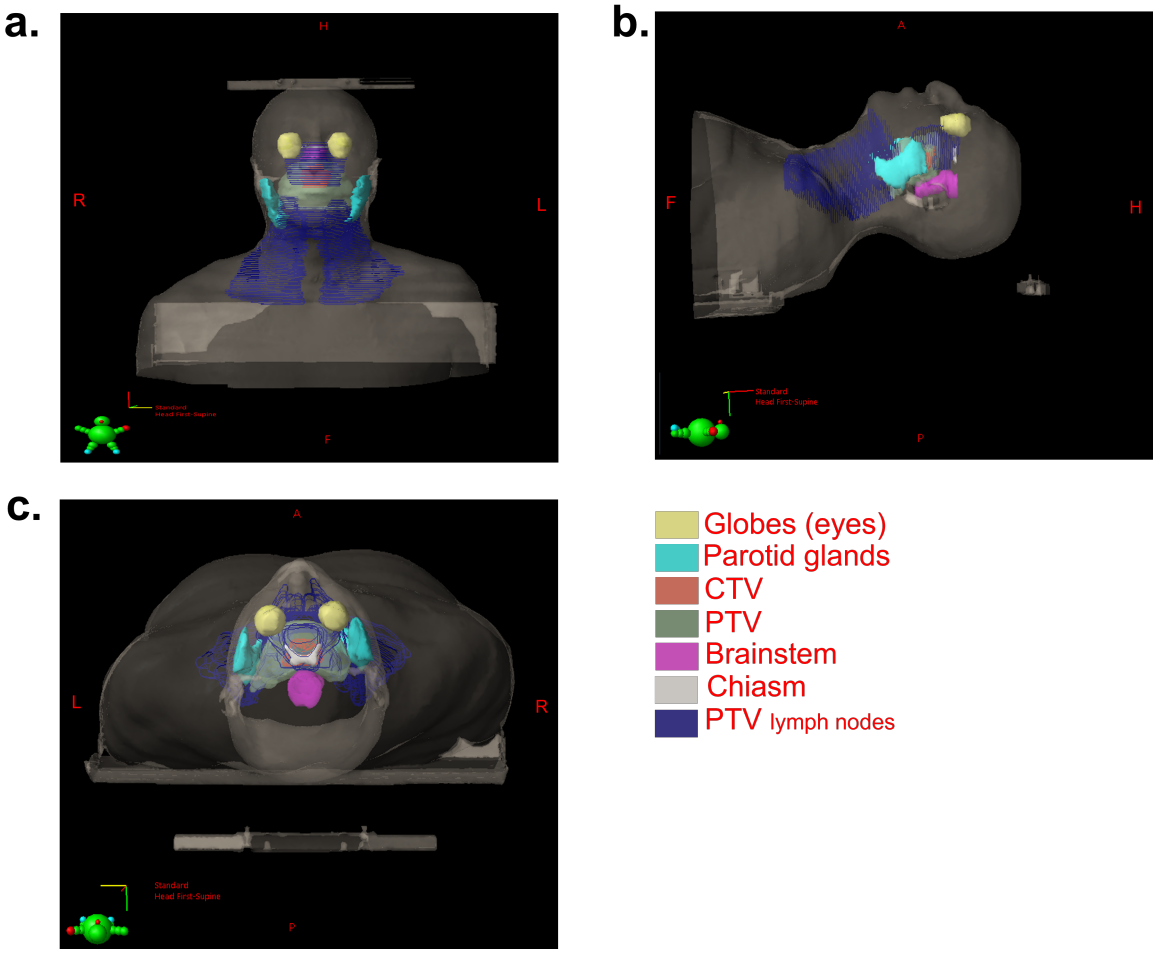

Figure 4.7: The tumour volumes and organs at risk **a.** coronal view **b.** sagittal view **c.** axial view. L: left, R: right, A: anterior, P: posterior, H:head, and F:feet.

For the radiation source, the DYNVMLC module (which represents the dynamic MLCs in Varian linac) was added to the linac built and calibrated as outlined in chapter 3. EPID can be used to study the performance of each beam [201]. In this study specifically, in order to save time and computer memory, beam three (left anterior oblique) was simulated as it passes the left parotid gland. The dose was normalised in order to reduce the statistical noise resulting from inter-sample variations in order to improve data integrity in terms of data accuracy and consistency [202]. The normalisation constant was the highest dose in the reference image, namely 6×10^{-16} Gy/particle. The beam was used as a shared library in order to irradiate the phantom. This source option requires the linac to be compiled as a shared library first, and

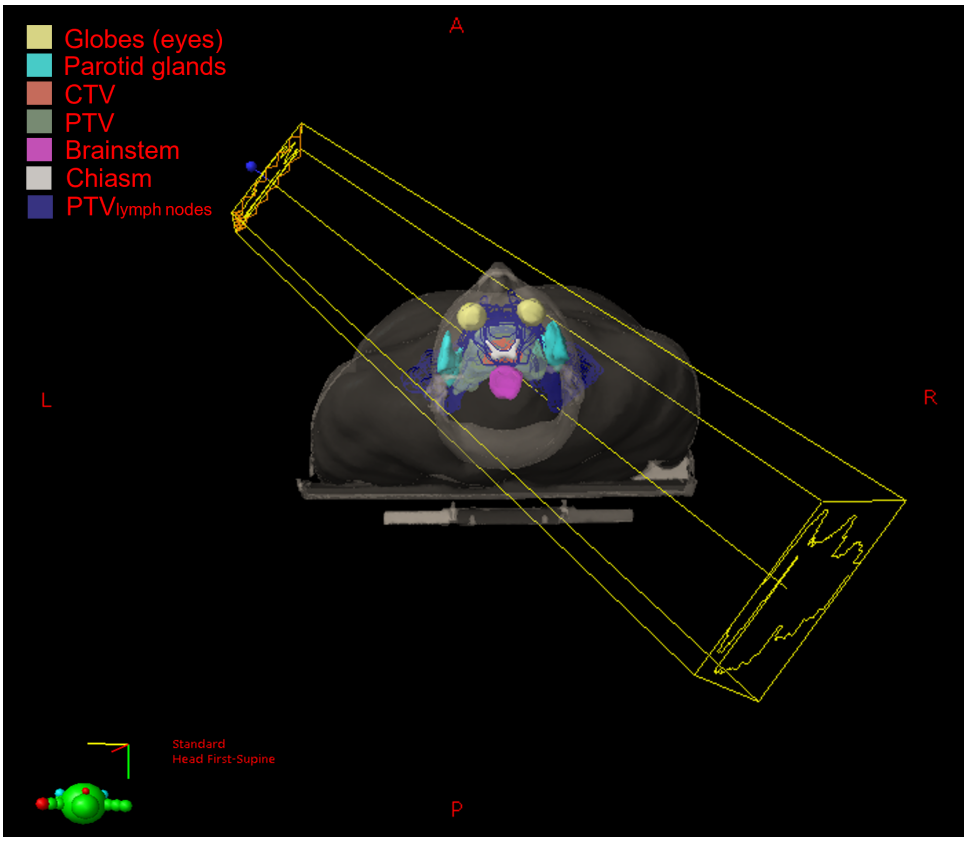

Figure 4.8: The LAO beam direction as shown in the TPS

then subsequently loaded dynamically into memory when the dose calculation is started. This allows both simulations (the beam simulation and dose calculation) to begin executing simultaneously. The 4D PSF_{IAEA} was scored in the BEAMnrc coordinate system, on the exit from each phantom, for the next step.

For MC simulation setup and parameters, the number of particles required to achieve a statistically relevant MC simulation is significantly high. Given this, variance reduction techniques play a substantial role in these simulations. The bremsstrahlung splitting was applied uniformly, and with a splitting factor of 20 without Russian Roulette, in order to increase the number of photons [73]. The energy cut-offs were used for the electron (ECUT) and photon (PCUT) transports: these were 0.7 MeV and 0.01 MeV, respectively. These values were chosen in order to eliminate low energy photons and which would therefore be less likely to contribute to the final result. This will lead to faster

calculation and better efficiency. No extra range rejection was utilised in this simulation as there is a limited number of particles in the PSF_{IAEA}. The HOWFARLESS algorithm was turned off since the phantom is based on a real patient: as such, it is considered inhomogeneous. The material surrounding the phantom is air, used in order to mimic the real case scenario. Each of these parameters were selected either based on literature guidance, or the egsnrc manual where they were suggested as a means to provide better results [73, 77, 203].

- **Obtaining the EPID response:**

  By scoring the 4D PSF_{IAEA} on particle exit from the phantom, the EPID dose calculation becomes straightforward [204]. Each model was irradiated by each previously generated 4D PSF_{IAEA} using 2×10^9 incident particles. The model response was extracted from d_{max} for the water model, and from the Gadox layer for the 17-slab model. Figure 4.9 shows the flowchart of the work process implemented in order to obtain the model response. Figure 4.10 shows the two main parts of the simulation.

  For MC simulation setup and parameters of EPID calculation, the bremsstrahlung splitting, splitting factor, ECUT, and PCUT were the same as for the IMRT simulation. However, the HOWFARLESS algorithm was employed for the water-slab model only which implies that it was turned off for Gadox-based PIDs since they are not considered homogeneous phantoms as with the water-slab model. The EPID was surrounded by air.

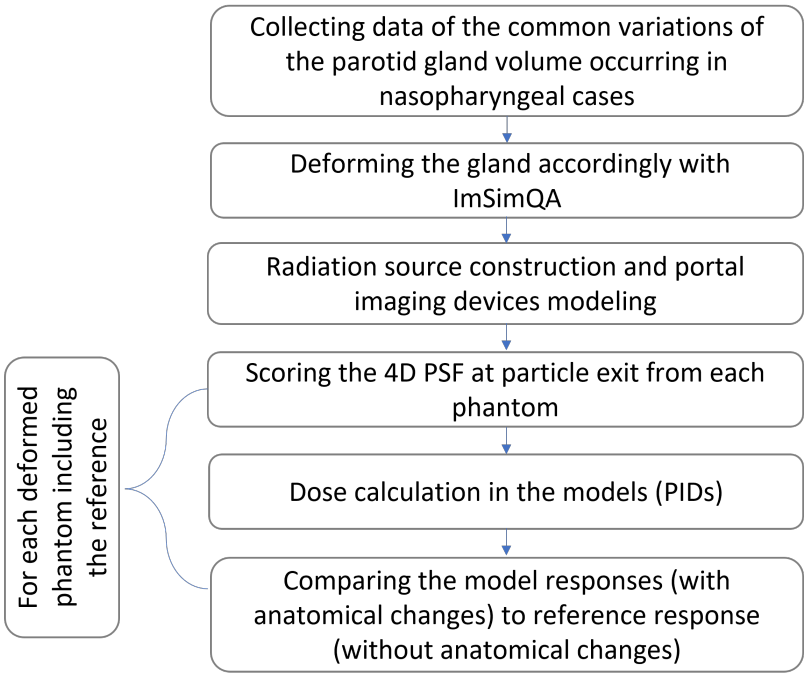

Figure 4.9: Flowchart exhibiting the functionality of the work process for EPID response scoring.

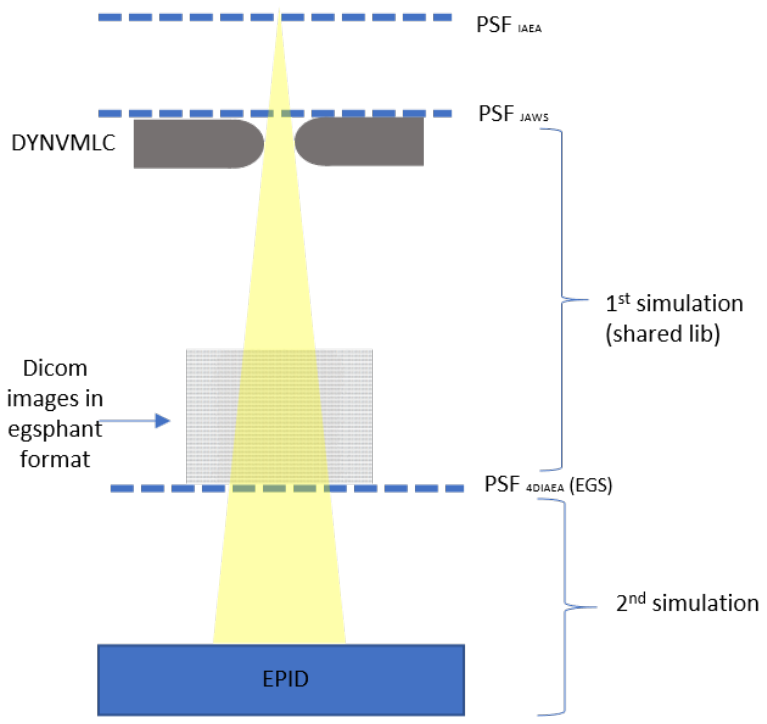

Figure 4.10: The two main parts of the simulation, DYNCMLC is the Varian dynamic MLCs.

4.4.4 The Evaluation methods

- **2D gamma analysis with gamma angle**

  The gamma analysis was applied in order to assess whether a difference can be seen between the simulations with anatomical changes (i.e., the evaluated image) and without changes (i.e., the reference image). As a reminder, these images were taken from the Gadox layer for 5-slab and 17-slab models, and from the d_{max} for water model. Various criteria have been selected 1%/ 1 mm, 2%/ 1 mm and 2%/ 2 mm for the models assessment. These various gamma criteria were chosen because the gamma analysis sensitivity decreases dramatically with loose criteria [205]. Furthermore, it is recommended by [85] to use tight gamma criteria in order to detect small errors and, in this research, there are subtle regional modifications in the gland volume which can easily be missed by deploying a too broad criteria. The gamma angle indicates which parameter has a higher impact on the gamma value. The gamma angle will be between 0 and $\pi/2$ if it is dominated by the dose difference; however, it will be between $\pi/4$ and $\pi/2$ if the distance to agreement (DTA) has the higher influence on the gamma value [86].

  The action threshold for the gamma index (reference level of gamma passing rate) is defined at 95%, in other words, the pass rate of more than 95% of the dose points in the phantom should have a gamma value smaller than 1, (i.e., $(\gamma\% < 1) \geq 95\%$) [206]. This protocol is designed to ensure uniform dose distribution to the target volume and to protect the surrounding normal tissues as well as take other errors (such as tumour shrinkage) into consideration. Such a protocol can result in successful tumour control and minimal complication rates (see Figure 3.4). For this study, the voxels ($< 1 \times 10^{-16}$ Gy/incident particle) were excluded when computing the results. This value was selected since it is the highest value found in the background.

- **Sensitivity index (the standardised mean difference)**

  The sensitivity index (d') expresses the respondent's sensitivity to the change

in signal due to the change in the gland volume, and it therefore represents the signal-to-noise ratio of the measured difference. Contrary to the gamma index, the sensitivity index includes a noise component represented by standard deviation, thereby leading to more realistic sampling since it may include various noises. It is useful to evaluate the probability that an anatomical change be detected. In this study, it was calculated by comparing the standardised difference between the means of signal to the averaged uncertainty of two images [179]. This was done according to equation (4.1):

$$d' = \frac{|S_{ref} - S_{def}|}{\sqrt{\frac{1}{2}(\sigma_{ref}^2 + \sigma_{def}^2)}} \tag{4.1}$$

Where S_{ref} is the pixel signal in the reference image, and S_{def} is the pixel signal in the evaluated image of a deformed phantom. σ_{ref}^2 and σ_{def}^2 denote the squared uncertainty of the pixels in the reference and evaluated images, respectively. The d' assumes that σ_{ref}^2 and σ_{def}^2 are equal in contributions and uncorrelated. The sensitivity index is dimensionless, and a higher index indicates that the difference can be readily detected.

4.5 Results and discussions

4.5.1 PIDs detection ability

All models expressed a similar detection ability with a mean difference around 0.2%. The statistical uncertainty was below 1% in the simulations: the water model has the lowest uncertainty thanks to its structure, and it directly records the dose in water [180], unlike Gadox-based detectors where the dose is proportional to deposited energy, but has oversensitivity to low energy as reported in [207–211]. The passing rates of gamma evaluation for the water model and 5-slab were lower than the suggested gamma level at -28.5% volume loss of the parotid gland. However, the 17-slab model had a pass rate less than 95% at -26.3% of the gland shrinkage (see Figure 4.11, a). The gamma passing rates (GPRs) were 95.85%, 95.65%, and

94.76% for water, 5-slab and 17-slab, respectively. Latterly, these rates were observed at 26.3% volume reduction using 1%/ 1 mm gamma criteria. The models were able to report the common volume loss which is from -37% to -46.9% for the parotid gland. The values of the gamma angle were between $\pi/4$ and $\pi/2$, thereby implying that the gamma index is primarily dominated by the DTA criteria. This implies, although the soft tissue is not clearly shown in EPID images as much as that of kV-based detectors [121], it is able to detect the dose discrepancy raised from non-rigid anatomy (soft tissue) changes.

There is no international standard, or indeed limit, for volume loss during radiotherapy and at which point the ART becomes necessary. This decision mainly relies upon the practised protocol in the given hospital. For parotid glands, one study suggested, based on CBCT images, to consider re-planning when the volume was reduced by 24–30%, which is more likely to occur in the third week of treatment [108]. The model in this study suggested re-planning at a volume loss of 26% which is within the previously recommended range (i.e., 24–30%). As radiation also has an effect on different parts of the human anatomy including the tumour itself, the tumour volume change must be counted also since it will increase the discrepancy between the delivered dose and planned dose. The tumour shrinkage rate in nasopharyngeal cancer was found to be 0.23% per day, with an average range of 0.02%–0.8% [212]. However, this range varies as the tumour radio-responsiveness varies from patient to patient. Younger patients ($\leq$ 47 years old) tend to have high tumour volume loss in contrast to older patients ($>$ 47 years old) [213, 214]. Moreover, given that the majority of head and neck cancers are treated by IMRT or volumetric modulated arc therapy (VMAT), these two techniques tend to induce discordance in dose distributions between the intended dose (calculated in the treatment planning system) and the real dose delivered to a patient during treatment. Despite this, they generate clinically superior treatment plans than the traditional planning technique, namely three dimensional (3D) conformal radiation therapy [215–217]. This discordance in dose distributions is a result of using larger amounts of monitor units than the traditional radiotherapy technique, in addition to producing a steep

dose falloff between the tumour (target) volume and nearby normal tissue, marked as organs at risk (OARs) [218]. Thus, this shortcoming may lead to increasing the dose discrepancy fund in the results in graph (a) of Figure 4.11.

The GPRs with various criteria were plotted as a function of the parotid volume change for the 17-slab model (see Figure 4.11, b). As tolerance levels increased, the gamma passing rates increased. This should be taken into account when using gamma analysis in clinics, and the criteria should be carefully established in order to quantify errors, whether they are small or large.

The sensitivity index of each model was calculated using equation (4.1). As was anticipated, the discrepancy detection capability of three models increased as the gland volume reduced (see Figure 4.11, c). In order to quantify the model's ability as an error detector, Rose's criterion is introduced. It states that a signal to noise ratio above factor five is required to definitively differentiate the image features [219]. The sensitivity index is the relationship of the mean (signal) to standard deviation (noise) as equation (4.1) demonstrates. Hence, this represents a simple and straightforward method to indicate the SNR. According to Rose's criterion, and based on the sensitivity index, all models are able to clearly discriminate the changes at 60% volume change in the gland with a detection rate of 82% for 17-slab EPID, 79% for 5-slab, and 78% for water modelling at a 95% gamma reference level. The certainty of detection reaches 100% when the changes are larger than 60%. The overall detection ability for 17-slab, 5-slab, and water models are 65%, 63%, and 59%, respectively. This is for the averaged parotid gland changes.

The gamma maps of the 17-slab geometry are displayed in Figure 4.12 for each respective volume change of the gland. These images were extracted from the Gadox layer, and the pixels outside the beam were set to zero. The parotid gland dose deviation noticeably begun at -26.3%, and gradually increased until a volume loss of 72% was observed. This emphasises the recommendation in [85] of using tight gamma criteria when detecting small changes. This means the gland became close to the high dose, thereby leading to an increase in the parotid gland mean

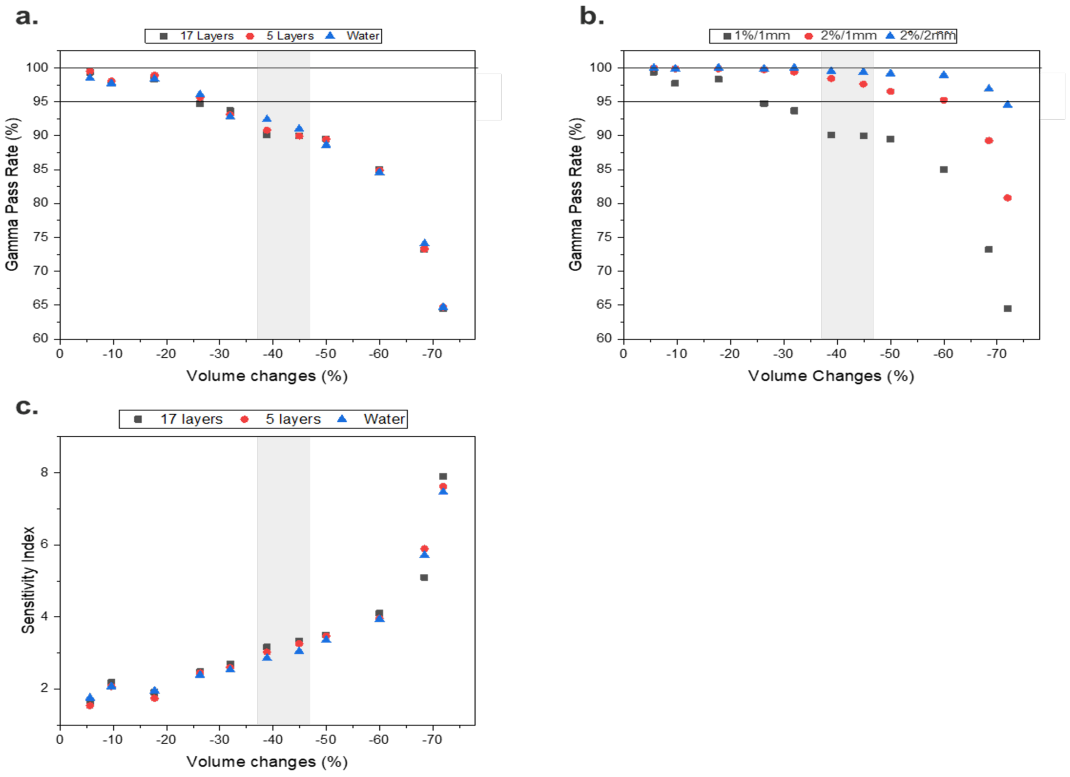

Figure 4.11: The results of **a.** the GPR of three models **b.** the GPR for 17-slab model using various gamma criteria **c.** the sensitivity index. The shadowed area is the common volume change of the parotid gland during the treatment (between-37% and -46.9%).

dose [220]. Moreover, it began to effect the dose in PTV (i.e., the area underneath the gland) at -26.3% volume loss with a gradual increase. Thus, re-planning at this level can save the gland from post radiation side effects, and furthermore ensure a dose distribution as planned for a specified tumour volume. Any volume change of less than -26% indicates that ART is likely to be unnecessary.

EPID detection ability may be reduced due to noise. In some commercially available EPIDs, there is a support arm located underneath the photodiodes: this causes back-scattering which, in turn, contributes 6% of the image signal. This has a visible impact on the large field sizes and could, therefore, reduce error detection visibility [221]. This effect of back- scattering was not deliberated in this study's investigation models. The MLC transmission (namely, 30% of the EPID response) was, however, involved in the calculation [221].

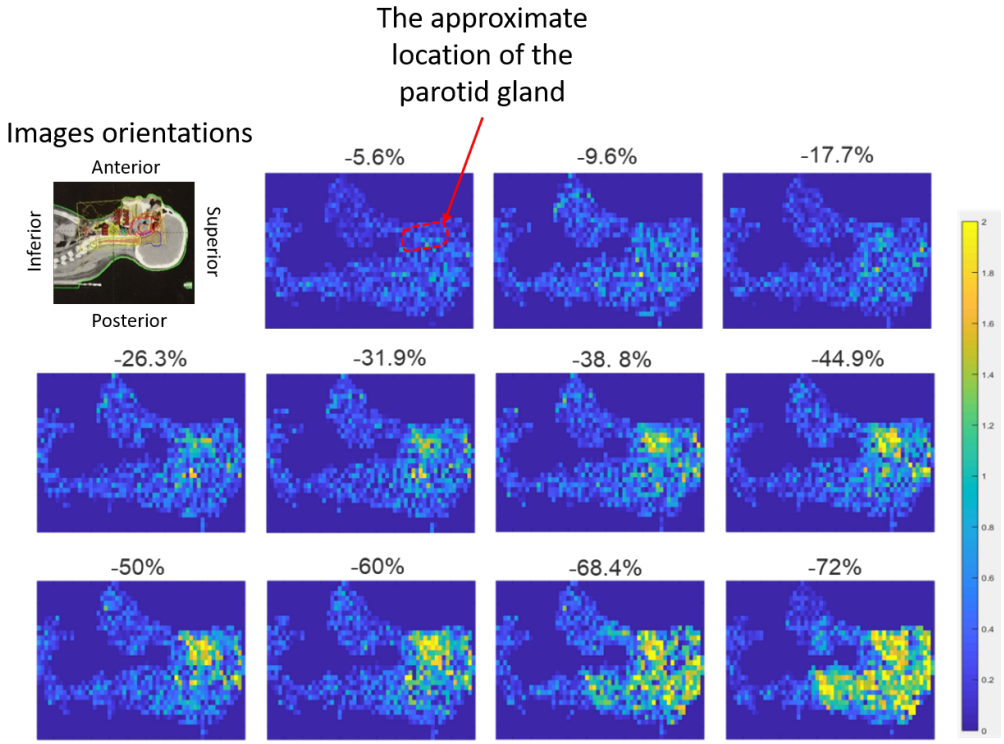

Figure 4.12: The gamma maps for each volume reduction, indicated by percentage above each image, of the parotid gland at the detector level of a single beam IMRT in nasopharyngeal carcinoma. The dose bar, on right, indicates the normalised dose.

The damage in the pixels within clinical EPID due to radiation exposure leads to an unstable response on the image. Such damage cannot be simulated. Nevertheless, the pixel sensitivity variation effect might be mitigated by two methods. The first is done by applying a flat field (FF) correction to the clinical EPID image which is an essential commissioning step; the second is to introduce variation in the MC images [81, 222, 223]. Furthermore, the accumulation of the dark current within pixels exhibits increased noise in the image. The dark subtraction, another essential commissioning step, diminishes this type of noise, reducing up to 99.7% of the dark current, thereby implying that only 0.03% remains in the image [157, 224]. As a result, these noise sources will have a minute impact on the EPID detection ability.

This computational model of EPID will open doors to set a volume loss limit for human anatomy during radiotherapy. Where beyond this limit, ART becomes necessary in order to achieve successful treatment and improve patients' quality of

life. Moreover, it can study EPID sensitivity in order to detect dose discrepancy or errors in other cases. For example, tumour regression in lung cancer cases where it has demonstrated its ability as in vivo dosimeter that can be used to detect the dose differences between the delivered and planned doses. This is performed on a simple phantom consisting of water and air using the MC simulation [225, 226]. As such, this can decrease the margin around tumours and therefore see less dose being inadvertently transferred to healthy surrounding tissue [226].

4.5.2 Simulation Time

The central processing unit (CPU) time requirement for 2×10^9 incident particles was examined for three geometries. The results are shown in Figure 4.13. Obviously, generating the 4D PSF_{IAEA} requires the longest time for all models; on the other hand, acquiring the model response varies from one to the other. The water model was the fastest, whilst the other models were about 480% longer. The water response simulation requires 5 hours whilst the other two need 29 hours (a marked difference).

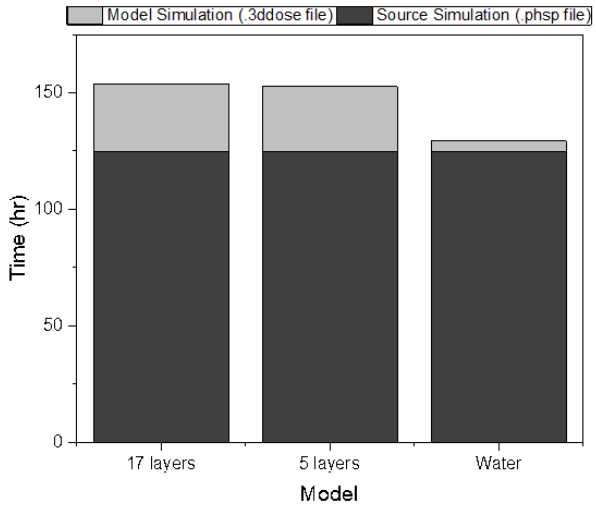

Figure 4.13: CPU time required for three different configurations whilst obtaining the 4D PSF_{IAEA} and scoring the model response.

4.6 Conclusions

The primary goal of this project has been to inspect and test the portal imaging devices and investigate their clinical abilities in terms of anatomical changes detection, specifically parotid shrinkage during radiotherapy treatment, via a computational method. This was achieved by calculating the energy deposit within the phosphor layer of the PID with and without changes. The anatomical changes were simulated using ImSimQA software.

In summary, based on the literature examined, the parotid glands tend to shrink and affect the dose distribution during the treatment, with a common volume loss of 37– 46.9% to a maximum recorded volume loss of 84%. Three models presented an equivalent detection ability, with a mean difference around 0.2%. The sensitivity index rose from 2 to 8 when the changes were substantial, with slight differences between the models. However, in many cases, the water-slab recorded relatively less sensitivity than Gadox-based PIDs: this is owing to the fact that Gadox has a high sensitivity to low energy photons.

According to gamma analysis, the passing rates of gamma evaluation for water and 5-slab models were lower than the suggested gamma level (95%) at -28.5%, whereas the 17-slab model had a pass rate less than 95% at -26.3% of the gland shrinkage. Latterly, this is most likely to happen during the third week of the treatment. This implies that the 5-slab model does not respond in exactly the same minor as the 17-slab one given that they have slightly different outcome responses overall.

The computational study demonstrated that the utility of EPID (when used for monitoring anatomical changes of the parotid gland during the radiation treatment) lends to support the claim that EPID can be used for dose verification via quantitative dose mapping. This is because it is sensitive to dose differences arising from soft tissue discrepancy, and not only for position verification. The hypothesis of using a simple EPID structure as a replacement for the complex EPID structure (specifically, in the computational studies for fast simulation and better efficiency)

is supported as the differences between the models were less than 0.2%.

Chapter 5

MC system applications- The role of EPID in detecting maxillary sinusitis impact on dose distribution, and the main limiting factors for EPID applications

5.1 Overview of chapter

Heterogeneous maxillary sinuses (the medical term is sinusitis) are a side effect of radiotherapy in nasopharyngeal cases. Here, the sinusitis may develop during the radiotherapy, and thus the sinus becomes full of fluid instead of air [100]. However, in other cases (as with maxillary sinus carcinoma), the sinusitis regresses during the treatment [227]. In both cases, these changes in the sinuses filling, from air to fluid and vice versa, can alter the radiation dose of tumour volume and OARs. The role of EPID was investigated in detecting sinusitis impact on dose distribution at the EPID level. In order to define the limiting factors for EPID application, the effect of anatomical overlapping with the tumour volume, in relation to the sensitivity

of EPID to dose discrepancy, has been discussed. Additionally, the impact of the evaluation tools on the application has also been examined. The dose difference is measured by comparing the EPID response (without the anatomical changes which represent its response in the first fraction) with its response in relation to changes via 2D and 3D gamma analysis. This was performed with a criterion of 1%/ 1 mm, and the gamma level was set at 95% in order to determine the gamma analysis influence on error detection using EPID. Since small field sizes are commonly used in IMRT plans, a relationship between the field size and the dose discrepancy due to these changes, was established in order to understand the impact volume of the dose difference for the field size.

5.2 Hypotheses of chapter

- The heterogeneous volumes caused by issues such as sinusitis may have a greater impact on small field sizes where it is commonly used in IMRT plans.
- EPID can report the dose discrepancy due to heterogeneous volumes caused by issues such as sinusitis and its effect on the dose distribution in tumour volume using IMRT beam.
- The evaluation tool plays an important role in EPID application efficiency.

5.3 Criteria of success

In a similar manner to chapter 4, the gamma analysis, sensitivity index, and percentage dose difference are applied in order to evaluate the performance of the simulated electronic portal imaging devices (EPID). More specifically, this is done in order to detect errors raised from anatomical changes such as sinusitis during radiotherapy for head and neck cancer patients. The gamma analysis provides a dose distribution comparison by combining both dose difference (DD) and distance to agreement (DTA) into a single quantity. The gamma analysis level is set to 95% [178]: consequently, dose differences between the reference and the evaluated images below this

level are not considered as a pass. The sensitivity index represents the relationship between the mean difference (signal) and the standard deviation (noise) difference of two distributions. A higher index indicates that error has a larger effect on dose distribution: as such, it can be more readily detected. The percentage dose difference is the percentage of the relative change between two doses in percentage terms. The acceptable difference is $\pm 5\%$, and any value beyond this range is considered as not passable.

5.4 Materials and methods

5.4.1 Phantom deformation

In general, the human head consists of various tissues and cavities: therefore, it is a heterogeneous area. From the perspective of radiation dosimetry, this inhomogeneity has an impact on dose distribution in terms of increasing the uncertainty when calculating the absorbed dose in a treatment planning system [228]. Any change in the tissue texture, like that which occurs with sinusitis where the sinuses are filled with fluid instead of air, may cause incorrect target coverage since each tissue has different physical and radiological properties [229]. Sinusitis can be a side effect of radiotherapy for nasopharyngeal carcinoma patients [230], or it can be diminished by radiation in some cases if the patient had this condition before treatment (i.e., as in the case of maxillary sinus carcinoma) [100]. To increase the therapeutic benefit of radiotherapy, it is crucial to take such a change in the content into consideration and consider re-planning if necessary.

For the purposes of this study, a retrospective IMRT case of nasopharyngeal carcinoma was used. The key parameters of this IMRT plan are listed in Table 4.2. The ultimate purpose thereof was to evaluate EPID ability in order to estimate the influence of sinusitis on the dose distribution of the area of interest (in this case the radiation field) at the EPID level by replacing the air in the sinus cavity with the fluid. The deformation was made by reading the DICOM files through MATLAB,

then selecting the slices containing the maxillary sinus. Afterwards, the pixel values were copied and transferred to the Excel file and the Hounsfield unit of air was manually modified to fluid. This process was repeated for all slices.

In the end, different real patient-based phantoms were produced. For the purposes of this experiment, we will consider two scenarios. These are: the deformed phantoms b and c (see Figure 5.1) and they will be named scenario (b) and scenario (c) in order to represent the half-filled sinusitis and fully filled sinusitis, respectively. They are benchmarked to the reference model (original phantom (a)) which is named scenario (a). The phantoms were converted to a specific format using the CTCREATE tool distributed with EGSnrc software so as to be compatible with BEAMnrc user code. The phantom voxel dimensions were chosen to be 0.25 cm $\times$ 0.25 cm $\times$ 0.25 cm in order to reach a compromise between resolution, simulation speed, and statistical uncertainty. The patient boundaries, PTV location, and maxillary sinuses were defined on the new phantom by using following equation (5.1):

$$P_{sim} = \frac{P_{ct}}{length_{ct}} \times length_{sim} \tag{5.1}$$

Where P_{sim} is the new pixel position on the y axis of the new image of the phantom created by CTCREATE, in cm. P_{ct} is the pixel position on the y axis on the CT image, in cm. $Length_{ct}$ is the CT image y axis length and $length_{sim}$ is the new image y axis length, in cm. The position on the y axis was calculated because the PDD was extracted from the y axis of the axial CT image. The same equation can be used in order to find the new pixel position on the x axis also.

5.4.2 Radiation source and radiation detector

The source mentioned in section 3.4.1 was used. Three different field sizes were created: 3 cm $\times$ 3 cm, 5 cm $\times$ 5 cm, and 10 cm $\times$ 10 cm. These were used in order to study the relationship between the field size and dose discrepancy.

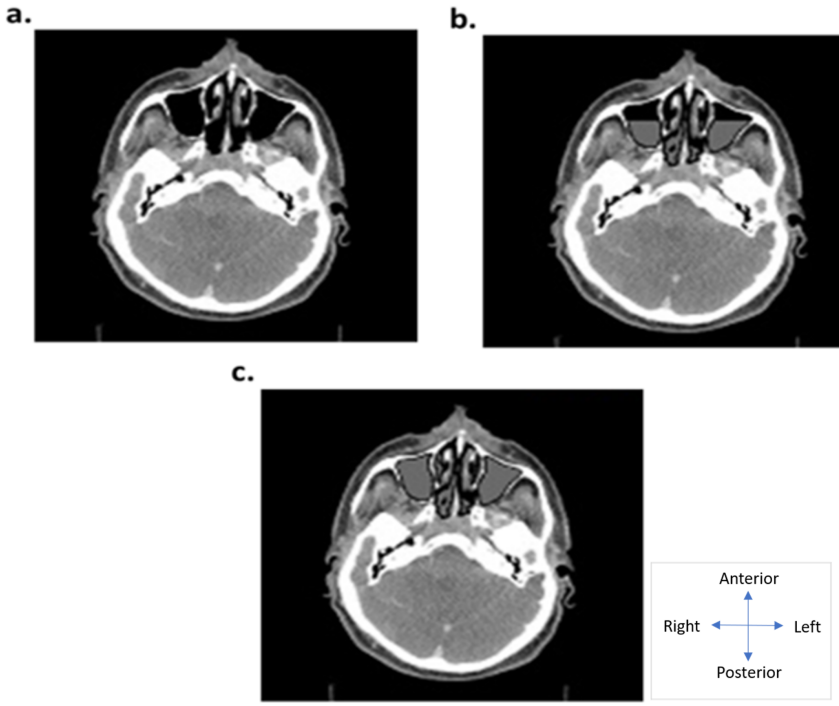

Figure 5.1: Different scenarios of sinusitis **a.** the original CT **b.** modified phantom (half fluid-filled sinuses) referred to as scenario (b), **c.** modified phantom (fully fluid-filled sinuses) referred to it as scenario (c).

The radiation detector is the 17-slab model that was previously mentioned and used in chapter 4, and here it represents the clinical EPID. More details about the structure can be found in chapter 4, section 4.4.1.

5.4.3 IMRT beam simulation and EPID scoring (dose calculation)

The same retrospective case of nasopharyngeal cancer used in chapter 4 was used here. According to the aims of this experiment, the anterior beam (beam 4 in Figure 4.5) was simulated in order to ensure that the beam went through the maxillary sinuses (see Figures 5.2 and 5.3). The dose was normalised in order to reduce the statistical noise resulting from inter-sample variations and to improve data integrity in terms of data accuracy and consistency [202]. The normalisation constant was the highest dose in the reference image, namely 6×10^{-15} Gy/particle. For EPID scoring, the same steps mentioned previously in chapter 4, section 4.4.3 were fol-

lowed.

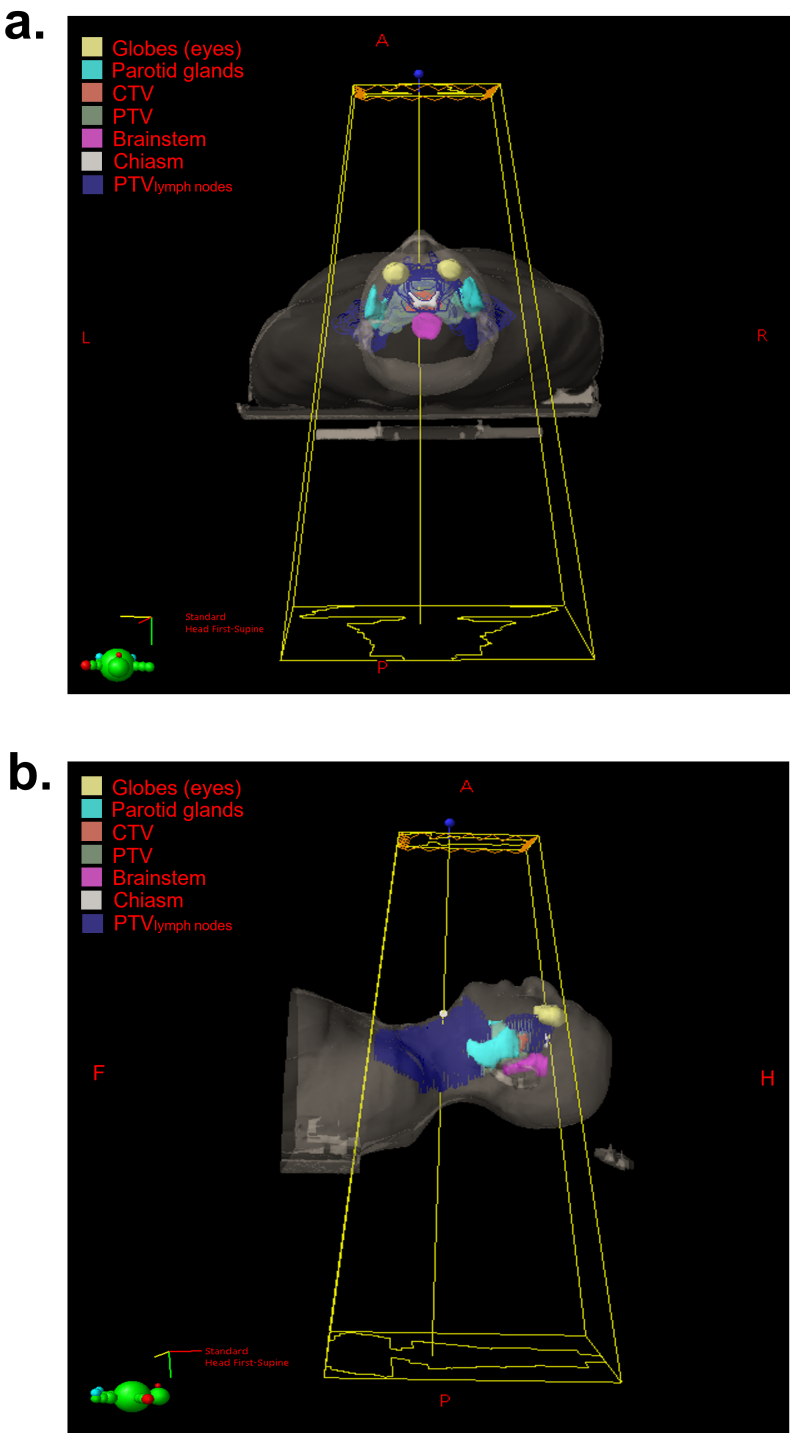

Figure 5.2: The anterior beam direction, as shown in the TPS, regarding the PTV, CTV, and OARs; **a.** axial view **b.** sagittal (lateral) view

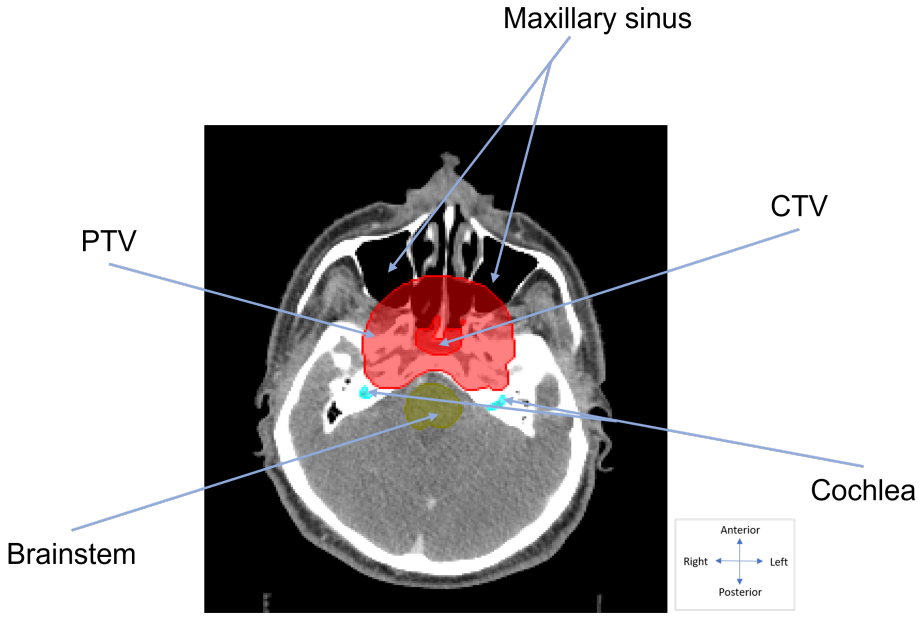

Figure 5.3: The maxillary sinus location to the CTV, PTV, and OARs.

5.4.4 Evaluation tools

- Percentage depth dose curve (PDD)

  PDD is one practical tool that can be used to study the dose distribution within the patient on the central axis (i.e., z axis beam). There are main regions constituting the typical PDD of the radiation beam in a water phantom. The beam passes the surface of the phantom, where it deposits a surface dose lower than the d_{max}. Underneath the surface, the dose increases quickly to reach a maximum value at depth (d_{max}), and thereafter it exponentially decreases until it reaches a certain value at the exit point from the phantom [66]. More details about the PDD can be found in chapter 1, section 1.4. The PDD within the patient is the same as described for the water phantom, however, the natural heterogeneity of the human body decreases the smoothness of the PDD curve [231].

- Percentage dose difference

  The dose percentage difference is the percentage of the relative change (difference) between two doses in percentage terms. It was calculated using the following equation (5.2) [232]:

$$Diff(\%) = \frac{x - x_{reference}}{x_{reference}} \times 100 \tag{5.2}$$

Where Diff is the percentage dose difference (%), x is the dose of a phantom with change (sinusitis) in Gy/particle, and $x_{reference}$ is the reference dose of a phantom without change in Gy/particle. In this case, x and $x_{reference}$ are particularly unitless (i.e., no unit) given that the dose has been normalised.

- Gamma analysis

  The 2D and 3D gamma analysis were applied as evaluation tools. The EPID response of the modified phantom (with changes (evaluated image)) was compared to the EPID response of the original phantom (without changes (reference image)). A software environment available online (the 'computational environment for radiotherapy research (CERR)') was used for 3D gamma analysis [233]. The gamma analysis criterion was 1%/ 1 mm, and the gamma level was at 95% (see Figure 3.4) for both 2D and 3D gamma analysis.

- Sensitivity index

  The sensitivity index of the EPID response was calculated according to equation (4.1), as mentioned in chapter 4, section 4.4.4.

5.5 Results and discussions

Firstly, the dose discrepancy and the connection between the discrepancy and field size were evaluated inside the patient. Secondly, EPID's ability to report the discrepancy was assessed for each field size. Finally, an IMRT plan was simulated in order to replicate a clinical scenario and to therefore evaluate the evaluation tool's influence on the error detection in tumour volume. The uncertainty of each simulation was less than 1%.

5.5.1 The relationship between the field size and the dose discrepancy due to heterogeneity

- *Reporting dose difference within the patient at different jaw openings*

  The PDD can be used to report the presence of dose differences owing to inhomogeneity. Inhomogeneity is always a concern, and its effect on the dose was investigated within a water phantom, or an animal (e.g., a dog) such as has been studied by [234–236]. In this study, a phantom based on real patient data was used in order to investigate EPID's ability to report errors arising from sinusitis. Similar to the outcomes of the previously mentioned studies [234–236], it is found that aeration changes (e.g., sinusitis during the radiotherapy treatment) led to the dose alteration at the patient level (see Figure 5.4). This step was considered in order to investigate the impact of sinusitis within the patient on the PTV (tumour volume), and which is represented by the yellow shaded area in Figure 5.4, and defined by using equation (5.1).

  The dose difference threshold is defined as the minimum dose difference (error) considered in the analysis [237]. It was stated in [238] that a dose variation of $\pm$ 10% in IMRT from the real dose is an accepted norm in many clinical practices. However, it is recommended to use a threshold of less than $\pm$ 3% difference by [239]. In this study the 95% reference level has been established for error threshold, therefore, errors within $\pm$ 5% are counted as minimal and negligible. This range has been set to avoid undesirable consequences accompanying radiation treatment, and to ensure that radiotherapy has been applied as accurately as reasonably achievable without being unacceptably loose or strict [240].

  Figure 5.4 was translated into numbers in Table 5.1 which lists the dose differences using percentile change between the normal and the deformed phantoms. The PTV in this patient is overlapped with the maxillary sinus, and for this reason, the PTV dose difference was divided into two areas, namely dose difference during sinusitis and after sinusitis. The average difference at the

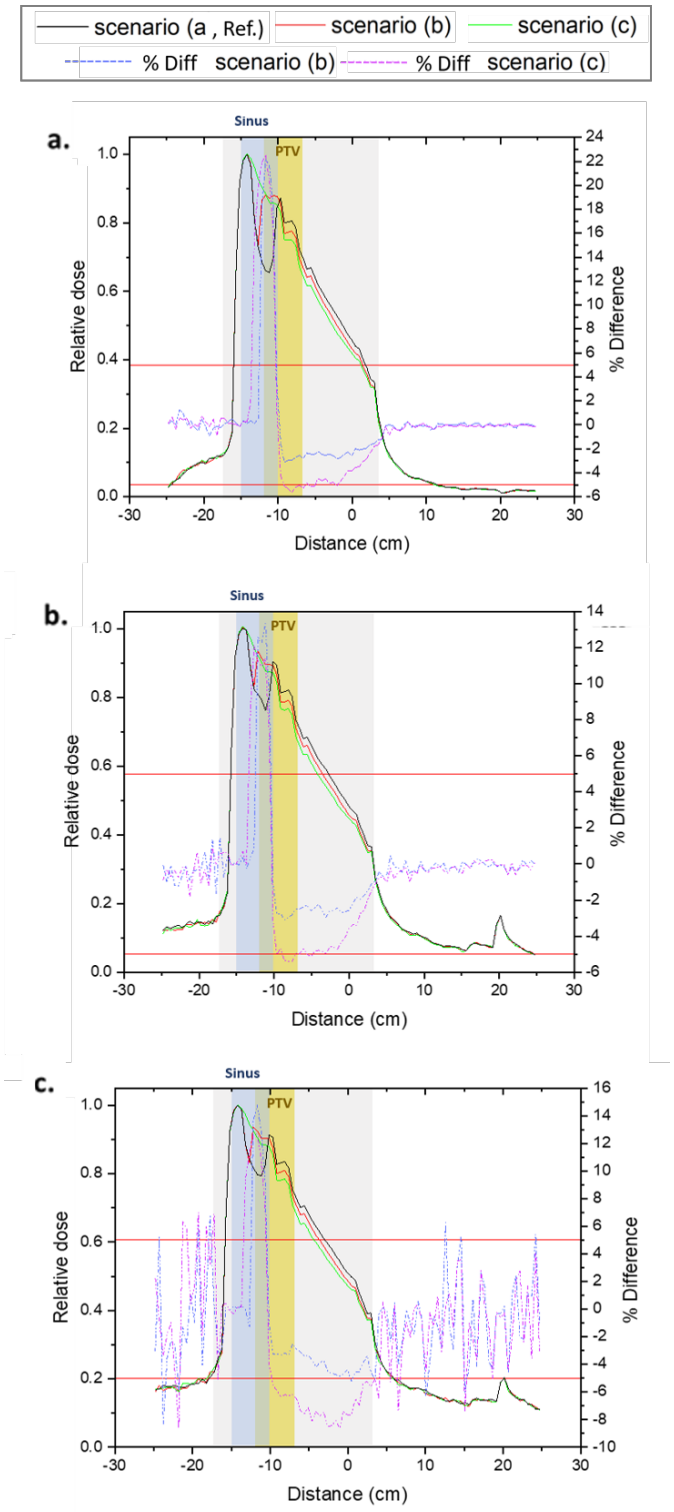

Figure 5.4: The PDDs within the patient (from -17 cm to 3 cm, the grey shaded area) for different scenarios at **a.** 3 cm x 3 cm, **b.** 5 cm x 5 cm and **c.** 10 cm x 10 cm. The blue shaded area from -15 cm to -10 cm is the sinuses, and the yellow shaded area from -12.5 cm to -7 cm is PTV.

PTV for both scenarios decreases by almost 50% at 5 cm $\times$ 5 cm and 10 cm $\times$ 10 cm compared to 3 cm $\times$ 3 cm in the area where the PTV is overlapped with sinusitis. The dose difference has a higher impact when the sinuses are fully filled with the fluid. However, this effect diminishes as the field size increases: for instance, scenario (c) different by +3%/-2.46%, +0.40%/-2.32% and +0.45%/-2.92% at sinusitis/after sinusitis areas relative to scenario (b) at 3 cm $\times$ 3 cm, 5 cm $\times$ 5 cm and 10 cm $\times$ 10 cm field sizes, respectively. The difference is larger at 10 cm $\times$ 10 cm than in the 5 cm $\times$ 5 cm filed size since the former has higher scatter contribution and the field size covers the maxillary sinuses on both sides of the nose (two maxillary sinuses). The dose difference in the PTV was exceeding the percentage difference threshold ($\pm$ 5%) at the sinusitis area for all field sizes and for both scenarios. However, it was below the threshold for scenario (b) (namely, the after sinusitis area for all field sizes) (see Table 5.1). A study undertaken by [241] reported the clinical outcomes of patients treated with IMRT for malignancies of the nasal cavity and paranasal sinuses. The outcomes were suboptimal in the long term: specifically, the patients complained of late complications. This can be due to ignoring the anatomical changes which have happened in the area during the treatment and which thereby led to poor disease control. In VMAT, it is reported that changes in maxillary sinuses have a minimal impact on dose distribution in tumour volume, and no dose differences in OARs volumes [227]. Despite this, such changes can highly impact upon the dose distribution in cases where a proton therapy beam is used [227].

For gamma passing rates (GPRs), the whole irradiated field is considered, and the values outside the beams are set to zero. The tolerance level was set to be equal or bigger than 95% ($\geq$ 95%), more details on this can be found in chapter 3, section 3.4.5. The difference between the two scenarios is not realised in PTV. The GPRs at EPID level are slightly lower when the sinus is fully filled. The effect of this change in the PTV is lightly pronounced in the small field, as can be observed by looking at the 3 cm $\times$ 3 cm field compared

to the 5 cm $\times$ 5 cm one. For the 10 cm $\times$ 10 cm field size, the GPR is the lowest because the field covers both sinuses, unlike the other two field sizes (see Table 5.1).

Table 5.1: The averaged dose difference and 2D GPRs at different field sizes for PTV and EPID

Field size (cm^2)			3x3		5x5		10x10	
Scenario			b	c	b	c	b	c
Dose difference (%)	PTV	at sinusitis	14.03	17.00	7.90	8.27	8.05	8.50
		after sinusitis	-2.64	-5.10	-2.82	-5.14	-3.14	-6.06
	EPID		-5.01	-7.61	-4.11	-7.33	-4.44	-6.64
2D GPRs (%)	PTV		94.50	94.50	96.90	96.90	92.60	92.50
	EPID		98.30	98.10	97.60	97.00	90.50	89.60

- *EPID ability to report dose discrepancy due to sinusitis*

  The PDD within the patient proved that heterogeneity of the sinuses can lead to dose disagreements. The question remains as to whether EPID has the ability to reflect the real effect and report these changes readily, and without limitations. For this reason, the dose difference and gamma passing rates were studied at the EPID level in order to quantify EPID sensitivity for heterogeneity detection and the anatomical overlapping influence. Table 5.1 and Figure 5.5 demonstrate the impact of heterogeneity of sinuses on the dose at the EPID level. The dose difference at the EPID level showed the differences between the two scenarios. Scenario (c) exceeded the threshold ($\pm$ 5%) at the three field sizes. By contrast, scenario (b) was either at the threshold, or barely below it for the three field sizes. Overall the dose difference reported at the EPID level is much lower than the actual difference observed in the PTV. It is beneficial to take these findings into account when using the small fields, as are commonly utilised in IMRT plans, in order to avoid late complications [241, 242]. Scenario (c), where the sinuses are fully filled with fluid, has lower gamma passing rates by approximately 0.20- 2% compared to scenario (b), where the sinuses are half-filled with fluid (see Table 5.1). Table 5.1 shows that the GPRs at the EPID level were lower than the threshold for

10 cm × 10 cm, that is when two maxillary sinuses were inside the field.

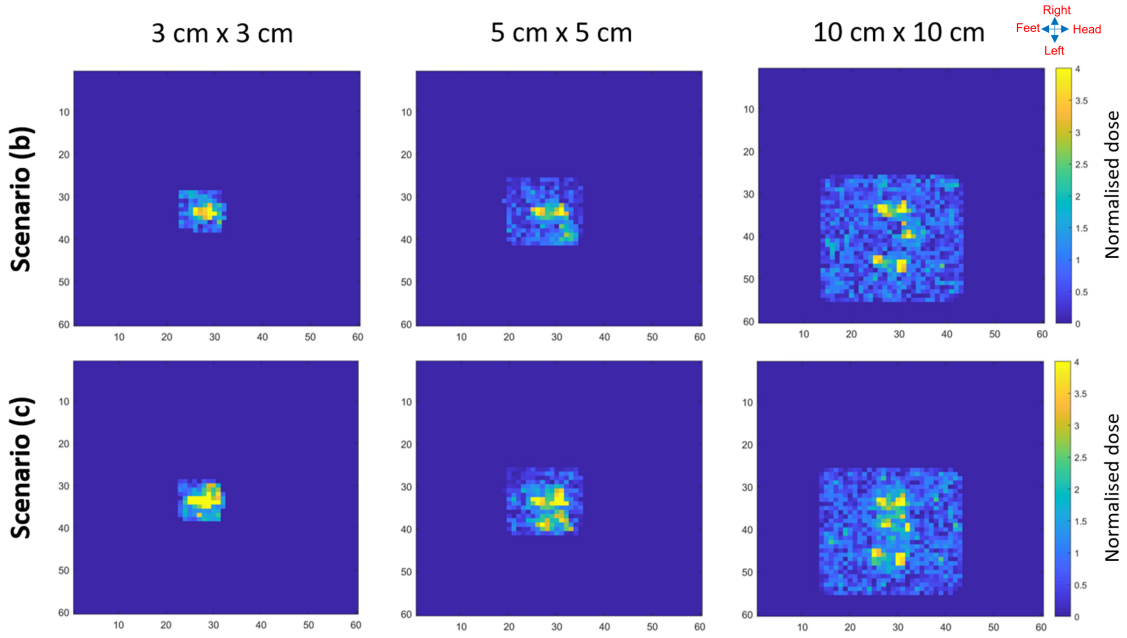

Figure 5.5: The 2D gamma map (60 pixels × 60 pixels) at EPID level for 3 cm × 3 cm, 5 cm × 5 cm and 10 cm × 10 cm for both scenarios. The first row represents scenario (b), and the second row represents scenario (c). The first column represents 3 cm × 3 cm, the second column represents 5 cm × 5 cm, and the third column represents 10 cm × 10 cm.

5.5.2 IMRT beam and main limiting factors for EPID applications

5.5.2.1 Gamma analysis impact on EPID

A single anterior IMRT field, crossing the sinuses to EPID, was simulated. In Figure 5.6, the gamma map reported dose differences in the maxillary sinuses area, but since it is overlapped with the tumour, it is difficult to visualise the impact on the dose of the tumour volume itself. This will be discussed further in section 5.5.2.2. Table 5.2 shows gamma passing rates (GPRs) of two different scenarios, using 2D and 3D gamma analysis. The 2D gamma analysis demonstrates a lower passing rate compared to 3D gamma analysis. This is despite using tight criteria (1%/ 1 mm) and a gamma level of 95%. In general, 2D gamma analysis tends to be more sensitive

to errors than 3D gamma analysis, as has been proved by [243] where 2D gamma analysis has been recommended in order to detect fine errors. With 95% gamma threshold at the EPID level, 2D GPRs indicate the necessity of re-planning, unlike 3D GPRs which were lower by 0.30%- 1% than the threshold. Carefully selecting gamma criteria is important, as was shown in chapter 4 (see Figure 4.11, b) and by [243].

The influence of such changes on dose distribution was found to be not major when using radiation (photon) therapy in contrast to proton therapy [227]. The effect can be reduced with continued efforts to obtain the best optimisation for parameters of the IMRT plan, and by combining the chemotherapy with radiotherapy [244]. Furthermore, providing a substantial time investment by oncologists in the target contouring process also plays an important role in IMRT success for head and neck cancer patients [244].

The sensitivity index (d') is the mean image signal to the square root of the standard deviation (noise) (see equation (4.1)). It is 2.25 and 2.47 at the EPID level for scenarios (b) and (c), respectively. Looking at Figure 4.11, c, the value of the EPID sensitivity index for sinusitis is similar to the EPID sensitivity index of parotid volume loss, specifically -50%. For Rose's criterion, the signal to noise ratio above factor five is required to differentiate the image features with certitude [219]. This indicates that the EPID performance ranks highly in terms of error detection arising from the heterogeneity within the maxillary sinuses during radiotherapy of head and neck cancer patients.

Table 5.2: GPRs for half (b) and full (c) filled sinuses using an IMRT beam

	PTV		EPID	
Scenario	b	c	b	c
2D GPRs(%)	87.40	86.70	84.10	81.57
3D GPRs(%)	97.00	96.90	94.70	94.00

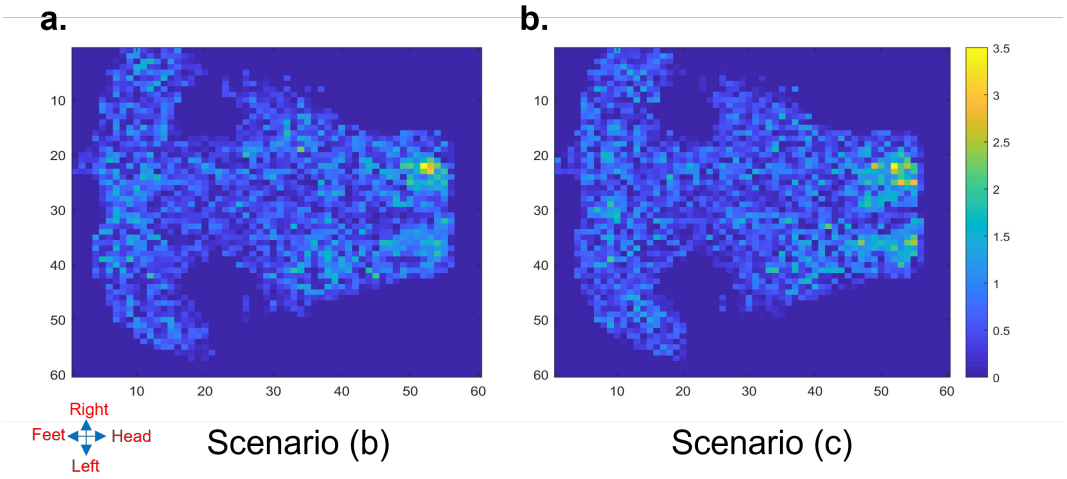

Figure 5.6: The gamma map (60 pixels × 60 pixels) of 2D gamma analysis for different scenarios using an IMRT beam at EPID level **a.** scenario (b) (half-filled sinusitis) and **b.** scenario (c) (full-filled sinusitis).

5.5.2.2 Anatomical superposition impact on EPID application

EPID is the common tool used for dose verification. This is thanks to its linear response to the radiation dose [131]. However, there are a few obstacles facing its implementation. The delivered dose that has three dimensions is compressed into the EPID dose map, namely into two dimensional images. Therefore, EPID can report the dose discrepancy but it cannot always define the impact of these errors on dose of tumour volume due to structural overlapping, as Figure 5.6 shows. It is not a simple matter to link between the variations in the dose map of the dose distribution obtained at the EPID level and dose distribution within the patient [131]. In Figure 5.6, the dose difference due to sinusitis is clearly noticeable, but this does not guarantee the dose discrepancy in tumour volume. Such a problem is observed when errors and tumour volumes are at one level (i.e., overlapped) as with sinusitis and nasopharyngeal carcinoma using a 0° beam gantry angle. However, this is not the case with the parotid gland and nasopharyngeal carcinoma as was seen in chapter 4 where the two structures were not exactly at the same level, and the beam was at a gantry angle of 82.9°. This limits the EPID dosimetry applications, and thus it is highly preferable to combine two methods to track errors. In another respect, the simple solution for 2D dose verification systems to overcome the anatomical

overlapping issues is acquiring EPID response for more than one beam in order to obtain different views, for example, anterior-posterior and lateral views.

5.5.3 Recommendations to gain maximum benefits from EPID applications

Several considerations must be taken into account in order to maximise the benefits of EPID application in clinics.

Firstly, an expert physicist is needed as dose verification is a part of the physicists' responsibilities according to the American Association of Physicists in Medicine (AAPM), report number 38 [245]. The expert physicist will evaluate the impact of errors on the plan. The question then arises that if the observed difference in dose distribution can be considered as a clinically unacceptable error (i.e., whereby the outcome of radiation treatment would be influenced by this dose shift in terms of local control or toxicity), should the plan be mandatorily adapted to these changes or not? Some errors have no major effect on the dose distribution, nor the surrounding normal structures (for instance, minor changes in the structure of maxillary sinuses due to inflammation in nasopharyngeal carcinoma cases using radiation therapy with VMAT technique) [19, 227]. Whilst others, such as tumour shrinkage, other surrounding organs shrinkage in the beam path, gases in rectum, bladder filling or weight loss, may lead to critical shifts in dose distribution for tumours or increases in the dose to normal tissues [246–248].

Secondly, combining two systems is highly recommended in order to accurately define the error sources and their influence on the dose distribution. In clinical practice, the adopted evaluation for the treatment operation must be effective and be able to reflect the real delivery status of the treatment as well as any mistakes or changes which occur during the treatment [249]. Hence, it is advised to use 2D and 3D dose comparisons since 2D dose comparisons may become restricted due to anatomical overlapping, whilst 3D dose verification provides dose information within a patient. It is found that 2D dose comparison tends sometimes to exagger-

ate the error impact whilst in the 3D dose verification, the passing rate is more likely to be higher compared to 2D dose verification. Latterly, this is due to the fact that the 3D dose verification evaluates the dose pixels in all points within the evaluated area thereby resulting in a relatively lower ratio of pixel numbers at which dose deviations occur relative to the total pixel number [249, 250]. For situations like that, an experienced medical physicist reviews these alerts. When the error is studied and understood, and the negative clinical consequences are estimated, the situation is debated with a radiation oncologist in order to decide a corrective action [131]. In a situation where it is not possible to combine two dose verification systems, it is recommended to acquire EPID from more than one beam and the frequent views are the anterior-posterior and lateral ones.

Thirdly, finding the optimal gamma dimensional analysis and gamma criteria is vital in addition to setting the gamma threshold wisely. It is very crucial to consider this as missing, or false errors may occur due to operational shortcomings arising from applying wrong criteria. Therefore, this will reduce the evaluation tool's accuracy and subsequent effectiveness for the treatment process (see Figure 4.11, b). The commonly used gamma criteria in clinics have been discussed widely, and it has been recommended to use tight or loose criteria based on the size of error with a view to upgrading the treatment process and establishing consistent and comparable criteria amongst institutions [85]. Furthermore, the differences between 2D and 3D gamma analysis must be considered: 3D gamma analysis tends to have higher passing rates by around 3% since it includes a larger number of pixels compared to 2D gamma analysis [251]. In this study, the passing rates of 3D gamma analysis were higher by 10% (see Table 5.2). A simulation system, like the one used in this study, can be an effective tool to evaluate the gamma criteria for common errors in radiation therapy.

5.6 MC portal imaging device vs the clinical EPID

Since EPID is integrated into linac, the dose verification became readily available. This improves the certainty of delivered dose evaluation [252]. The size of clinical EPID is approximately 20.48 cm $\times$ 20.48 cm, with a minimum pixel size of 0.2 mm and a matrix of 1024 $\times$ 1024 pixels [253]. The clinical EPID has a much finer pixel size than the MC portal imaging device used in this study (which has dimensions of 0.5 cm $\times$ 0.5 cm) and this was selected in order to obtain appropriate statistical certainty. This pixel size will lead to pixel averaging, a technique used to reduce noise: nevertheless, this definitely decreases the overall sensitivity given that averaging data within a pixel causes error fading and also lowers its impact. Therefore, it will be hard to detect [254]. The outcomes of my model estimate the real results in order to indicate the suitability of EPID for detection of anatomical changes during radiation therapy since it is predicted that EPID will be much more sensitive thanks to the fine pixel size it generates.

There are several reasons which account for preventing decreasing of the voxel size. These are:

- A limited number of photons and using PSF source;
- The inverse relationship between voxel size and uncertainty;
- Limited computer efficiency;
- Uncertain EPID structure.

5.7 Conclusions

In this project, the effect of aeration changes within the sinuses on the dose distribution was studied for head cancer cases in addition to the influence of anatomical superimposition and gamma analysis on the EPID ability to detect such changes. For this purpose, a method was invented in order to create different scenarios of the sinusitis, two of which were involved in this study. The relationship between the effect of sinusitis and field size was established using PDD comparison in the phantom, and it was found that the effect diminishes slightly as the field size increases. The average difference at the PTV for both scenarios decreases by almost 50% at 5 cm $\times$ 5 cm and 10 cm $\times$ 10 cm, compared to the 3 cm $\times$ 3 cm in the area wherein the PTV is overlapped with sinusitis. This supports the claim of heterogeneous volumes, caused by certain issues such as sinusitis, perhaps halving a greater impact on small field sizes of the type commonly used in IMRT plans.

Gamma analysis and dose difference emphasised the role of EPID in detecting the inhomogeneity arising from sinusitis by comparing the energy deposited in the phosphor layer of the EPID, both with and without aeration changes. However, the EPID role was limited by anatomical superposition and the used gamma dimensional analysis since the effect of this change on tumour volume was not clear due to the overlapping. For the IMRT beam, the passing rates dramatically changed from 84% to 95% for 2D and 3D gamma analysis, respectively, in half fluid filled sinusitis, and from 82% to 94% in fully fluid filled sinusitis. To overcome this shortcoming, some recommendations were supplemented in order to maximise the benefits of EPID applications in radiotherapy. In brief, the recommendations urge the adaptation of two systems of dose verification and that the gamma criteria be set wisely with expert physicist supervision. Accordingly, the claim that the evaluation tool plays an important role in EPID application efficiency is supported.

In conclusion, the first part of the claim is supported. Namely, that EPID can report the dose discrepancy due to heterogeneous volumes caused by issues such as sinusitis. To that end, EPID, as deployed in my computational model, has shown

the potential to detect errors arising from such changes. Whereas the second part of the claim is rejected (namely, that EPID can report sinusitis effects on the dose distribution in tumour volumes) the EPID application was found to be limited by both anatomical overlapping and the range of available evaluation tools. Nevertheless, there are several recommendations for enhancing EPID's usefulness, for instance, record dose mapping for more than one beam.

This model can be beneficial and is promising in relation to tracking dose delivery for lung cases where inhomogeneity is a major issue. This is especially true in relation to the fact that EPID is easily accessible in many radiotherapy departments.

Chapter 6

Concluding remarks and recommendations for future work

Detectors are essential in both research and industrial facilities that use radiation beams for diagnostic or therapeutic purposes. The main objective of this work was to find the most optimal detector for a particular function, and to evaluate its suitability for the suggested function in radiology and radiotherapy departments.

6.1 Lassena (kV) and Lassena (MV) radiation detectors

In chapter 2, Lassena (kV) underwent a test according to IEC standards in order to evaluate its image resolution and noise level to obtain the DQE values. Based on the findings, the new radiation detector Lassena (kV) is suitable for general radiography as it has acceptable DQE values at three selected energies. These were 54 kV (RQA3), 74 kV (RQA5), and 92 kV (RQA7). However, this detector has a relatively high radiation susceptibility which limited its dynamic range by looking at the relationship between the mean pixel values and the K_a. DQE (0.5) values were 0.46 for RQA3, 0.52–0.56 for RQA5, and 0.55–0.59 for RQA7 with an integration time of 0.13s. The dynamic range can be increased by using a shorter integration

time or thinner scintillator. Moreover, the results of comparing the detector under investigation to other detectors presently on the market for CBCT usages demonstrated that Lassena (kV) has a promising potential for CBCT applications. This is especially true in that the contemporary market is seeking a detector suitable for CBCT usage, and which creates a good quality image with low radiation dose whilst also maintaining low image noise.

For Lassena (MV), the evaluation method was designed based on several studies [139–142]. The detector has been tested using MV source (Linac) with 6 MV in terms of the dosimetric properties (including linearity based on dose rate, reproducibility and uniformity) and image noise. the detector under investigation has a high degree of short-term reproducibility, with an STD of $\pm$ 0.25 and $\pm$ 0.02 for 51 and 105 MU/min. It also has an acceptable pixel uniformity-response at high dose rates with an STD of $\pm$ 0.012 and $\pm$ 0.004 for 51 and 105 MU/min, respectively. There is also decent linearity with a coefficient of determination (R^2) at 0.8624. Nevertheless, Lassena (MV) is not yet suitable as a clinical device since the detector becomes saturated after 105 MU/min, which in turn results in a limited dynamic range for the detector as the clinical dose rate is between 300 to 400 MU/min. These results might be due to the sensor (Lassena) or the scintillator thickness: more specifically, the thick scintillator will guarantee a large production of optical light. Therefore, it is highly recommended to use a thinner scintillator or thicker build up layer. Following this, the modified detector must go under new testing in order to verify whether or not acceptable results have been achieved within the necessary parameters. Moreover, it is recommended to determine the pMTF and DQE for Lassena (MV) in order to quantify its image quality because the detector can be used as an imager as well. The MTF can be simply measured using a thin tungsten edge phantom and accruing a high number of images to increase the photon flux as explained in detail by [255, 256].

6.2 MC system building, execution and calibration

A virtual linac was built and calibrated in chapter 3 in order to be used in chapters 4 and 5. The 6 MV and 10 MV beams were mimicked via BEAMnrc, using PSF_{IAEA} which is available online. Following this, DOSXYZnrc user code was utilised in order to calculate the dose in the water tank. For verification purposes, the PDDs and lateral profiles at different depths were extracted so as to be compared to the measured data provided by the Royal Free Hospital. Using a gamma criteria of 2%/ 2 mm, the PDD results demonstrated a high agreement for both energies, with a total of 100% of points having passed the gamma comparison for both 6 MV and 10 MV. It was observed that the inconsistency was pronounced at the build-up region due to head treatment scatter: however, in the equilibrium region, the differences were negligible. For the lateral profiles of both energies, more than 86% of the points passed the gamma comparison: however, the penumbra regions scored highest in terms of inconsistent results. This disagreement within the gradient region increased with the larger field size due to the high statistical fluctuations resulting from a limited number of particles. To conclude, the beam energy 6 MV is competent for use in MC simulations. For IMRT and VMAT applications, MLCs must be inserted to this system.

6.3 MC system implementation for parotid gland monitoring during radiotherapy

The EPID application for parotid gland shrinkage monitoring is highly recommended for radiotherapy of the head and neck given that it has been studied in silico in chapter 4. The MC system consists of a radiation source and three portal imaging devices (PIDs) which were: the water slab, and two Gadox-based detectors (5-slab and 17-slab). These were used in order to replicate the clinical EPID, and also to compare the response of the three models. This was performed by calculating the transmitted dose in the PIDs in order to evaluate their competence and to detect the

dose difference arising from anatomical changes between the planned and delivered doses. The anatomical changes were simulated computationally, and based on volume changes reported in the literature. Based on the computational experiment, the PIDs are able to monitor anatomical changes of the parotid gland during radiation treatment: this is achieved by applying tight gamma criteria (e.g., 1%/ 1 mm) with a mean difference around 0.2%. The simulated 17-slab PID began to register the dose deviation when the parotid gland shrunk by -26.3%, a change which is more likely to be seen during the third week of treatment. In a study by [108], and based on CBCT images, re-planning is found to be preferable when the volume reduced by 24– 30%, and occurring in the third week. Thus, the third week of treatment for nasopharyngeal sickness tends to be the most suitable time for re-planning and ART.

A comparison between three different detectors was made. According to gamma analysis, the passing rates of gamma evaluation for water and 5-slab models were lower than the suggested gamma level (95%) at -28.5%. However, the 17-slab model had a pass rate of less than 95% at -26.3% of the gland shrinkage, which is most likely to happen in the third week of treatment. This implies that the 5-slab does not exactly respond in the same manner as the 17-slab model: however, it can replace it since the mean difference between their responses is less than $\pm 5\%$.

In order to detect errors related to soft tissue with 2D gamma analysis, it is recommended to apply a strict criteria of 1%/ 1 mm, as discussed in chapter 4 and recommended by [85].

This computational study demonstrates the viable utility of EPID for monitoring anatomical changes of the parotid gland during radiation treatment.

6.4 EPID role to detect sinusitis impact on dose distribution and EPID limitations

In chapter 5, it was shown that the effect of aeration changes within the sinuses as per the dose distribution. This was investigated for the case of nasopharyngeal cancer. Two scenarios were involved in this study, scenario (b) and scenario (c). They were used in order to indicate half-filled maxillary sinuses with fluid, and fully-filled maxillary sinuses, respectively. The relationship between the effect of sinusitis and field size was established using PDD comparison: it was found that the effect faded by almost 50% for both scenarios at 5 cm $\times$ 5 cm and 10 cm $\times$ 10 cm, compared to 3 cm $\times$ 3 cm (where the PTV is overlapped with sinusitis). Hence, the dose discrepancy impact is found to be higher in small fields.

EPID has the capacity to find the dose discrepancy due to heterogeneity resulting from sinusitis since it has been emphasised via gamma analysis of a comparison between the energy deposited in the phosphor layer of the EPID, both with and without the aeration changes. The effect of this change on tumour volume itself was not clear: this was due to the anatomical overlapping. For gamma analysis, the passing rates dramatically changed from: 84% to 95% for 2D and 3D gamma analysis in half fluid-filled sinusitis, respectively; and, from 82% to 94% in fully fluid-filled sinusitis. Thus, the role of EPID in detecting such changes was restricted by anatomical superposition as well as the gamma criteria used.

6.5 Main recommendations for EPID applications

With a view to fully implementing EPID applications, several recommendations were stated in order to help users obtain the maximum benefits from dose verification using EPID. Gamma analysis is a standard tool for evaluation in many institutes. It must be used wisely and set according to the clinic's needs. The superposition of anatomy limits EPID performance in 2D dose verification: therefore, using two verification systems is strongly advised, or obtaining EPID from more

than one beam. An expert physicist will be able to comprehend and deal with these obstacles and overcome them.

To extend the investigation further, a powerful computer with a high CPU speed and sufficient memory is required in order to be able to readily use a voxel size as fine as that observed with the clinical EPID. Correspondingly, it is also recommended to avoid using PSF_{IAEA} since it contains a limited number of photons. When these considerations are taken into account, the model can be used to study other cases (e.g., like lung cases) where heterogeneity is a concern. The impact of anatomy overlapping may be tested by comparing the gamma map of the PTV slices in the patients to the gamma map at the EPID level, or by acquiring the EPID from all radiation beams.

Appendix A

Linac configuration

********** start of CM CHAMBER with identifier CHAMBER **********

10.0, RMAX

Monitor Chamber, 3 windows, 4 signal plates

14.835, ZMIN

0, 12, 0, N_TOP, N_CHM, N_BOT

9.9, 9.95, 10, RADII FOR CENTRAL PART

0.0127, 0, ZTHICK, FLAG FOR LAYER 1 IN CENTRAL PART

0.0, 0.0, 1, 6,

KAPTON700ICRU

0.238, 0, ZTHICK, FLAG FOR LAYER 2 IN CENTRAL PART

0.0, 0.0, 1, 6,

AIR700ICRU 0.00508, 0, ZTHICK, FLAG FOR LAYER 3 IN CENTRAL PART

0.0, 0.0, 1, 6,

KAPTON700ICRU

0.239, 0, ZTHICK, FLAG FOR LAYER 4 IN CENTRAL PART

0.0, 0.0, 1, 6,

AIR700ICRU

0.00508, 0, ZTHICK, FLAG FOR LAYER 5 IN CENTRAL PART

0.0, 0.0, 1, 6,

KAPTON700ICRU

0.238, 0, ZTHICK, FLAG FOR LAYER 6 IN CENTRAL PART

0.0, 0.0, 1, 6,

AIR700ICRU

0.0127, 0, ZTHICK, FLAG FOR LAYER 7 IN CENTRAL PART

0.0, 0.0, 1, 6,

KAPTON700ICRU

0.238, 0, ZTHICK, FLAG FOR LAYER 8 IN CENTRAL PART

0.0, 0.0, 1, 6,

AIR700ICRU

0.00508, 0, ZTHICK, FLAG FOR LAYER 9 IN CENTRAL PART

0.0, 0.0, 1, 6,

KAPTON700ICRU

0.477, 0, ZTHICK, FLAG FOR LAYER 10 IN CENTRAL PART

0.0, 0.0, 1, 6,

AIR700ICRU

0.0127, 0, ZTHICK, FLAG FOR LAYER 11 IN CENTRAL PART

0.0, 0.0, 1, 6,

KAPTON700ICRU

0.635, 0, ZTHICK, FLAG FOR LAYER 12 IN CENTRAL PART

0.0, 0.0, 1, 6,

AIR700ICRU

0.7, 0.01, 1, 6, chamber wall

AIR700ICRU

0.7, 0.01, 1, 6, gap

AIR700ICRU

0.7, 0.01, 1, 6, container

AIR700ICRU

1, MRNGE

********** start of CM MIRROR with identifier MIRROR **********

7, RMAX

Mylar mirror angle at 35 degree

17.985, 8.03, ZMIN, ZTHICK

5.729, -5.734, XFMIN, XBMIN

1, LAYERS

0.00508, thickness of layer 1

0.0, 0.0, 1, 7,

MYLAR700ICRU

0.0, 0.0, 1, 0,

AIR700ICRU

0.0, 0.0, 1, 0,

AIR700ICRU

********** start of CM MCTWIST with identifier mctwist **********

30, RMAX

MCTWIST MODULE

1, NMCTWIST

28.1, ZMIN

0.01, 0.7, 0.01, 0, 0, 0

AIR700ICRU

********** start of CM JAWS with identifier SECJAWS **********

20, RMAX Secondary collimators set to produce a 10x10 field at 100 cm SSD at dmax

2, PAIRED BARS OR JAWS

Y

28.2, 36, 1.41000, 1.80000, -1.41000, -1.80000,

X

36.9, 44.7, 1.84500, 2.23500, -1.84500, -2.23500,

0.7, 0.01, 1, 1,

0.7, 0.01, 1, 1,

W700ICRU

0.7, 0.01, 1, 1,

W700ICRU

********** start of CM DYNVMLC with identifier DYNVMLC **********

20.5, RMAX

dynamic VMLC

1, 3, 0, ORIENT, NGROUP, MODE

48.25, ZMIN

6.7, ZTHICK

0.5, 0.04, 0.04, 0.1354, 0.3252, 0.1227, 48.25, 48.533, 51.524, 51.732, 52.98, 53.28, 2, 54.5474, 54.812,

0.25, 0.04, 0.04, 0.0929, 0.1371, 0.1371, 48.345, 48.6096, 49.5277, 49.8277, 2, 51.625, 51.627, 54.7, 54.746,

0.25, 0.04, 0.04, 0.0354, 0.1285, 0.1235, 48.412, 48.531, 51.631, 51.732, 53.3293, 53.6293, 2, 54.5474, 54.812,

10, 1

40, 2

10, 1

-10.2, START

0.006, LEAFGAP

0, ENDTYPE

8, ZFOCUS or RADIUS of leaf ends

0, ZFOCUS of leaf sides

-10, 10, 40

-10, 10, 10

-10, 10, 10

0.7, 0.01, 1, 0,

AIR700ICRU

0.7, 0.01, 2, 0, 0,

W700ICRU

0.7, 0.01, 3, 0,

AIR700ICRU

**********end of all CMs**********

:Start MC Transport Parameter:

Global ECUT= 0.7

Global PCUT= 0.01

Global SMAX= 1e10

ESTEPE= 0.25

XIMAX= 0.5

Boundary crossing algorithm= Exact

Skin depth for BCA= 3

Electron-step algorithm= EGSnrc

Spin effects= On

Brems angular sampling= KM

Brems cross sections= NIST

Bound Compton scattering= On

Compton cross sections= default

Pair angular sampling= Simple

Pair cross sections= BH

Photoelectron angular sampling= On

Rayleigh scattering= Off

Atomic relaxations= On

Electron impact ionization= Off

Photon cross sections= xcom

Photon cross-sections output= Off

:Stop MC Transport Parameter:

Appendix B

Dose calculation

INPUT04

2

AIR700ICRU

H2O700ICRU

0.7, 0.01, 0, 0, 0

-1, -1, -1, 1

-15

0.4, 75

-15

0.4, 75

0

0.4, 75

1, 75, 1, 75, 1, 75, 2, 0

0, 0, 0, 0, 0, 0, 0, 0

0, 0, 0, 0, 0, 0, 0, 0

1, 108, 1, 108, 1, 120, 1, 1

1, 108, 1, 108, 1, 120, 0, 1

0, 0, 0, 0, 0, 0, 0, 1

2, 2, 0, 0, 0, 180, 0, 50.3, 0, 0, 20, 100, 0, 8

2, 2, 1, 100, 0, 0, 0, 0

/home/ucl/EGSnrc/egs_home/BEAM_TB_TWIST/6TWIST_10.egsphsp1 %file path

4000000000, 0, 50, 11, 50, 100, 0, 0, 1,

0, , 0, 0, 0, 80, 1, 0

:Start MC Transport Parameter:

Global ECUT= 0.7

Global PCUT= 0.01

Global SMAX= 5

ESTEPE= 0.25

XIMAX= 0.5

Boundary crossing algorithm= PRESTA-I

Skin depth for BCA= 0

Electron-step algorithm= PRESTA-II

Spin effects= On

Brems angular sampling= Simple

Brems cross sections= BH

Bound Compton scattering= Off

Compton cross sections= default

Pair angular sampling= Simple

Pair cross sections= BH

Photoelectron angular sampling= Off

Rayleigh scattering= Off

Atomic relaxations= Off

Electron impact ionization= Off

Photon cross sections= xcom

Photon cross-sections output= Off

:Stop MC Transport Parameter:

B.1 Phantom parameters for CTCREAT

DICOM

/home/hanan/EGSnrc/phant/mctlist

0, 0, 0, 0, 0, 0

0.25, 0.25, 0.25

5, -1024

AIR700ICRU

-500, 0.001, 0.044

fat700icru

-30, 0.9, 0.967

H2O700ICRU

0, 0.997, 1

ICRUTISSUE700ICRU

101, 0.302, 1.101

ICRPBONE700ICRU

1976, 1.101, 2.088

Appendix C

Extracting the MLCs positions from IMRT plan

function [beam$_data, beam_names, info$] $= readDicomMLC($filename$)$

$\%a function to extract MLCs poisitions saved in txt format.$

%INPUTS: filename - (optional) the name of the dicom file containing the RT % plan. if a file name is not provided a file selection

% dialog box will appear.

%OUTPUTS: MLCmovements for beamnrc - (title, nfields, index, MLC %poisitions in pairs)

if nargin <1

[f, p] = uigetfile('*.dcm');

filename = [p f];

info = dicominfo(filename);

fid= fopen('file.txt','w+t'); %put txt file path and name

= ('IMRT dynamic4'); %change the title for each beam

fprintf(fid,'%s',title); % title

fprintf(fid,'%.0f',227); %change the controlpoints for ecah beam

```
    nbeams = length(fieldnames(info.BeamSequence));

    for c = 1:nbeams

    beam = info.BeamSequence.(['Item_' num2str(4)]); %change the number of
beam
nfields = length(fieldnames(beam.ControlPointSequence));
for d = 1:nfields
beam2 = beam.ControlPointSequence.(['Item_' num2str(d)]);
index= beam2.CumulativeMetersetWeight;
if isfield(beam2, 'BeamLimitingDevicePositionSequence')==1
MLC1= beam2.BeamLimitingDevicePositionSequence;
nitem= length(fieldnames(MLC1));
for s = 1:nitem
MLC=MLC1.(['Item_' num2str(s)]);
ML=MLC.RTBeamLimitingDeviceType;
if strcmp(ML, 'MLCX')==1
MLC2= MLC.LeafJawPositions;
MLCcm=MLC2/10; %mm to cm
MLCnew=MLCcm/2.03; %1.944; %PLAN_SSD/My_SSD (100-lastCM_dist) is to
convert the distance
MLC1= MLCnew(1:60);
MLC11= MLCnew (61:120);
MMLLCC=[MLC1,MLC11];
A= flip (MMLLCC);

    end
end
end
fprintf(fid,'%.4f',index);
fprintf(fid,'%.2f,%.2f',A.');

    end
```

```
    end
fclose(fid);
```

C.1 Creating mask in MATLAB

```
dicomlist = dir(fullfile('FILEPATH','*.dcm'));
for cnt = 1 : numel(dicomlist)
I{cnt}= dicomread(fullfile('FILEPATH',dicomlist(cnt).name));
end
dmask=uint16(AA);
Rdmask=imrotate(dmask,270);
mask=flip(Rdmask,2);
se = offsetstrel('ball',3,3);
for x= 39:57
slice_image = I{1,(x)};
slice_mask = mask(:,:,(x));
combine = slice_mask.*slice_image;
masked_image = zeros(size(combine));

    masked_image((100<combine)  (combine<0)) = 1; % threshold
slice_image(masked_image<0) = 1000; % condition of if air -¿ water
I{1,(x)} = slice_image;

    end

    for cnt = 1 : numel(dicomlist)
metadata = dicominfo(fullfile('FILEPATH',dicomlist(cnt).name));
file_name = strcat('FILEEXIT', int2str(cnt),'.dcm');
dicomwrite(Icnt, file_name, metadata);
end
```

Bibliography

[1] Ehsan Samei and Douglas E Pfeiffer. *Clinical Medical Imaging Physics: Current and Emerging Practice*. John Wiley & Sons, 2020.

[2] Martin Spahn. X-ray detectors in medical imaging. *Nuclear Instruments and Methods in Physics Research Section A: Accelerators, Spectrometers, Detectors and Associated Equipment*, 731:57–63, 2013.

[3] International Electrotechnical Commission et al. Medical electrical equipment-characteristics of digital x-ray imaging devices-part 1: determination of detective quantum efficiency detectors used in mammography. *IEC 62220-1*, 2003.

[4] Anastasios C Konstantinidis, Magdalena B Szafraniec, Luigi Rigon, Giuliana Tromba, Diego Dreossi, Nicola Sodini, Panagiotis F Liaparinos, Steve Naday, Spencer Gunn, Alan McArthur, et al. X-ray performance evaluation of the dexela cmos aps x-ray detector using monochromatic synchrotron radiation in the mammographic energy range. *IEEE Transactions on Nuclear Science*, 60(5):3969–3980, 2013.

[5] C Michail, I Valais, I Seferis, N Kalyvas, G Fountos, and I Kandarakis. Experimental measurement of a high resolution cmos detector coupled to csi scintillators under x-ray radiation. *Radiation Measurements*, 74:39–46, 2015.

[6] C Michail, I Valais, N Martini, V Koukou, N Kalyvas, A Bakas, I Kandarakis, and G Fountos. Determination of the detective quantum efficiency

(dqe) of cmos/csi imaging detectors following the novel iec 62220-1-1: 2015 international standard. *Radiation Measurements*, 94:8–17, 2016.

[7] Lawrence Lechuga and Georg A Weidlich. Cone beam ct vs. fan beam ct: a comparison of image quality and dose delivered between two differing ct imaging modalities. *Cureus*, 8(9), 2016.

[8] Kavitha Srinivasan, Mohammad Mohammadi, and Justin Shepherd. Applications of linac-mounted kilovoltage cone-beam computed tomography in modern radiation therapy: A review. *Polish journal of radiology*, 79:181, 2014.

[9] Hassan S Abou-elenein, Ehab M Attalla, H Ammar, Ismail Eldesoky, Mohamed Farouk, and Mohamed S Zaghloul. Megavoltage cone beam computed tomography: Commissioning and evaluation of patient dose. *Journal of Medical Physics/Association of Medical Physicists of India*, 36(4):205, 2011.

[10] Ulrik V Elstrøm, Ludvig P Muren, Jørgen BB Petersen, and Cai Grau. Evaluation of image quality for different kv cone-beam ct acquisition and reconstruction methods in the head and neck region. *Acta Oncologica*, 50(6):908–917, 2011.

[11] MF Chan, J Yang, Y Song, C Burman, P Chan, and S Li. Evaluation of imaging performance of major image guidance systems. *Biomedical imaging and intervention journal*, 7(2), 2011.

[12] Samuel J Blake, Philip Vial, Lois Holloway, Peter B Greer, Aimee L McNamara, and Zdenka Kuncic. Characterization of optical transport effects on epid dosimetry using geant4. *Medical physics*, 40(4):041708, 2013.

[13] David S Chang, Foster D Lasley, Indra J Das, Marc S Mendonca, Joseph R Dynlacht, et al. *Basic radiotherapy physics and biology*. Springer, 2014.

[14] Indra J Das, Minsong Cao, Chee-Wai Cheng, Vladimir Misic, Klaus Scheuring, Edmund Schüle, and Peter AS Johnstone. A quality assurance phantom for electronic portal imaging devices. *Journal of applied clinical medical physics*, 12(2):391–403, 2011.

[15] Jerrold T Bushberg and John M Boone. *The essential physics of medical imaging*. Lippincott Williams & Wilkins, 2011.

[16] BMC McCurdy. Dosimetry in radiotherapy using a-si epids: Systems, methods, and applications focusing on 3d patient dose estimation. In *Journal of Physics: Conference Series*, volume 444, page 012002. IOP Publishing, 2013.

[17] Pejman Rowshanfarzad, Conor K McGarry, Michael P Barnes, Mahsheed Sabet, and Martin A Ebert. An epid-based method for comprehensive verification of gantry, epid and the mlc carriage positional accuracy in varian linacs during arc treatments. *Radiation Oncology*, 9(1):249, 2014.

[18] Jan-Jakob Sonke, Marianne Aznar, and Coen Rasch. Adaptive radiotherapy for anatomical changes. In *Seminars in radiation oncology*, volume 29, pages 245–257. Elsevier, 2019.

[19] Roel A Rozendaal, Ben J Mijnheer, Olga Hamming-Vrieze, Anton Mans, and Marcel Van Herk. Impact of daily anatomical changes on epid-based in vivo dosimetry of vmat treatments of head-and-neck cancer. *Radiotherapy and Oncology*, 116(1):70–74, 2015.

[20] Yinghui Li, Jinhan Zhu, Jinping Shi, Lixin Chen, and Xiaowei Liu. Investigating the effectiveness of monitoring relevant variations during imrt and vmat treatments by epid-based 3d in vivo verification performed using planning cts. *PloS one*, 14(6):e0218803, 2019.

[21] Michael G Herman, Jon J Kruse, and Christopher R Hagness. Guide to clinical use of electronic portal imaging. *Journal of Applied Clinical Medical Physics*, 1(2):38–57, 2000.

[22] Kathleen J Roxby and Jeffrey C Crosbie. Pre-treatment verification of intensity modulated radiation therapy plans using a commercial electronic portal dosimetry system. *Australasian physical & engineering sciences in medicine*, 33(1):51–57, 2010.

[23] Wouter Van Elmpt, Leah McDermott, Sebastiaan Nijsten, Markus Wendling, Philippe Lambin, and Ben Mijnheer. A literature review of electronic portal imaging for radiotherapy dosimetry. *Radiotherapy and oncology*, 88(3):289–309, 2008.

[24] Aleksandra Grzadziel, Barbara Smolińska, Roman Rutkowski, and Krzysztof Ślosarek. Epid dosimetry–configuration and pre-treatment imrt verification. *Reports of Practical Oncology & Radiotherapy*, 12(6):307–312, 2007.

[25] Hui Tian. Noise analysis in cmos image sensors. 2000.

[26] CD Arvanitis and SE Bohndiek. Active pixel cmos-based radiation detectors. 2014.

[27] Gerhard Lutz et al. *Semiconductor radiation detectors*. Springer, 2007.

[28] D Lazos, W Mourad, D Hauerstock, L Harrison, E Furhang, F Trichter, and RD Ennis. Comparison of fiducial-based 2d kv orthogonal imaging, fiducial-based cbct and soft tissue-based cbct registration for patient positioning correction in image guided radiation therapy for prostate cancer. *International Journal of Radiation Oncology• Biology• Physics*, 81(2):S763, 2011.

[29] Sarah E Bohndiek, Andrew Blue, Andy T Clark, Mark L Prydderch, Renato Turchetta, Gary J Royle, and Robert D Speller. Comparison of methods for estimating the conversion gain of cmos active pixel sensors. *IEEE Sensors Journal*, 8(10):1734–1744, 2008.

[30] J Cabello, A Bailey, I Kitchen, A Clark, J Crooks, R Halsall, M Key-Charriere, S Martin, M Prydderch, R Turchetta, et al. Digital autoradiogra-

phy using ccd and cmos imaging technology. In *2006 IEEE Nuclear Science Symposium Conference Record*, volume 4, pages 2607–2612. IEEE, 2006.

[31] Henok T Mebrahtu. Heavy ion radiation effects on cmos image sensors. 1993.

[32] M Bigas, Enric Cabruja, Josep Forest, and Joaquim Salvi. Review of cmos image sensors. *Microelectronics journal*, 37(5):433–451, 2006.

[33] M Tartagni, F Filomena, N Manaresi, R Canegallo, and R Guerrieri. A comparative analysis of active and passive pixel cmos image sensors.

[34] Anastasios Konstantinidis. *Evaluation of digital X-ray detectors for medical imaging applications*. PhD thesis, UCL (University College London), 2011.

[35] HK Kim. Practical expressions describing detective quantum efficiency in flat-panel detectors. *Journal of Instrumentation*, 6(11):C11020, 2011.

[36] Marco Bertolini, Andrea Nitrosi, Stefano Rivetti, Nico Lanconelli, Pierpaolo Pattacini, Vladimiro Ginocchi, and Mauro Iori. A comparison of digital radiography systems in terms of effective detective quantum efficiency. *Medical Physics*, 39(5):2617–2627, 2012.

[37] Nicole T Ranger, Ehsan Samei, James T Dobbins III, and Carl E Ravin. Assessment of detective quantum efficiency: intercomparison of a recently introduced international standard with prior methods. *Radiology*, 243(3):785–795, 2007.

[38] Hartmut Illers, Dirk Vandenbroucke, and Egbert Buhr. Measurement of correlated noise in images of computed radiography systems and its influence on the detective quantum efficiency. In *Medical Imaging 2004: Physics of Medical Imaging*, volume 5368, pages 639–647. International Society for Optics and Photonics, 2004.

[39] Ehsan Samei, Nicole T Ranger, James T Dobbins III, and Ying Chen. Intercomparison of methods for image quality characterization. i. modulation transfer function a. *Medical physics*, 33(5):1454–1465, 2006.

[40] Stefano Rivetti, Nico Lanconelli, Marco Bertolini, and Domenico Acchiappati. A new clinical unit for digital radiography based on a thick amorphous selenium plate: Physical and psychophysical characterization. *Medical physics*, 38(8):4480–4488, 2011.

[41] Stefano Rivetti, Nico Lanconelli, Marco Bertolini, Andrea Nitrosi, Aldo Burani, and Domenico Acchiappati. Comparison of different computed radiography systems: physical characterization and contrast detail analysis. *Medical physics*, 37(2):440–448, 2010.

[42] P Monnin, D Gutierrez, S Bulling, D Guntern, and FR Verdun. A comparison of the performance of digital mammography systems. *Medical physics*, 34(3):906–914, 2007.

[43] Giovanni Borasi, Ehsan Samei, Marco Bertolini, Andrea Nitrosi, and Davide Tassoni. Contrast-detail analysis of three flat panel detectors for digital radiography. *Medical physics*, 33(6Part1):1707–1719, 2006.

[44] Stefano Rivetti, Nico Lanconelli, Renato Campanini, Marco Bertolini, Gianni Borasi, Andrea Nitrosi, Claudio Danielli, Lidia Angelini, and Stefania Maggi. Comparison of different commercial ffdm units by means of physical characterization and contrast-detail analysis. *Medical physics*, 33(11):4198–4209, 2006.

[45] P Monnin, D Gutierrez, S Bulling, D Lepori, J-F Valley, and FR Verdun. Performance comparison of an active matrix flat panel imager, computed radiography system, and a screen-film system at four standard radiation qualities. *Medical physics*, 32(2):343–350, 2005.

[46] Giovanni Borasi, Andrea Nitrosi, Paolo Ferrari, and Davide Tassoni. On

site evaluation of three flat panel detectors for digital radiography. *Medical Physics*, 30(7):1719–1731, 2003.

[47] Andrew DA Maidment and Michael Albert. Conditioning data for calculation of the modulation transfer function. *Medical Physics*, 30(2):248–253, 2003.

[48] Ehsan Samei. Performance of digital radiographic detectors: quantification and assessment methods. *Advances in digital radiography: RSNA*, 27710:37–47, 2003.

[49] Alberto Del Guerra. *Ionizing radiation detectors for medical imaging*. World Scientific, 2004.

[50] Egbert Buhr, Susanne Günther-Kohfahl, and Ulrich Neitzel. Simple method for modulation transfer function determination of digital imaging detectors from edge images. In *Medical Imaging 2003: Physics of Medical Imaging*, volume 5030, pages 877–884. International Society for Optics and Photonics, 2003.

[51] James T Dobbins III, David L Ergun, Lois Rutz, Dean A Hinshaw, Hartwig Blume, and Dwayne C Clark. Dqe (f) of four generations of computed radiography acquisition devices. *Medical physics*, 22(10):1581–1593, 1995.

[52] Ehsan Samei, Michael J Flynn, and David A Reimann. A method for measuring the presampled mtf of digital radiographic systems using an edge test device. *Medical physics*, 25(1):102–113, 1998.

[53] Robert M Nishikawa. The fundamentals of mtf, wiener spectra, and dqe. *the University of Chicago, Depatment of Radiology, Chicago, USA, AAPM proceedings*, 1998.

[54] Mohd Awais Farooque and Jayant S Rohankar. Survey on various noises and techniques for denoising the color image. *International Journal of Application or Innovation in Engineering & Management (IJAIEM)*, 2(11):217–221, 2013.

[55] Pierre Gravel, Gilles Beaudoin, and Jacques A De Guise. A method for modeling noise in medical images. *IEEE Transactions on medical imaging*, 23(10):1221–1232, 2004.

[56] Kristin J McLoughlin, Philip J Bones, and Nico Karssemeijer. Noise equalization for detection of microcalcification clusters in direct digital mammogram images. *IEEE transactions on medical imaging*, 23(3):313–320, 2004.

[57] Jacob Beutel, Harold L Kundel, and Richard L Van Metter. *Handbook of medical imaging*, volume 1. Spie Press, 2000.

[58] Wei Zhao, Dylan C Hunt, Kenkichi Tanioka, and John A Rowlands. Indirect flat-panel detector with avalanche gain. In *Medical Imaging 2004: Physics of Medical Imaging*, volume 5368, pages 150–161. International Society for Optics and Photonics, 2004.

[59] John A Rowlands and John Yorkston. Flat panel detectors for digital radiography. *Handbook of medical imaging*, 1:223–328, 2000.

[60] Anders Brahme. *Comprehensive biomedical physics*. Newnes, 2014.

[61] LE Reinstein, HI Amols, PJ Biggs, AB Droege, AB Filimonov, W Lutz, and S Shalev. Radiotherapy portal imaging quality: Aapm report no. 24. *Report of AAPM Task Group*, 28, 1987.

[62] David I Thwaites and John B Tuohy. Back to the future: the history and development of the clinical linear accelerator. *Physics in Medicine & Biology*, 51(13):R343, 2006.

[63] Asghar Mesbahi, Michael Fix, Mahmoud Allahverdi, Ellen Grein, and Hossein Garaati. Monte carlo calculation of varian 2300c/d linac photon beam characteristics: a comparison between mcnp4c, geant3 and measurements. *Applied Radiation and Isotopes*, 62(3):469–477, 2005.

[64] Thuc M Pham. *Simulation of the transmitted dose in an EPID using a Monte Carlo method.* PhD thesis, 2009.

[65] David Greene and Peter C Williams. *Linear accelerators for radiation therapy*. CRC Press, 1997.

[66] ERVIN B Podgorsak. External photon beams: Physical aspects. *Radiation Oncology Physics: A handbook for teachers and students'. Vienna: IAEA*, page 169, 2005.

[67] Ervin B Podgorsak et al. Radiation oncology physics. *Vienna: International Atomic Energy Agency*, pages 123–271, 2005.

[68] Guillaume Lamé and Mary Dixon-Woods. Using clinical simulation to study how to improve quality and safety in healthcare. *BMJ Simulation and Technology Enhanced Learning*, 6(2), 2020.

[69] Robert L Harrison. Introduction to monte carlo simulation. In *AIP conference proceedings*, volume 1204, pages 17–21. American Institute of Physics, 2010.

[70] Donald C Craig. *Extensible hierarchical object-oriented logic simulation with an adaptable graphical user interface*. PhD thesis, Memorial University of Newfoundland, 1996.

[71] Peter L Bonate. A brief introduction to monte carlo simulation. *Clinical pharmacokinetics*, 40(1):15–22, 2001.

[72] I Kawrakow, E Mainegra-Hing, DWO Rogers, et al. Egsnrcmp: the multiplatform environment for egsnrc. *National Research Council of Canada, Ottawa*, 2006.

[73] DWO Rogers, B Walters, Iwan Kawrakow, et al. Beamnrc users manual. *Nrc Report Pirs*, 509:12, 2009.

[74] BRBI Walters, Iwan Kawrakow, DWO Rogers, et al. Dosxyznrc users manual. *Nrc Report Pirs*, 794:1–125, 2005.

[75] I Kawrakow and DWO Rogers. The egsnrc code system. *NRC Report PIRS-701, NRC, Ottawa*, 2000.

[76] N Reynaert, S Van der Marck, D Schaart, W Van der Zee, M Tomsej, C van Vliet-Vroegindeweij, J Jansen, M Coghe, C De Wagter, and B Heijmen. Monte carlo treatment planning: an introduction. *Report NCS-16 (Netherlands Commission on Radiation Dosimetry, Delft)*, 2006.

[77] Sangeetha Shanmugasundaram and Sureka Chandrasekaran. Optimization of variance reduction techniques used in egsnrc monte carlo codes. *Journal of Medical Physics*, 43(3):185, 2018.

[78] Maged Mohammed, E Chakir, H Boukhal, Mroan Saeed, and T El Bardouni. Evaluation of variance reduction techniques in beamnrc monte carlo simulation to improve the computing efficiency. *Journal of Radiation Research and Applied Sciences*, 9(4):424–430, 2016.

[79] Frank Verhaegen and Jan Seuntjens. Monte carlo modelling of external radiotherapy photon beams. *Physics in medicine & biology*, 48(21):R107, 2003.

[80] Turki Almatani. Optimisation of variance reduction techniques in egsnrc monte carlo for a 6 mv photon beam of an elekta synergy linear accelerator. *Journal of King Saud University-Science*, 33(4):101421, 2021.

[81] Joao Seco and Frank Verhaegen. *Monte Carlo techniques in radiation therapy*. CRC press, 2013.

[82] Pedro Andreo. Monte carlo simulations in radiotherapy dosimetry. *Radiation Oncology*, 13(1):121, 2018.

[83] Daniel A Low, William B Harms, Sasa Mutic, and James A Purdy. A technique for the quantitative evaluation of dose distributions. *Medical physics*, 25(5):656–661, 1998.

[84] Xuejun Gu, Xun Jia, and Steve B Jiang. Gpu-based fast gamma index calculation. *Physics in Medicine & Biology*, 56(5):1431, 2011.

[85] Moyed Miften, Arthur Olch, Dimitris Mihailidis, Jean Moran, Todd Pawlicki, Andrea Molineu, Harold Li, Krishni Wijesooriya, Jie Shi, Ping Xia, et al. Tolerance limits and methodologies for imrt measurement-based verification qa: recommendations of aapm task group no. 218. *Medical physics*, 45(4):e53–e83, 2018.

[86] Jonas Bengtsson Scherman. Developement and evaluation of methods for comparison of dose distributions in radiotherapy using calculated, synthetic and simulated measured dose distributions. 2009.

[87] B Catlin, J Lyons, Muller O'Rahilly, and Swenson Carpenter. Basic human anatomy. *The pharynx and larynx. Dartmouth Medical School*, 2008.

[88] NHS. *Nasopharyngeal cancer*, 2018 (accessed November 20, 2020).

[89] American Cancer Society. *Treatment Options by Stage of Nasopharyngeal Cancer*, 2019 (accessed November 20, 2020).

[90] Nicholas L Mankowski and Bruno Bordoni. Anatomy, head and neck, nasopharynx. In *StatPearls [Internet]*. StatPearls Publishing, 2020.

[91] Gang Ren, Shou-Ping Xu, Lei Du, Lin-Chun Feng, Bao-Lin Qu, Hai-Xia Liu, Chuan-Bin Xie, and Lin Ma. Actual anatomical and dosimetric changes of parotid glands in nasopharyngeal carcinoma patients during intensity modulated radiation therapy. *BioMed research international*, 2015, 2015.

[92] Hannah M Chason and Brian W Downs. Anatomy, head and neck, parotid gland. In *StatPearls [Internet]*. StatPearls Publishing, 2018.

[93] Joseph O Deasy, Vitali Moiseenko, Lawrence Marks, KS Clifford Chao, Jiho Nam, and Avraham Eisbruch. Radiotherapy dose–volume effects on salivary gland function. *International Journal of Radiation Oncology* Biology* Physics*, 76(3):S58–S63, 2010.

[94] Giuseppe Sanguineti, Francesco Ricchetti, Binbin Wu, Todd McNutt, and Claudio Fiorino. Parotid gland shrinkage during imrt predicts the time to xerostomia resolution. *Radiation Oncology*, 10(1):19, 2015.

[95] G Sanguineti, F Ricchetti, O Thomas, B Wu, and T McNutt. Pattern and predictors of volumetric change of parotid glands during intensity modulated radiotherapy. *The British journal of radiology*, 86(1031):20130363, 2013.

[96] Simona Marzi, Alessia Farneti, Antonello Vidiri, Francesca Di Giuliano, Laura Marucci, Filomena Spasiano, Irene Terrenato, and Giuseppe Sanguineti. Radiation-induced parotid changes in oropharyngeal cancer patients: the role of early functional imaging and patient-/treatment-related factors. *Radiation Oncology*, 13(1):189, 2018.

[97] Wei Li, ZP Sun, XJ Liu, and GY Yu. Volume measurements of human parotid and submandibular glands. *Beijing da xue xue bao. Yi xue ban= Journal of Peking University. Health sciences*, 46(2):288, 2014.

[98] PDQ Adult Treatment Editorial Board. Paranasal sinus and nasal cavity cancer treatment (adult)(pdq®): Health professional version. *PDQ Cancer Information Summaries [Internet]*, 2002.

[99] Nick Jones. The nose and paranasal sinuses physiology and anatomy. *Advanced drug delivery reviews*, 51(1-3):5–19, 2001.

[100] Chih-Jen Huang, Ming-Yii Huang, Ming-Chen Paul Shih, Kai-yuan Cheng, Ka-Wo Lee, Tzu-Ying Lu, Shyng-Shiou Yuan, and Pen-Tzu Fang. Post-radiation sinusitis is associated with recurrence in nasopharyngeal carcinoma patients treated with intensity-modulated radiation therapy. *Radiation Oncology*, 14(1):1–8, 2019.

[101] SM Morrill, ML Langer, RG Lane, and II Rosen. Tissue heterogeneity effects in treatment plan optimization. *International Journal of Radiation Oncology* Biology* Physics*, 30(3):699–706, 1994.

[102] David J Noble, Ping-Lin Yeap, Shannon YK Seah, Karl Harrison, Leila EA Shelley, Marina Romanchikova, Amy M Bates, Yaolin Zheng, Gillian C Barnett, Richard J Benson, et al. Anatomical change during radiotherapy for head and neck cancer, and its effect on delivered dose to the spinal cord. *Radiotherapy and Oncology*, 130:32–38, 2019.

[103] Trinanjan Basu and Nithin Bhaskar. Overview of important "organs at risk"(oar) in modern radiotherapy for head and neck cancer (hnc). In *Cancer Survivorship*. IntechOpen, 2018.

[104] 6. Organs at Risk and Morbidity-Related Concepts and Volumes. *Journal of the International Commission on Radiation Units and Measurements*, 13(1-2):79–88, 06 2016.

[105] Søren M Bentzen, Louis S Constine, Joseph O Deasy, Avi Eisbruch, Andrew Jackson, Lawrence B Marks, Randall K Ten Haken, and Ellen D Yorke. Quantitative analyses of normal tissue effects in the clinic (quantec): an introduction to the scientific issues. *International Journal of Radiation Oncology* Biology* Physics*, 76(3):S3–S9, 2010.

[106] Ivo Beetz, Roel JHM Steenbakkers, Olga Chouvalova, Charles R Leemans, Patricia Doornaert, Bernard FAM van der Laan, Miranda EMC Christianen, Arjan Vissink, Henk P Bijl, Peter van Luijk, et al. The quantec criteria for parotid gland dose and their efficacy to prevent moderate to severe patient-rated xerostomia. *Acta Oncologica*, 53(5):597–604, 2014.

[107] Govind Raghavan, Amar U Kishan, Minsong Cao, and Allen M Chen. Anatomic and dosimetric changes in patients with head and neck cancer treated with an integrated mri-tri-60co teletherapy device. *The British journal of radiology*, 89(1067):20160624, 2016.

[108] Alba Fiorentino, R Caivano, V Metallo, C Chiumento, M Cozzolino, G Califano, S Clemente, P Pedicini, and V Fusco. Parotid gland volumetric changes

during intensity-modulated radiotherapy in head and neck cancer. *The British journal of radiology*, 85(1018):1415–1419, 2012.

[109] Eric K Hansen, M Kara Bucci, Jeanne M Quivey, Vivian Weinberg, and Ping Xia. Repeat ct imaging and replanning during the course of imrt for head-and-neck cancer. *International Journal of Radiation Oncology* Biology* Physics*, 64(2):355–362, 2006.

[110] Victor Gabriel Leandro Alves, Mahmoud Ahmed, Eric Aliotta, Wookjin Choi, and Jeffrey Vincent Siebers. An error detection method for real-time epid-based treatment delivery quality assurance. *Medical Physics*, 48(2):569–578, 2021.

[111] B Mijnheer, A Jomehzadeh, P González, I Olaciregui-Ruiz, R Rozendaal, P Shokrani, H Spreeuw, R Tielenburg, and A Mans. Error detection during vmat delivery using epid-based 3d transit dosimetry. *Physica Medica*, 54:137–145, 2018.

[112] Todsaporn Fuangrod, Peter B Greer, Henry C Woodruff, John Simpson, Shashank Bhatia, Benjamin Zwan, A Timothy, Boyd MC McCurdy, and Richard H Middleton. Investigation of a real-time epid-based patient dose monitoring safety system using site-specific control limits. *Radiation Oncology*, 11(1):1–10, 2016.

[113] Leah N McDermott, Markus Wendling, Jan-Jakob Sonke, Marcel van Herk, and Ben J Mijnheer. Anatomy changes in radiotherapy detected using portal imaging. *Radiotherapy and oncology*, 79(2):211–217, 2006.

[114] Nicholas J Lowther, David A Hamilton, Han Kim, Jamie M Evans, Steven H Marsh, and Robert JW Louwe. Monitoring anatomical changes of individual patients using statistical process control during head-and-neck radiotherapy. *Physics and Imaging in Radiation Oncology*, 9:21–27, 2019.

[115] Pascal Francois, Philippe Boissard, Lucie Berger, and Alejandro Mazal. In

vivo dose verification from back projection of a transit dose measurement on the central axis of photon beams. *Physica Medica*, 27(1):1–10, 2011.

[116] Manikandan Arjunan, Sureka Chandra Sekaran, Biplab Sarkar, and Saran Kumar Manavalan. Electronic portal imaging device-based three-dimensional volumetric dosimetry for intensity-modulated radiotherapy pre-treatment quality assurance. *Journal of medical physics*, 44(3):176, 2019.

[117] Markus Wendling, Leah N. McDermott, Anton Mans, Ígor Olaciregui-Ruiz, Raul Pecharromán-Gallego, Jan-Jakob Sonke, Joep Stroom, Marcel van Herk, and Ben J. Mijnheer. In aqua vivo epid dosimetry. *Medical physics*, 39(1):367–377, 2012.

[118] Ophélie Piron, Nicolas Varfalvy, and Louis Archambault. Establishing action threshold for change in patient anatomy using epid gamma analysis and ptv coverage for head and neck radiotherapy treatment. *Medical physics*, 45(8):3534–3545, 2018.

[119] Irina Malajovich, Boon-Keng Kevin Teo, Heather Petroccia, James M Metz, Lei Dong, and Taoran Li. Characterization of the megavoltage cone-beam computed tomography (mv-cbct) system on halcyontm for igrt: Image quality benchmark, clinical performance, and organ doses. *Frontiers in oncology*, 9:496, 2019.

[120] Hooshang Nikjoo, Shuzo Uehara, and Dimitris Emfietzoglou. *Interaction of radiation with matter*. CRC press, 2012.

[121] Jared R. Robbins. Advances in image-guided radiation oncology: Changing the way we treat cancer. AAMD 43rd Annual Meeting, 2018.

[122] Larry E Antonuk. Electronic portal imaging devices: a review and historical perspective of contemporary technologies and research. *Physics in Medicine & Biology*, 47(6):R31, 2002.

[123] Yun Inn Tan. *2D transit dosimetry using electronic portal imaging device*. PhD thesis, University of Glasgow, 2016.

[124] Sofia Celi, Emilie Costa, Claas Wessels, Alejandro Mazal, Alain Fourquet, and Pascal Francois. Epid based in vivo dosimetry system: clinical experience and results. *Journal of applied clinical medical physics*, 17(3):262–276, 2016.

[125] Hideharu Miura, Shuichi Ozawa, Masahiro Hayata, Shintarou Tsuda, Tsubasa Enosaki, Kiyoshi Yamada, and Yasushi Nagata. Evaluation of cone-beam computed tomography image quality assurance for vero4drt system. *Reports of Practical Oncology & Radiotherapy*, 22(3):258–263, 2017.

[126] Jolien Heukelom and Clifton David Fuller. Head and neck cancer adaptive radiation therapy (art): conceptual considerations for the informed clinician. In *Seminars in radiation oncology*, volume 29, pages 258–273. Elsevier, 2019.

[127] Wei Wang, Haihua Yang, Wei Hu, Guoping Shan, Weijun Ding, Changhui Yu, Biyun Wang, Xufeng Wang, and Qianyi Xu. Clinical study of the necessity of replanning before the 25th fraction during the course of intensity-modulated radiotherapy for patients with nasopharyngeal carcinoma. *International Journal of Radiation Oncology* Biology* Physics*, 77(2):617–621, 2010.

[128] Peter H Ahn, Chin-Cheng Chen, Andrew I Ahn, Linda Hong, Paola G Scripes, Jin Shen, Chen-Chiao Lee, Ekeni Miller, Shalom Kalnicki, and Madhur K Garg. Adaptive planning in intensity-modulated radiation therapy for head and neck cancers: single-institution experience and clinical implications. *International Journal of Radiation Oncology* Biology* Physics*, 80(3):677–685, 2011.

[129] H Zhong and JY Jin. Recent advances and challenges in adaptive radiotherapy for patients with locally advanced nsclc. *Ann Radiat Ther Oncol*, 1, 2017.

[130] Eelco Lens et al. *Respiratory motion management for radiotherapy of pancreatic cancer patients*. 2017.

[131] B Mijnheer. Epid-based dosimetry and its relation to other 2d and 3d dose measurement techniques in radiation therapy. In *Journal of Physics: Conference Series*, volume 847, page 012024. IOP Publishing, 2017.

[132] James L Bedford, Ian M Hanson, and Vibeke N Hansen. Comparison of forward-and back-projection in vivo epid dosimetry for vmat treatment of the prostate. *Physics in Medicine & Biology*, 63(2):025008, 2018.

[133] SS Korreman. Semi-and virtual 3d dosimetry in clinical practice. In *Journal of Physics: Conference Series*, volume 444, page 012007. IOP Publishing, 2013.

[134] Sean L Berry, Cynthia Polvorosa, Simon Cheng, Israel Deutsch, KS Clifford Chao, and Cheng-Shie Wuu. Initial clinical experience performing patient treatment verification with an electronic portal imaging device transit dosimeter. *International Journal of Radiation Oncology* Biology* Physics*, 88(1):204–209, 2014.

[135] VN Hansen, PM Evans, and W Swindell. The application of transit dosimetry to precision radiotherapy. *Medical physics*, 23(5):713–721, 1996.

[136] Shouliang Ding, Yongbao Li, Hongdong Liu, Rui Li, Bin Wang, Jun Zhang, Yan Chen, and Xiaoyan Huang. Comparison of intensity modulated radiotherapy treatment plans between 1.5 t mr-linac and conventional linac. *Technology in Cancer Research & Treatment*, 20:1533033820985871, 2021.

[137] I Sedgwick, D Das, N Guerrini, B Marsh, and R Turchetta. Lassena: a 6.7 megapixel, 3-sides buttable wafer-scale cmos sensor using a novel grid-addressing architecture. *Proc Int Image Sens Work*, pages 3–6, 2013.

[138] Thilo Michel, Gisela Anton, M Böhnel, J Durst, M Firsching, A Korn, B Kreisler, A Loehr, F Nachtrab, D Niederlöhner, et al. A fundamental

method to determine the signal-to-noise ratio (snr) and detective quantum efficiency (dqe) for a photon counting pixel detector. *Nuclear Instruments and Methods in Physics Research Section A: Accelerators, Spectrometers, Detectors and Associated Equipment*, 568(2):799–802, 2006.

[139] YAM Yousif, AJ Van Rensburg, et al. Performance evaluation of the siemens electronic portal imaging device for imrt plan verification. *International Journal of Medical Physics, Clinical Engineering and Radiation Oncology*, 4(03):215, 2015.

[140] Aiping Ding, Lei Xing, and Bin Han. Development of an accurate epid-based output measurement and dosimetric verification tool for electron beam therapy. *Medical Physics*, 42(7):4190–4198, 2015.

[141] Shrikant Deshpande, Aitang Xing, Lois Holloway, Peter Metcalfe, and Philip Vial. Dose calibration of epids for segmented imrt dosimetry. *Journal of applied clinical medical physics*, 15(6):103–118, 2014.

[142] Peter B Greer and Carmen C Popescu. Dosimetric properties of an amorphous silicon electronic portal imaging device for verification of dynamic intensity modulated radiation therapy. *Medical physics*, 30(7):1618–1627, 2003.

[143] Rita Reymen Dominique Huyskens Xiaodong Xiaodong He, Ann Van Esch. Evaluation of an electronic portal imaging device for transit dosimetry. *Acta Oncologica*, 38(5):591–596, 1999.

[144] Awusi Kavuma. *Transit dosimetry based on water equivalent path length measured with an amorphous silicon electronic portal imaging device*. PhD thesis, University of Glasgow, 2011.

[145] Eurostat. Handbook on precision requirements and variance estimation for ess households surveys, 2013.

[146] CE Dick and JW Motz. Image information transfer properties of x-ray fluorescent screens. *Medical physics*, 8(3):337–346, 1981.

[147] Marco Endrizzi, Piernicola Oliva, Bruno Golosio, and Pasquale Delogu. Cmos aps detector characterization for quantitative x-ray imaging. *Nuclear Instruments and Methods in Physics Research Section A: Accelerators, Spectrometers, Detectors and Associated Equipment*, 703:26–32, 2013.

[148] NW Marshall. Detective quantum efficiency measured as a function of energy for two full-field digital mammography systems. *Physics in Medicine & Biology*, 54(9):2845, 2009.

[149] Matteo Salomoni, Rosalinde Pots, Etiennette Auffray, and Paul Lecoq. Enhancing light extraction of inorganic scintillators using photonic crystals. *Crystals*, 8(2):78, 2018.

[150] Anastasios C Konstantinidis, Magdalena B Szafraniec, Robert D Speller, and Alessandro Olivo. The dexela 2923 cmos x-ray detector: A flat panel detector based on cmos active pixel sensors for medical imaging applications. *Nuclear Instruments and Methods in Physics Research Section A: Accelerators, Spectrometers, Detectors and Associated Equipment*, 689:12–21, 2012.

[151] Kenneth A Fetterly and Nicholas J Hangiandreou. Effects of x-ray spectra on the dqe of a computed radiography system. *Medical physics*, 28(2):241–249, 2001.

[152] Youcef El-Mohri, Kyung-Wook Jee, Larry E Antonuk, Manat Maolinbay, and Qihua Zhao. Determination of the detective quantum efficiency of a prototype, megavoltage indirect detection, active matrix flat-panel imager. *Medical physics*, 28(12):2538–2550, 2001.

[153] Rongqing Hui and Maurice O'Sullivan. *Fiber optic measurement techniques*. Academic Press, 2009.

[154] Xinghui Liu, Hai Ou, Jun Chen, Shaozhi Deng, Ningsheng Xu, and Kai Wang. Highly photosensitive dual-gate a-si: H tft and array for low-dose flat-panel x-ray imaging. *IEEE Photonics Technology Letters*, 28(18):1952–1955, 2016.

[155] Qinan Bao and Arion F Chatziioannou. Estimation of the minimum detectable activity of preclinical pet imaging systems with an analytical method. *Medical physics*, 37(11):6070–6083, 2010.

[156] IA Cunningham. Applied linear-systems theory in handbook of medical imaging. *Physics and psychophysics*, pages 82–157, 2000.

[157] Hanan Alzahrani, Sion Richards, Iain Sedgwick, Paul Seller, Anastasios Konstantinidis, Gary Royle, and Kate Ricketts. Image quality determination of a novel digital detector for x-ray imaging and cone-beam computed tomography applications. *Nuclear Instruments and Methods in Physics Research Section A: Accelerators, Spectrometers, Detectors and Associated Equipment*, page 163914, 2020.

[158] RV Sousa. Dose rate influence on deep dose deposition using a 6 mv x-ray beam from a linear accelerator. *Brazilian Journal of Physics*, 39(2):292–296, 2009.

[159] Janhavi R Bhangle, VK Sathiya Narayanan, and Shrikant A Deshpande. Dose linearity and uniformity of siemens oncor impression plus linear accelerator designed for step-and-shoot intensity-modulated radiation therapy. *Journal of Medical Physics/Association of Medical Physicists of India*, 32(3):103, 2007.

[160] Wavelength company. Photodiode basics: Selection operation. `https://www.teamwavelength.com/photodiode-basics/`, 2020.

[161] Karim Zarei Zefreh, Jan De Beenhouwer, Federica Marone Welford, and Jan Sijbers. Investigation on effect of scintillator thickness on afterglow in

indirect-flat panel detectors. In *Online e-journal of nondestructive testing.–*. 2016.

[162] Monte Carlo Support. `https://myvarian.com`. Accessed: 2019-02-10.

[163] Simon K Goodall and Martin A Ebert. Recommended dose voxel size and statistical uncertainty parameters for precision of monte carlo dose calculation in stereotactic radiotherapy. *Journal of Applied Clinical Medical Physics*, 21(12):120–130, 2020.

[164] BRB Walters and I Kawrakow. A "howfarless" option to increase efficiency of homogeneous phantom calculations with dosxyznrc. *Medical physics*, 34(10):3794–3807, 2007.

[165] I Kawrakow and BRB Walters. Efficient photon beam dose calculations using dosxyznrc with beamnrc. *Medical physics*, 33(8):3046–3056, 2006.

[166] Jung-in Kim, So-Yeon Park, Hak Jae Kim, Jin Ho Kim, Sung-Joon Ye, and Jong Min Park. The sensitivity of gamma-index method to the positioning errors of high-definition mlc in patient-specific vmat qa for sbrt. *Radiation oncology*, 9(1):1–12, 2014.

[167] Valerie J Easton and John H McColl. Statistics glossary v1. 1. 1997.

[168] Jatinder R Palta. Tolerance limits and action levels for planning and delivery of imrt. *Intensity-Modulated Radiation Therapy. The State Of The Art*, pages 593–612, 2003.

[169] Margarida Fragoso, Iwan Kawrakow, Bruce A Faddegon, Timothy D Solberg, and Indrin J Chetty. Fast, accurate photon beam accelerator modeling using beamnrc: A systematic investigation of efficiency enhancing methods and cross-section data. *Medical physics*, 36(12):5451–5466, 2009.

[170] Jason Y Cheng, Holly Ning, Barbara C Arora, Ying Zhuge, and Robert W Miller. Output factor comparison of monte carlo and measurement for varian truebeam 6 mv and 10 mv flattening filter-free stereotactic radiosurgery system. *Journal of applied clinical medical physics*, 17(3):100–110, 2016.

[171] Bibekananda Mishra, Subhalaxmi Mishra, T Palani Selvam, ST Chavan, and SN Pethe. Comparison of measured and monte carlo calculated dose distributions from indigenously developed 6 mv flattening filter free medical linear accelerator. *Journal of Medical Physics*, 43(3):162, 2018.

[172] J Sempau, A Sánchez-Reyes, F Salvat, H Oulad ben Tahar, SB Jiang, and JM Fernández-Varea. Monte carlo simulation of electron beams from an accelerator head using penelope. *Physics in Medicine & Biology*, 46(4):1163, 2001.

[173] Eyad Alhakeem and Sergei Zavgorodni. Evaluation of latent variances in monte carlo dose calculations with varian truebeam photon phase-spaces used as a particle source. *Physics in Medicine & Biology*, 63(1):01NT03, 2017.

[174] Kwo-Ping Chang, Zhi-Wei Wang, and An-Cheng Shiau. Determining optimization of the initial parameters in monte carlo simulation for linear accelerator radiotherapy. *Radiation Physics and Chemistry*, 95:161–165, 2014.

[175] F Renner, J Wulff, RP Kapsch, and Klemens Zink. Uncertainties in monte carlo-based absorbed dose calculations for an experimental benchmark. *Physics in Medicine & Biology*, 60(19):7637, 2015.

[176] Mohandass Palanisamy, Khanna David, Manigandan Durai, Narendra Bhalla, and Abhishek Puri. Dosimetric impact of statistical uncertainty on monte carlo dose calculation algorithm in volumetric modulated arc therapy using monaco tps for three different clinical cases. *Reports of Practical Oncology and Radiotherapy*, 24(2):188–199, 2019.

[177] Nirmal Sakthi, Paul Keall, Ivaylo Mihaylov, Qiuwen Wu, Yan Wu, Jeffrey F Williamson, Rupert Schmidt-Ullrich, and Jeffrey V Siebers. Monte carlo–based dosimetry of head-and-neck patients treated with sib-imrt. *International Journal of Radiation Oncology* Biology* Physics*, 64(3):968–977, 2006.

[178] Ji-Hye Song, Min-Joo Kim, So-Hyun Park, Seu-Ran Lee, Min-Young Lee, Dong Soo Lee, and Tae Suk Suh. Gamma analysis dependence on specified low-dose thresholds for vmat qa. *Journal of applied clinical medical physics*, 16(6):263–272, 2015.

[179] Peter C Austin. Using the standardized difference to compare the prevalence of a binary variable between two groups in observational research. *Communications in statistics-simulation and computation*, 38(6):1228–1234, 2009.

[180] Shrikant Deshpande, Samuel J Blake, Aitang Xing, Peter E Metcalfe, Lois C Holloway, and P Vial. A simple model for transit dosimetry based on a water equivalent epid. *Medical physics*, 45(3):1266–1275, 2018.

[181] A Teymurazyan and G Pang. Monte carlo simulation of a novel water-equivalent electronic portal imaging device using plastic scintillating fibers. *Medical physics*, 39(3):1518–1529, 2012.

[182] B Warkentin, S Steciw, S Rathee, and BG Fallone. Dosimetric imrt verification with a flat-panel epid. *Medical physics*, 30(12):3143–3155, 2003.

[183] JO Kim, JV Siebers, PJ Keall, and R Mohan. A monte carlo model of an amorphous silicon flat panel imager for portal dose prediction. In *EPI2K2 Program & Abstract Book (7th International Workshop on Electronic Portal Imaging, Vancouver BC, 2002)*, pages 118–119, 2002.

[184] PJ Keall, JV Siebers, R Jeraj, and R Mohan. The effect of dose calculation uncertainty on the evaluation of radiotherapy plans. *Medical physics*, 27(3):478–484, 2000.

[185] Jean-Noël Badel. Contrôle dosimétrique des traitements de radiothérapie par simulation monte carlo de l'image de dose portale transmise. *Institut National des Sciences Appliquées de Lyon., Algerie*, 2009.

[186] Martin J Berger, J S Coursey, and M A Zucker. Estar, pstar, and astar: computer programs for calculating stopping-power and range tables for electrons, protons, and helium ions (version 1.21). 1999.

[187] O Grundmann, GC Mitchell, and KH Limesand. Sensitivity of salivary glands to radiation: from animal models to therapies. *Journal of dental research*, 88(10):894–903, 2009.

[188] Jeremias Hey, Juergen Setz, Reinhard Gerlach, Martin Janich, Guido Hildebrandt, Dirk Vordermark, Christian R Gernhardt, and Thomas Kuhnt. Parotid gland-recovery after radiotherapy in the head and neck region-36 months follow-up of a prospective clinical study. *Radiation oncology*, 6(1):1–8, 2011.

[189] J Gildersleve, DP Dearnaley, PM Evans, and W Swindell. Reproducibility of patient positioning during routine radiotherapy, as assessed by an integrated megavoltage imaging system. *Radiotherapy and Oncology*, 35(2):151–160, 1995.

[190] Laurent Gilbeau, Michelle Octave-Prignot, Thiery Loncol, Laurette Renard, Pierre Scalliet, and Vincent Grégoire. Comparison of setup accuracy of three different thermoplastic masks for the treatment of brain and head and neck tumors. *Radiotherapy and Oncology*, 58(2):155–162, 2001.

[191] Hui Wu, Xiaojian Chen, Xin Yang, Yalan Tao, Yunfei Xia, Xiaowu Deng, Cheng Zheng, Jared Robbins, Christopher Schultz, and X Allen Li. Early prediction of acute xerostomia during radiation therapy for head and neck cancer based on texture analysis of daily ct. *International Journal of Radiation Oncology* Biology* Physics*, 102(4):1308–1318, 2018.

[192] Ceri Powell, Maria Schmidt, Marco Borri, Dow-Mu Koh, Mike Partridge, Angela Riddell, Gary Cook, Shreerang A Bhide, Christopher M Nutting, Kevin J Harrington, et al. Changes in functional imaging parameters following induction chemotherapy have important implications for individualised patient-based treatment regimens for advanced head and neck cancer. *Radiotherapy and Oncology*, 106(1):112–117, 2013.

[193] Chunhui Han, Yi-Jen Chen, An Liu, Timothy E Schultheiss, and Jeffrey YC Wong. Actual dose variation of parotid glands and spinal cord for nasopharyngeal cancer patients during radiotherapy. *International Journal of Radiation Oncology* Biology* Physics*, 70(4):1256–1262, 2008.

[194] Choonik Lee, Katja M Langen, Weiguo Lu, Jason Haimerl, Eric Schnarr, Kenneth J Ruchala, Gustavo H Olivera, Sanford L Meeks, Patrick A Kupelian, Thomas D Shellenberger, et al. Assessment of parotid gland dose changes during head and neck cancer radiotherapy using daily megavoltage computed tomography and deformable image registration. *International Journal of Radiation Oncology* Biology* Physics*, 71(5):1563–1571, 2008.

[195] Choonik Lee, Katja M Langen, Weiguo Lu, Jason Haimerl, Eric Schnarr, Kenneth J Ruchala, Gustavo H Olivera, Sanford L Meeks, Patrick A Kupelian, Thomas D Shellenberger, et al. Evaluation of geometric changes of parotid glands during head and neck cancer radiotherapy using daily mvct and automatic deformable registration. *Radiotherapy and Oncology*, 89(1):81–88, 2008.

[196] Sitti Yani, Ilmi Rizkia, Mohamad Fahdillah Rhani, Mohammad Haekal, Freddy Haryanto, et al. Egsnrc application for imrt planning. *Reports of Practical Oncology & Radiotherapy*, 25(2):217–226, 2020.

[197] Simona Horová and K Badraoui Cuprova. Linear accelerator and mlc monte carlo model in egsnrc/beamnrc system. 2014.

[198] Roberto Capote, Francisco Sánchez-Doblado, Antonio Leal, Juan Ignacio

Lagares, Rafael Arráns, and Günther H Hartmann. An egsnrc monte carlo study of the microionization chamber for reference dosimetry of narrow irregular imrt beamlets. *Medical physics*, 31(9):2416–2422, 2004.

[199] Emily Heath, Jan Seuntjens, and Daryoush Sheikh-Bagheri. Dosimetric evaluation of the clinical implementation of the first commercial imrt monte carlo treatment planning system at 6 mv. *Medical physics*, 31(10):2771–2779, 2004.

[200] Lixin Zhan, Runqing Jiang, and Ernest K Osei. Beam coordinate transformations from dicom to dosxyznrc. *Physics in Medicine & Biology*, 57(24):N513, 2012.

[201] Chiara Arilli, Yannik Wandael, Chiara Galeotti, Livia Marrazzo, Silvia Calusi, Mattia Grusio, Isacco Desideri, Franco Fusi, Angelo Piermattei, Stefania Pallotta, et al. Combined use of a transmission detector and an epid-based in vivo dose monitoring system in external beam whole breast irradiation: A study with an anthropomorphic female phantom. *Applied Sciences*, 10(21):7611, 2020.

[202] Thao Vu, Eli Riekeberg, Yumou Qiu, and Robert Powers. Comparing normalization methods and the impact of noise. *Metabolomics*, 14(8):1–10, 2018.

[203] Jung-Ha Kim, Robin Hill, and Zdenka Kuncic. An evaluation of calculation parameters in the egsnrc/beamnrc monte carlo codes and their effect on surface dose calculation. *Physics in Medicine & Biology*, 57(14):N267, 2012.

[204] IA Popescu, P Atwal, J Lobo, J Lucido, and BMC McCurdy. Patient-specific qa using 4d monte carlo phase space predictions and epid dosimetry. In *Journal of Physics: Conference Series*, volume 573, page 012004, 2015.

[205] Jennifer M Steers and Benedick A Fraass. Imrt qa: Selecting gamma criteria based on error detection sensitivity. *Medical physics*, 43(4):1982–1994, 2016.

[206] Min Yao, Michael M Graham, Henry T Hoffman, Russell B Smith, Gerry F Funk, Scott M Graham, Kenneth J Dornfeld, Mark Skwarchuk, Yusuf Menda, and John M Buatti. The role of post–radiation therapy fdg pet in prediction of necessity for post–radiation therapy neck dissection in locally advanced head-and-neck squamous cell carcinoma. *International Journal of Radiation Oncology* Biology* Physics*, 59(4):1001–1010, 2004.

[207] Boyd MC McCurdy, Kurt Luchka, and Stephen Pistorius. Dosimetric investigation and portal dose image prediction using an amorphous silicon electronic portal imaging device. *Medical physics*, 28(6):911–924, 2001.

[208] F Cremers, Th Frenzel, C Kausch, D Albers, T Schönborn, and R Schmidt. Performance of electronic portal imaging devices (epids) used in radiotherapy: image quality and dose measurements. *Medical physics*, 31(5):985–996, 2004.

[209] C Kirkby and R Sloboda. Comprehensive monte carlo calculation of the point spread function for a commercial-si epid. *Medical physics*, 32(4):1115–1127, 2005.

[210] M Partridge, B-M Hesse, and L Müller. A performance comparison of direct- and indirect-detection flat-panel imagers. *Nuclear Instruments and Methods in Physics Research Section A: Accelerators, Spectrometers, Detectors and Associated Equipment*, 484(1-3):351–363, 2002.

[211] AE Schach von Wittenau, CM Logan, MB Aufderheide Iii, and DM Slone. Blurring artifacts in megavoltage radiography with a flat-panel imaging system: Comparison of monte carlo simulations with measurements. *Medical physics*, 29(11):2559–2570, 2002.

[212] Shouping Xu, Zhaoxia Wu, Cungeng Yang, Lin Ma, Baolin Qu, Guangpei Chen, Weirong Yao, Shi Wang, Yaqiang Liu, and X Allen Li. Radiation-induced ct number changes in gtv and parotid glands during the course of

radiation therapy for nasopharyngeal cancer. *The British journal of radiology*, 89(1062):20140819, 2016.

[213] Howard E Morgan and David J Sher. Adaptive radiotherapy for head and neck cancer. *Cancers of the head & neck*, 5(1):1–16, 2020.

[214] Murat Surucu, Karan K Shah, Ibrahim Mescioglu, John C Roeske, William Small Jr, Mehee Choi, and Bahman Emami. Decision trees predicting tumor shrinkage for head and neck cancer: Implications for adaptive radiotherapy. *Technology in cancer research & treatment*, 15(1):139–145, 2016.

[215] Jong Min Park, So-Yeon Park, and Hyoungnyoun Kim. Modulation index for vmat considering both mechanical and dose calculation uncertainties. *Physics in Medicine & Biology*, 60(18):7101, 2015.

[216] Jong Min Park, So-Yeon Park, Hyoungnyoun Kim, Jin Ho Kim, Joel Carlson, and Sung-Joon Ye. Modulation indices for volumetric modulated arc therapy. *Physics in Medicine & Biology*, 59(23):7315, 2014.

[217] So-Yeon Park, Jong Min Park, Wonmo Sung, Il Han Kim, and Sung-Joon Ye. Texture analysis on the edge-enhanced fluence of vmat. *Radiation Oncology*, 10(1):1–11, 2015.

[218] Gary A Ezzell, Jay W Burmeister, Nesrin Dogan, Thomas J LoSasso, James G Mechalakos, Dimitris Mihailidis, Andrea Molineu, Jatinder R Palta, Chester R Ramsey, Bill J Salter, et al. Imrt commissioning: multiple institution planning and dosimetry comparisons, a report from aapm task group 119. *Medical physics*, 36(11):5359–5373, 2009.

[219] James Pawley. *Handbook of biological confocal microscopy*, volume 236. Springer Science & Business Media, 2006.

[220] Jennifer C O'Daniel, Adam S Garden, David L Schwartz, He Wang, Kian K Ang, Anesa Ahamad, David I Rosenthal, William H Morrison, Joshua A Asper, Lifei Zhang, et al. Parotid gland dose in intensity-modulated radiother-

apy for head and neck cancer: is what you plan what you get? *International Journal of Radiation Oncology* Biology* Physics*, 69(4):1290–1296, 2007.

[221] Helen Gustafsson, Philip Vial, Zdenka Kuncic, Clive Baldock, and Peter B Greer. Epid dosimetry: Effect of different layers of materials on absorbed dose response. *Medical physics*, 36(12):5665–5674, 2009.

[222] Ross I Berbeco. *Beam's Eye View Imaging in Radiation Oncology*. CRC Press, 2017.

[223] Loredana Marcu, Eva Bezak, and Barry Allen. *Biomedical physics in radiotherapy for cancer*. Csiro publishing, 2012.

[224] Hanan Alzahrani, Sion Richards, Iain Sedgwick, Paul Seller, Anastasios Konstantinidis, Gary Royle, and Kate Ricketts. Image quality determination of a novel low energy x-ray detector. In *2018 IEEE Nuclear Science Symposium and Medical Imaging Conference Proceedings (NSS/MIC)*, pages 1–2. IEEE, 2018.

[225] Stefano Peca and Derek Brown. Sensitivity to inhomogeneities for an in-vivo epid dosimetry method: Poster-thur eve-25. *Medical Physics*, 41, 2014.

[226] H Arimura, Y Egashira, Y Shioyama, K Nakamura, S Yoshidome, S Anai, S Nomoto, H Honda, F Toyofuku, Y Higashida, et al. Computerized method for estimation of the location of a lung tumor on epid cine images without implanted markers in stereotactic body radiotherapy. *Physics in Medicine & Biology*, 54(3):665, 2009.

[227] Yuki Narita, Takahiro Kato, Takashi Ono, Sho Oyama, Shinya Komori, Kazuhiro Arai, Yoshitomo Abe, Takaomi Harada, Tatsuya Nakamura, Hitoshi Wada, et al. Effect of anatomical change on dose distribution during radiotherapy for maxillary sinus carcinoma: passive scattering proton therapy versus volumetric-modulated arc therapy. *The British journal of radiology*, 92(1093):20180273, 2019.

[228] Dongho Shin, Myonggeun Yoon, Sung-Yong Park, Suk Lee, Sang Hoon Lee, Hyun Do Huh, Dae Yong Kim, Kwan Ho Cho, and Dong Oh Shin. Quality assurance of inhomogeneity correction algorithm in the intensity modulated radiotherapy and dynamic conformal arc radiotherapy using multiple heterogeneous head and neck phantoms. In *World Congress on Medical Physics and Biomedical Engineering 2006*, pages 1867–1870. Springer, 2007.

[229] American Association of Physicists in Medicine (AAPM) et al. Tissue inhomogeneity corrections for megavoltage photon beams, 2004.

[230] Reda Kamel, Samy Al-Badawy, Akram Khairy, Tarek Kandil, and Aly Sabry. Nasal and paranasal sinus changes after radiotherapy for nasopharyngeal carcinoma. *Acta oto-laryngologica*, 124(4):532–535, 2004.

[231] Simone C Cardoso, Victor Gabriel L Alves, Luiz Antonio R da Rosa, Luciana T Campos, Delano VS Batista, and Alessandro Facure. Monte carlo simulation of bony heterogeneity effects on dose profile for small irradiation field in radiotherapy. *Plos one*, 5(5):e10466, 2010.

[232] Jeffrey O Bennett, William L Briggs, and Anthony Badalamenti. *Using and understanding mathematics: A quantitative reasoning approach*. Pearson Addison Wesley Reading, 2008.

[233] Joseph O Deasy, Angel I Blanco, and Vanessa H Clark. Cerr: a computational environment for radiotherapy research. *Medical physics*, 30(5):979–985, 2003.

[234] F Seif, MR Bayatiani, S Hamidi, and M Kargaran. Investigating the effect of air cavities of sinuses on the radiotherapy dose distribution using monte carlo method. *Journal of biomedical physics & engineering*, 9(1):121, 2019.

[235] Hiroto Yoshikawa and Michael W Nolan. Changes in target volume during irradiation of canine intranasal tumors can significantly impact radiation dosimetry. *Veterinary Radiology & Ultrasound*, 60(5):594–604, 2019.

[236] Navin Singh, Sunil Dutt Sharma, Nirmal Kumar Painuly, Abhijit Mandal, Lalit Mohan Agarwal, Ashutosh Sinha, et al. Underdosing of the maxillary sinus for small fields used in newer radiotherapy techniques: Comparison of thermoluminescent dosimeter and monte carlo data. *Journal of cancer research and therapeutics*, 14(2):351, 2018.

[237] Sara Bresciani, Amalia Di Dia, Angelo Maggio, Claudia Cutaia, Anna Miranti, Erminia Infusino, and Michele Stasi. Tomotherapy treatment plan quality assurance: the impact of applied criteria on passing rate in gamma index method. *Medical physics*, 40(12):121711, 2013.

[238] Indra J Das, Chee-Wai Cheng, Kashmiri L Chopra, Raj K Mitra, Shiv P Srivastava, and Eli Glatstein. Intensity-modulated radiation therapy dose prescription, recording, and delivery: patterns of variability among institutions and treatment planning systems. *Journal of the National Cancer Institute*, 100(5):300–307, 2008.

[239] Debbie van der Merwe, Jacob Van Dyk, Brendan Healy, Eduardo Zubizarreta, Joanna Izewska, Ben Mijnheer, and Ahmed Meghzifene. Accuracy requirements and uncertainties in radiotherapy: a report of the international atomic energy agency. *Acta oncologica*, 56(1):1–6, 2017.

[240] Michael L Taylor and Tomas Kron. Consideration of the radiation dose delivered away from the treatment field to patients in radiotherapy. *Journal of medical physics/Association of Medical Physicists of India*, 36(2):59, 2011.

[241] Megan E Daly, Allen M Chen, M Kara Bucci, Ivan El-Sayed, Ping Xia, Michael J Kaplan, and David W Eisele. Intensity-modulated radiation therapy for malignancies of the nasal cavity and paranasal sinuses. *International Journal of Radiation Oncology* Biology* Physics*, 67(1):151–157, 2007.

[242] Rezvan Azimi, Parham Alaei, and Patrick Higgins. The effect of small field output factor measurements on imrt dosimetry. *Medical Physics*, 39(8):4691–4694, 2012.

[243] Dandan Zhang, Bin Wang, Guangshun Zhang, Charlie Ma, and Xiaowu Deng. Comparison of 3d and 2d gamma passing rate criteria for detection sensitivity to imrt delivery errors. *Journal of applied clinical medical physics*, 19(4):230–238, 2018.

[244] Theodore S Hong, Wolfgang A Tomé, and Paul M Harari. Heterogeneity in head and neck imrt target design and clinical practice. *Radiotherapy and Oncology*, 103(1):92–98, 2012.

[245] Lloyd Asp, Morris Bank, Theodore Fields, William Hendee, Douglas Jones, Cohn Orton, Vincent Sampiere, George Starkschall, K. David Steidley, and Bruce Thomadsen. Statement on the role of a physicist in radiation oncology, 1985.

[246] Khaldoon M Radaideh. Dosimetric impact of weight loss and anatomical changes at organs at risk during intensity-modulated radiotherapy for head-and-neck cancer. *Journal of Radiation Research and Applied Sciences*, 13(1):301–308, 2020.

[247] Motoharu Sasaki, Hitoshi Ikushima, Masahide Tominaga, Takeshi Kamomae, Taro Kishi, Masataka Oita, and Masafumi Harada. Dose impact of rectal gas on prostatic imrt and vmat. *Japanese journal of radiology*, 33(12):723–733, 2015.

[248] Vitali Moiseenko, Mitchell Liu, Sarah Kristensen, Gerald Gelowitz, and Eric Berthelet. Effect of bladder filling on doses to prostate and organs at risk: a treatment planning study. *Journal of Applied Clinical Medical Physics*, 8(1):55–68, 2007.

[249] Hailei Lin, Shaomin Huang, Xiaowu Deng, Jinhan Zhu, and Lixin Chen. Comparison of 3d anatomical dose verification and 2d phantom dose verification of imrt/vmat treatments for nasopharyngeal carcinoma. *Radiation Oncology*, 9(1):1–7, 2014.

[250] YAC Fiagan, F Simonato, A Roggio, MA Rossato, A Scaggion, R Zandonà, and M Paiusco. Comparison between 2d and 3d imrt pre-treatment verification. *Physica Medica: European Journal of Medical Physics*, 32:22, 2016.

[251] Kiley B Pulliam, Jessie Y Huang, Rebecca M Howell, David Followill, Ryan Bosca, Jennifer O'Daniel, and Stephen F Kry. Comparison of 2d and 3d gamma analyses. *Medical physics*, 41(2):021710, 2014.

[252] Audrey H Zhuang and Arthur J Olch. Sensitivity study of an automated system for daily patient qa using epid exit dose images. *Journal of applied clinical medical physics*, 19(3):114–124, 2018.

[253] Bin Han, Aiping Ding, Minghui Lu, and Lei Xing. Pixel response-based epid dosimetry for patient specific qa. *Journal of applied clinical medical physics*, 18(1):9–17, 2017.

[254] Masayuki Nishiki, Kunio Shiraishi, Takuya Sakaguchi, and Kyojiro Nambu. Method for reducing noise in x-ray images by averaging pixels based on the normalized difference with the relevant pixel. *Radiological physics and technology*, 1(2):188–195, 2008.

[255] Josh Star-Lack, Daniel Shedlock, Dennis Swahn, Dave Humber, Adam Wang, Hayley Hirsh, George Zentai, Daren Sawkey, Isaac Kruger, Mingshan Sun, et al. A piecewise-focused high dqe detector for mv imaging. *Medical physics*, 42(9):5084–5099, 2015.

[256] Yi Wang, Larry E Antonuk, Qihua Zhao, Youcef El-Mohri, and Louis Perna. High-dqe epids based on thick, segmented bgo and csi: Tl scintillators: Performance evaluation at extremely low dose. *Medical physics*, 36(12):5707–5718, 2009.